

**INTERSTITIAL FLOWS MODULATE BREAST TUMOR CELL
INVASION USING A 3D MICROFLUIDIC MODEL**

A Dissertation

Presented to the Faculty of the Graduate School
of Cornell University

in Partial Fulfillment of the Requirements for the Degree of
Doctor of Philosophy

by

Yu Ling Huang

May 2019

© 2019 Yu Ling Huang

Interstitial flows modulate breast tumor cell invasion using a 3D microfluidic model

By

Yu Ling Huang, Ph.D

Cornell University 2019

Abstract

Tumor cell invasion through the extracellular matrix (ECM) is a critical step in the cancer metastatic cascade. Along the way from primary tumor to a distant metastatic site, tumor cells interact actively with the microenvironment either via biophysical or biochemical signals. It is now indisputable that the tumor microenvironment (TME) is as important as the genetic makeup of the tumor in regulating tumor invasion. To date, roles of biophysical cues within the TME, apart from matrix stiffness and architecture, in tumor invasion are poorly understood. Interstitial flows (IFs) are ubiquitous in maintaining tissue homeostasis in living systems, and are known to be elevated in malignant tumors due to the abnormal vasculature developed within the tumor. My dissertation focuses on revealing roles of IFs in breast tumor cell invasion using a newly developed 3D microfluidic platform and optical imaging.

This dissertation contains four main parts. First, I reviewed current understanding on the subject of TME in tumor invasion. Second, I presented work on the development of a microfluidic platform that provided well defined IFs to cells or spheroids embedded within a type I collagen matrix. Third, I studied roles of IFs in modulating invasion characteristics of single breast tumor cells (MDA-MB-231 cell line). I found that IFs carried away the cell-secreted adhesion molecules, fibronectin, and subsequently promoted amoeboid over mesenchymal cell morphology and motility. Most importantly, IFs inhibited tumor cells' ability to spread. Fourth, I studied roles of IFs in tumor spheroid invasion. For mono-culture spheroid (MDA-MB-231 cells supplemented

with Matrigel), IFs inhibited tumor cell invasion. For co-culture tumor spheroids made of 1:1 mixture of malignant and non-tumorigenic epithelial cells, IFs promoted tumor cell invasion via downregulating cell-cell adhesion E-cadherin of non-tumorigenic cells.

In summary, my work revealed that IFs inhibited tumor cell invasion in both single cell and mono-culture spheroid models via modulating cell-ECM adhesion. In contrast, IFs promoted tumor cell invasion in the co-culture spheroid model via downregulating cell-cell adhesion of the non-tumorigenic cells. My work highlighted the importance of biophysical parameter, IF, in regulating cell-ECM and cell-cell adhesion, and consequently modulating tumor invasion.

BIOGRAPHICAL SKETCH

The author Yu Ling Huang is a Ph.D candidate at Cornell University with a major in Biological Engineering. Yu Ling joined the Biofluidics Lab since May 2012 under the supervision of Professor Mingming Wu. During her Ph.D program, Yu Ling also worked as a teaching assistant for Principles of Biological Engineering (BEE 2600), an introductory level undergraduate course for Biological Engineering students, for five semesters. Prior to her Ph.D program, Yu Ling worked in Dr. Michael Shuler's lab on organ-on-a-chip research project as a Master of Engineering student, and received her Master of Engineering degree in Biomedical Engineering from Cornell University in May 2012. Yu Ling received her Bachelor of Science degree in Chemical Engineering with a concentration on molecular Engineering from Clarkson University in May 2011. Prior to her college, Yu Ling attended Lower East Side Prep High School in Manhattan, New York, after she immigrated to the U.S. with her family in 2004. Prior to that, Yu Ling was born and lived in Guang Dong, China.

After successful completion of the Doctor of Philosophy degree, Yu Ling will continue her academic career at Professor Mingming Wu's lab at Cornell as a postdoctoral research fellow for one year, and then she will move on to her next position.

LET PATIENCE HAVE ITS PERFECT WORK, THAT YOU MAYBE PERFECT AND
COMPLETE, LACKING NOTHING.

- James 1:4

ACKNOWLEDGMENTS

I owe my gratitude to a team of veritable supporters who have helped me in every way in culminating this Ph.D. and made my graduate school experience fruitful and memorable.

First, I would like to deeply express my sincere gratitude to my advisor, Professor Mingming Wu, for her guidance, encouragement, and patience in both research and teaching over the last seven years. She has been constantly inspiring and often post thought-provoking questions to me. She has been an extremely supporter for me to outreach to the STEM field as well as to equip myself academically. Inside the lab, she has taught me to be a hands-on engineer; while outside the lab, she taught me how to balance work and life, and being super understanding. I cannot imagine a better advisor and mentor in this chapter of my life.

I would like to extend my gratitude to my research project collaborator also my AD Hoc committee member Professor Jeffrey Segall, for his insights and expertise in guiding my experiments and research. I would also like to thank my dissertation committee members: Professor Mike Shuler and Professor Jan Lammerding for taking their time and providing insightful discussions and comments to further refine this work.

I would like to thank many of the current and former Wu Lab members: Dr. Beum Jun Kim, who has trained me most of the lab techniques and cell culturing; Dr. Chih-kuan Tung, who designed the microfluidic device and has trained me in microfabrication and microfluidic experiments; Dr. Matthew Hall, for training me in preparing 3D collagen matrix and characterizing the collagen gel; Dr. Xinzeng Feng and his advisor Professor Chung-Yuen Hui, for their help in understanding the theory in characterizing the mechanical properties of collagen gel; Young Joon Suh, for helping me to troubleshoot many pieces of the lab equipment; Brian Cheung and Dr. Sumit Dey, for insightful discussion on molecular biology. In addition, special thanks to all of my wonderful undergraduate students: Anqi (Angela) Zheng, Yujie Ma, Carina Shiau, Cindy Wu, and Min Seo Kang, and a high school student Audrey Chang, who have been dedicated to the hard work on the cell analysis for me, and without whom this work would not be able to be completed.

I am fortunate to have such great professors at Cornell University. Thanks to all the professors who taught me about biological and biomedical engineering, biofluidics, and nanobiotechnology classes that I have taken. I would like to thank Dr. Mandy Esch who sparked my interest in nanobiotechnology and Paula Miller for initial cell culture training. I would like to thank Dr. Wei Song and Dr. Jason Lu from Professor Mingling Ma's lab for sharing their tumor

spheroid formation platforms and offering reagents in my urgent situations. Thanks to all the supportive staff at BEE, Deb Higgins and Mary Cornell, and approximately 50 wonderful undergraduate TAs in my teaching class.

I would like to acknowledge the funding sources for my work from the National Center for Research Resources (5R21RR025801-03) and the NIH (8R21 GM103388-03, R21CA138366, U54CA143876), the Cornell Center on the Microenvironment & Metastasis (Award No U54CA143876 from the National Cancer Institute), the Cornell NanoScale Science and Technology Facility (CNF), Cornell University Biotechnology Resource Center and the Cornell Nanobiotechnology Center (NBTC), and the Imaging facility.

I would like to thank my wonderful friends throughout these years. Thanks to Yih-Lin Goh who has helped me to settle down in Ithaca when I arrived. Special thanks to my previous housemates Jing Jiang and Fei Wu for the laugh time. Particularly thanks to all the members of the Hong Kong Christian Fellowship, College Town Bible Fellowship, and First Ithaca Chinese Christian Church. Deeply thanks to Professor David Ng and Dr. Mavis Ng for their wise guidance in many aspects in our life.

Finally, I would like to thank my family for supporting my odyssey PhD journey. My deepest gratitude to my parents, my sister and brother, my parents in law, my grandparents, and my relatives, without whom I could not have accomplished anything. Above all, thanks to my amazing husband Fan Yang for his sacrificial love and care that made it possible for me to complete this work. Last but not least, thanks to my two lovely children, Lydia and Luca for being so sweet and adorable. Most importantly, I would like to thank God for He is faithful and enable me to complete this dissertation in every single aspect. Thank you!

TABLE OF CONTENTS

Preliminary Sections

Abstract	iii
Biographical Sketch	v
Acknowledgements	vii
Table of Contents	ix
List of Figures	xi
List of Tables	xii
List of Abbreviations	xii

Chapter 1: Introduction 1

1.1 The tumor microenvironment (TME) in cancer metastasis	1
1.2 Biophysical drivers in tumor cell invasion	2
1.2.1 Intramural flow in tumor cell invasion	2
1.2.2 Interstitial flow (IF) in tumor cell invasion	4
1.2.3 Extracellular matrix (ECM) in tumor cell invasion	9
1.3 Current state of art on microfluidic modeling of biophysical microenvironment in tumor cell invasion	10
1.3.1 Microfluidic models for intramural flows in tumor cell invasion	10
1.3.2 Microfluidic models for interstitial flows in tumor cell invasion	13
1.3.3 Microfluidic models for coupling intramural and IF in tumor cell invasion	19
1.3.4 Microfluidics for modeling ECM architecture in tumor cell invasion	19
1.4 Overview and aims	22

Chapter 2: Development of a contact line pinning microfluidic for modeling IF ... 23

2.1 A need for developing microfluidics that generate well-defined IFs	23
2.2 Design principles for a contact line pinning microfluidic device	23
2.3 Fabrication of the microfluidic device	25
2.4 Microfluidic device preparation	26
2.5 IF measurement and validation within the 3D microfluidic device	27

Chapter 3: Interstitial flows promote amoeboid over mesenchymal cell motility of breast tumor cell invasion in single cell assays 30

3.1 Introduction	30
3.2 Materials and method	32
3.2.1 3D cell culture preparation	32
3.2.2 Experimental procedures	33
3.2.3 Microfluidic device experimental setup	34
3.2.4 Staining for actin filaments	34
3.2.5 Imaging and data analysis	35
3.3 Results and discussion	36

3.3.1	IFs promote an amoeboid cell morphology and motility	36
3.3.2	Exogenous fibronectin promotes a mesenchymal cell phenotype	41
3.3.3	IFs mildly enhanced cell speed but not directional migration	42
3.3.4	The fastest migrating cells are within the amoeboid cells	44
3.3.5	IFs impaired the mean square displacements and persistence	45
3.4	Conclusion and future perspectives	48
3.5	Supplementary information	49
 Chapter 4: Interstitial flows modulate breast tumor spheroid invasion		51
4.1	Introduction	51
4.2	Materials and methods	53
4.2.1	Fabrication of microwells for spheroid formation	53
4.2.2	Cells, spheroids, and 3D spheroid culture preparation	53
4.2.3	Immunostaining of E-cadherin	56
4.2.4	Microfluidic setup and experimental procedure	57
4.2.5	Imaging and data analysis	60
4.3	Results and discussion	62
4.4	Interstitial flows promoted co-culture tumor spheroid invasion	62
4.4.1	IFs enable co-cultured tumor spheroid dissociation	62
4.4.2	IFs down regulated E-cadherin of the non-tumorigenic cells	65
4.4.3	IFs promoted amoeboid cell morphology of the tumor cells	68
4.4.4	IFs promoted a single over collective cell motility of non-tumorigenic cells	68
4.4.5	IFs enhanced the motility of both the metastatic and non- tumorigenic cells	70
4.5	Interstitial flows is not sufficient to promote the non-tumorigenic spheroid invasion	73
4.6	Interstitial flows inhibit malignant tumor spheroid invasion	75
4.6.1	IF reduced tumor cell motility	75
4.6.2	IF diminished the tumor cell ability to spread	76
4.6.3	IF promoted amoeboid cell morphology	78
4.7	Conclusion & future perspectives	78
 Chapter 5: Summary, conclusion and future perspectives		80
5.1	Summery on the roles of IF on tumor cell invasion	80
5.2	Conclusion	82
5.3	Implications	85
5.4	Future project: IFs on tumor spheroid intravasation in a 3D microfluidic model	85
5.5	Opportunities, challenges and perspectives	87
 Appendix: Other research projects		
Appendix A: Cooperative roles of interstitial flows and topography on tumor cell invasion ...		92
Appendix B: Characterize the mechanical properties of Collagen gels.....		96
 References.....		102

LIST OF FIGURES

Figure 1.1: Important biophysical parameters in the tumor microenvironment (TME).	2
Figure 1.2: High interstitial fluid pressure and elevated interstitial flows in the tumor..	6
Figure 1.3: Modeling interstitial flows in tumor cell invasion studies.	18
Figure 2.1: Illustration of contact line pinning idea.....	24
Figure 2.2: Design principle of a contact line pinning based microfluidic device.....	25
Figure 2.3: IF measurement using FRAP method.....	27
Figure 2.4: IF measurement and validation.....	28
Figure 3.1. Microfluidic device setup for single cell experiment.....	34
Figure 3.2: IFs promote an amoeboid cell morphology and motility.....	38
Figure 3.3. Amoeboid versus mesenchymal motility.....	39
Figure 3.4: Exogenous FN promote a mesenchymal cell phenotype.....	41
Figure 3.5: IFs slightly enhance cell speed but no significant directional migration.....	43
Figure 3.6: Maximum cell speed is inversely correlated to the aspect ratio of cells.....	45
Figure 3.7: IFs impair MDA-MB-231 mean square displacements and persistence.....	47
Figure 4.1: Robust and high throughput tumor spheroid formation assay.	55
Figure 4.2: Microfluidic platform for tumor spheroid invasion.....	58
Figure 4.3: IFs enable co-culture tumor spheroid dissociation.....	63
Figure 4.4: Time evolution of radial cell density profile to quantify tumor spheroid dissociation using azimuthally averaged radial cell intensity.....	64
Figure 4.5: IFs promote co-culture tumor spheroid dissociation via downregulating the E-cadherin of the non-tumorigenic MCF-10A cells	66
Figure 4.6: Confocal images of E-cadherin on single slices.....	67
Figure 4.7: IFs promoted amoeboid cell morphology of MDA-MB-231 cells.....	68
Figure 4.8: IFs promoted single over collective cell invasion of the MCF-10A cells from the co-culture spheroids.	69
Figure 4.9: MCF-10A cell morphology was not affected by IF..	70
Figure 4.10: IFs enhanced the cell motility and MSDs for malignant MDA-MB-231 cells invading out of the co-culture spheroids.....	71
Figure 4.11: No significant directional cell migration was observed for MDA-MB-231 tumor cells from the co-culture spheroids..	71
Figure 4.12: IFs enhanced the cell motility and MSDs for the non-tumorigenic MCF-10A cells invading from the co-culture spheroids.....	72
Figure 4.13: IF is not sufficient to induce MCF-10A spheroid invasion.....	74
Figure 4.14: IFs inhibit MDA-MB-231 tumor spheroid motility..	76
Figure 4.15: IFs inhibit MDA-MB-231 tumor spheroid ability to spread..	77
Figure 4.16: Interstitial flows promoted amoeboid cell morphology of tumor cells invaded out from the MDA-MB-231 spheroids....	78
Figure 5.1: Summary on the impacts of IF on tumor cell invasion in four experimental.....	82
Figure 5.2: IFs play differential role on cell-ECM and cell-cell adhesions.....	84
Figure 5.3: Microfluidic modeling of tumor transendothelial migration (TEM) under IFs.. .	87
Figure 5.4: Illustration of a microfluidic model recreating the biophysical microenvironment for tumor cell invasion studies.....	89

LIST OF TABLES

Table 1: Intramural flow rates and vessel diameters measured in healthy tissue and in tumors using animal models.....	3
Table 2: Interstitial flow rates measured in healthy tissue using animal models, and in tumors using animal models.....	5
Table 3: Summary on the roles of interstitial flows on lymphatic and blood morphogenesis and fibroblasts cell activities within a 3D ECM.....	5
Table 4: Detail on methods used to measure interstitial flow and the spatial location of the flow in animal models.....	7
Table 5: Summary on the roles of interstitial flows on tumor cell invasion using a modified Boyden chamber.....	8
Table 6: Vascular permeability measured <i>in vivo</i> and <i>in vitro</i>	13
Table 7: Hydraulic conductivity of ECM measured <i>in vivo</i> and <i>in vitro</i>	16
Table S1: Summaries of the experimental settings and results from three labs on the roles of interstitial flows on cell motility using microfluidic models.....	50

LIST OF ABBREVIATIONS

EC: endothelial cell

ECM: extracellular matrix

FN: fibronectin

FRAP: fluorescent recovery after photobleaching

IFs: interstitial flows

IFP: interstitial fluid pressure

TME: tumor microenvironment

PREFACE

The introductory chapter, chapter 1, consists of a perspective paper for which I am a first author “Microfluidic modeling of the biophysical microenvironment in tumor cell invasion” published in *Lab on a Chip*. The chapter is reproduced with permission of the publisher Royal Society of Chemistry. I acknowledge the contribution of my coauthors Jeffrey Segall and Mingming Wu. Chapter 3 consists of a paper for which I am first author “Interstitial flows promote amoeboid over mesenchymal cell motility of breast cancer cells revealed by a three dimensional microfluidic model” published in *Integrative Biology*. The chapter is reproduced with permission of the publisher Oxford University Press. I acknowledge the contributions of my co-authors Chih-Kuan Tung, Anqi Zheng, Beum Jun Kim and Mingming Wu. Chapter 4 consists a manuscript that is in preparation for submission. I acknowledge the contributions of my co-authors Yujie Ma, Carina Shiau, Cindy Wu, Jeffrey Segall, and Mingming Wu.

CHAPTER 1

INTRODUCTION

1.1 The tumor microenvironment (TME) in cancer metastasis

Cancer metastasis of solid tumors is a physical process where tumor cells generate sufficient forces to break away from the primary tumor, invade through the interstitial extracellular matrix (ECM), squeeze through vascular vessels, and establish a secondary tumor at a distant organ [1-3] (Figure 1). It is now well accepted that the tumor microenvironment (TME) plays an important role, similar to the genetic makeup of the tumor cells, in determining tumor cell invasiveness. While tumor genetics has always been the focus of tumor biology, it is only in recent decades that the critical roles of the TME have been recognized widely in the context of tumor cell invasion [4-9].

Broadly speaking, the complex TME can be classified into biochemical (e.g. cytokines secreted by cells and nutrients) and biophysical cues (e.g. fluid flows and ECM), as illustrated in Figure 1.1. Current tools for recreating the TME for tumor cell invasion are primarily Boyden chambers [10-12] and animal models [13-15]. Boyden chambers are straightforward to use, but difficult to recreate the complex TME and only provide population level and endpoint results. Animal models, on the other hand, provide a physiologically realistic environment, but are low throughput and it is difficult to isolate and control individual TME components. Microfluidic models have emerged to fill this gap [16-21]. Microfluidic models can allow for well-defined spatial and temporal arrangements of individual components of the TME, and facilitate quantitative analysis and mathematical modeling. In addition, they are compatible with optical imaging, enabling studies of single and collective cell dynamics in real time. We note that dynamic

analysis is important for tumor cell invasion studies because heterogeneity and plasticity are hallmarks of cancer [22-24]. In this work, we will focus on recent progress as well as future direction in the development of microfluidic devices for studying the roles of biophysical cues, specifically, biological flows and ECM, in driving tumor cell invasion. For microfluidic developments in the analysis of biochemical cues with applications in tumor cell invasion, please refer to recent excellent review articles [16, 25-27].

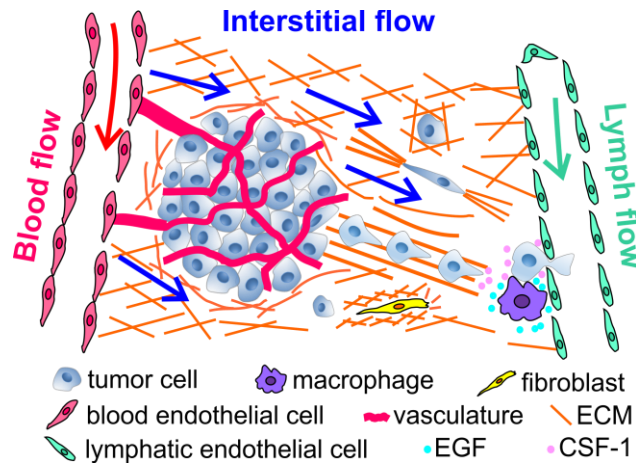


Figure 1.1: Important biophysical parameters in the tumor microenvironment (TME): intramural (blood and lymph) flows, interstitial flow, and the architectural support of extracellular matrices (ECM). Important biochemical parameters: cytokine gradients, nutrients, and oxygen, and multiple other cell types (stromal, immune, and endothelial cells).

1.2 Biophysical drivers in tumor cell invasion

1.2.1 Intramural flow in tumor cell invasion

Biological flows are ubiquitous in living systems and generally can be classified into intramural flows (blood and lymph flow) and interstitial flows (see Figure 1.1 and Table 1). Blood flow follows the large scale anatomical pattern, mainly aorta and arteries, with high flow speed in the order of tens of centimeters per second [28], and branches out to smaller scale arterioles and capillaries with lower flow speed, ranging from a few centimeters to a few hundred micrometers

per second [29]. In addition to nutrients and oxygen transport, shear stress from blood flow is known to be a critical regulator in vascular physiology [30] and morphogenesis during development [31-33], and is tightly linked to endothelial cell function [34-37]. Lymph flow, on the other hand, is several orders of magnitude smaller than blood flow, and has been reported to be on the order of a few millimeters per second in lymphatic vessels [38] and tens of micrometers per second in lymphatic capillaries [39].

Table 1: Intramural flow rates and vessel diameters measured in healthy tissue and in tumors using animal models.

	Healthy tissue	Tumor
Intramural flow	<u>Arterioles:</u> [29] diameter 15-60 μ m: 7-12 mm/s <u>Capillaries:</u> [29] diameter 5 μ m: 0.2 mm/s <u>Venules:</u> [29] diameter 18-72 μ m: 0.2-2.4 mm/s <u>Microlymphatic vessels:</u> [38] diameter 100 μ m: 1-7 mm/s <u>Lymphatic capillaries:</u> [39, 40] diameter 55 μ m: 0-29 μ m/s	<u>Blood vessels in mammary carcinoma:</u> [41] diameter 7-63 μ m: 0-0.8 mm/s <u>Blood vessels in glioma:</u> diameter 8-55 μ m: 0-0.5 mm/s [41] diameter 1-100 μ m: 0.001-10 mm/s [42] <u>Blood vessels in adenocarcinoma:</u> [43] arterioles 9-10 μ m: 0.59-0.7 mm/s capillaries 6-8 μ m: 0.09-0.27 mm/s venules 10-26 μ m: 0.09-0.22 mm/s

Blood/lymph flow within the TME is aberrant and its role in tumor cell invasion are largely unknown (see Table 1). Similar to normal tissue, blood flow in the TME is essential for tumor perfusion and growth. Different from the flow in normal tissue, blood flow in the TME is difficult to predict because of its dynamic nature. Blood flow rates within the TME are known to change with the abnormal growth of vascular vessels through angiogenesis, the physical stress from the fast growing tumor mass, and altered ECM mechanical properties. In addition, the blood vessels within the tumor are torturous, and often lack functional pericytes, basement membrane, and tight endothelial cell junctions [44-46]. Lymph flow within the TME has received much less attention, but is found to be elevated in contrast to healthy tissue [47].

The role of blood/lymph flow in tumor cell invasion are often attributed to the shear force regulation at the interface with endothelial cell (EC) layers. In order to disseminate to a distant organ, tumor cells must use the blood or lymphatic vessels as a conduit, and thus need to cross the EC layer [48-50]. Tumor cells are unlikely to enter/leave via the aortic or arterial vessels as those vessels have thicker walls and high shear stress. In contrast, blood capillaries with thinner walls and lower shear stress are more likely to physically trap circulating tumor cells for subsequent extravasation [3, 48, 51]. In parallel, lymphatic capillaries with significant slower flow at the host tissue are also sites where tumor cells prefer to reside [52]. Taken together, flow shear stress critically regulates the physiology of the vascular EC layers, and could potentially impact on tumor cell invasion.

1.2.2 Interstitial flow in tumor cell invasion

IF is a slow fluid movement through the interstitial space driven by hydrostatic and osmotic pressure differences between the arterial and venous or arterial and lymphatic vessels [53, 54]. First measured by the Jain lab using the fluorescence recovery after photobleaching (FRAP) technique, the flow speed associated with IF is typically on the order of a few micrometers per second in normal tissue (Table 2) [54]. While the main function of IF has long been known to drain waste fluids to the lymphatic system, recently it has been shown to regulate vascular morphogenesis [55-57] and align fibroblast cells and the matrix [58-60]. For details of the effect of IFs on endothelial cells and fibroblast cells, please see Table 3.

Table 2: IF rates measured in healthy tissue using animal models, and in tumors using both animal and human models.

	Healthy tissue	Tumor
Interstitial flow	<u>Rabbit ear tissue:</u> [54] 0.59±0.16 μm/s	Animal models: <u>VX2 carcinoma:</u> 0.55 ± 0.16 μm/s [54] <u>C6-pTET-VEGF tumor:</u> 0.1-0.5 μm/s [61] <u>Glioblastoma:</u> 0.25-0.8 μm/s [62] <u>Cervical carcinoma:</u> 1-7 μm/s [63] <u>Melanoma:</u> 1-9 μm/s Human patients: <u>Nonmetastatic squamous carcinoma:</u> 5-25 μm/s <u>Metastatic squamous carcinoma:</u> 10-55 μm/s

Table 3: Summary on the roles of IFs on lymphatic and blood morphogenesis and fibroblasts cell activities within a 3D ECM

Year	Author	In vitro Model	Flow speed	Cell type	Key findings	Ref.
2004	Ng <i>et al.</i>	Radial flow chamber	10 μm/s	Lymphatic and blood endothelial cells (LEC & BEC)	IF stimulated blood and lymphatic endothelial cell morphogenesis	[55]
2005	Helm <i>et al.</i>	Radial flow chamber	4.2μm/s	LEC & BEC	Synergistic effect of IF and VEGF direct capillary morphogenesis	[56]
2007	Helm <i>et al.</i>	Radial flow chamber	2.4-15.8 μm/s	LEC & BEC	Synergistic effect of IF and VEGF differentially modulate blood and lymphatic vessel morphogenesis in the matrix with various composition of fibrin and collagen.	[57]
2003	Ng <i>et al.</i>	Radial flow chamber	3.6–13 μm/s	Human dermal fibroblasts	IF induced fibroblasts aligned perpendicular to flow direction	[59]
2005	Ng <i>et al.</i>	Radial flow chamber	6.3μm/s	Human dermal fibroblasts	IF induced fibroblasts to myofibroblast differentiation	[58]
2006	Ng <i>et al.</i>	Radial flow chamber	5-13 μm/s	Human dermal and fetal lung fibroblasts	IF induced collagen fiber and fibroblast alignment in collagen matrix but not in fibrin.	[60]

Clinically, IF within the TME has been reported to be significantly higher in squamous carcinoma patients with metastatic status than those with non-metastatic status (Figure 1.2A) [63]. IF within the TME is elevated due to the heightened interstitial fluid pressure [63, 64] (Table 2). Elevated IF rates within the TME have been measured and documented in Table 2. For details of the measuring method and the location of IF where it was measured, please see Table 4. High interstitial fluid pressure in the TME, in part, is a result of the fact that excessive interstitial fluids could not be absorbed by the compressed non-functional lymphatic vessels within the tumor. It has been reported that the pressure is particularly high within a malignant tumor, and drops steeply at the tumor-host tissue interface using both mathematical modeling and *in vivo* measurement (Figure 1.2B and C) [63, 65]. For nearly three decades, high interstitial fluid pressure has been an important biomarker for tumor progression and a significant obstacle for cancer therapeutic delivery into the tumor [66-69].

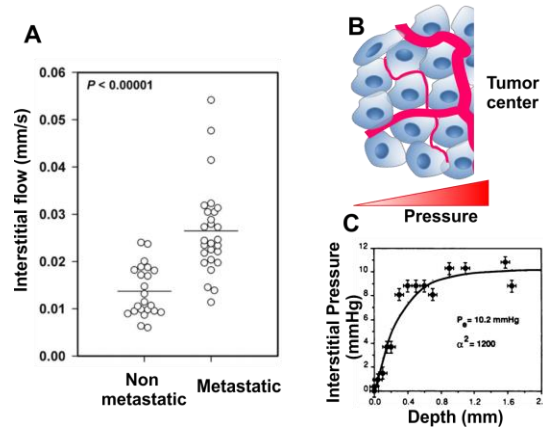


Figure 1.2: High interstitial fluid pressure and elevated IFs in the tumor. A. IF rates in non-metastatic vs. metastatic advanced squamous carcinoma patients. The plot is modified from reference [63]. B. Schematic of a semi-tumor. C. Mathematical model and *in vivo* measurement of interstitial fluid pressure within a tumor. The plot is modified from reference [66].

Table 4: Detail on methods used to measure IF and the spatial location of the flow in animal models.

Method	Location where the flow was measured	Flow rate	Ref.
FRAP	At the surrounding tissue	$0.55 \pm 0.16 \mu\text{m/s}$	[54]
MRI	At the tumor periphery	$0.1\text{-}0.5 \mu\text{m/s}$	[61]
Dynamic contrast-enhanced MRI	At the tumor periphery	$1\text{-}9 \mu\text{m/s}$	[63]
Dynamic contrast-enhanced MRI	Within the tumor	$0.25\text{-}0.8 \mu\text{m/s}$	[62]

Recently, the physical consequence of elevated and excessive interstitial fluid flow outward from the tumor to the host tissue has been investigated in the context of tumor cell invasion using *in vitro* models [70-72]. Using a modified Boyden chamber, the Swartz lab discovered that IF can guide tumor cell invasion along the flow direction. The unique feature of IF is that it operates in a region where the Peclet number (convective versus diffusive transport) is close to one. In other words, the transport of secreted cytokines is governed by both convective flow and diffusion. Computation of cell secreted cytokine transport shows that IF leads to flow-induced spatial gradients of secreted cytokines [56]. One example is the spatial gradients of lymphatic chemokine CCL19/21 along the flow direction, and breast tumor cells were discovered to follow the flow/gradient direction using a modified Boyden Chamber model [70]. More recently, IF was found to directly impact tumor cell mechanotransduction via CD44 in brain tumor cells [73] and via glycocalyx in renal carcinoma cells [74]. IF also has been shown to promote tumor cell invasion via stromal cell mediated matrix remodeling within the TME [75]. In summary, mounting evidence demonstrates that IF critically modulates tumor cell invasion behavior using the modified Boyden chambers. For details on the effect of IFs on tumor cell invasion using a modified Boyden chamber, please see Table 5.

Table 5: Summary on the roles of IFs on tumor cell invasion using a modified Boyden chamber.

Year	Author	In vitro Model	Flow speed	Cell type	Key findings	Ref.
2007	Shields <i>et al.</i>	Boyden chamber	0.2 $\mu\text{m/s}$	Breast cancer cells: MCF 10A MCF7 ZR75-1 MDA-MB-435S	IF induced CCR7-dependent autologous chemotaxis of tumor cells to lymphatic vessels.	[70]
2013	Munson <i>et al.</i>	Boyden chamber, radial flow chamber	0.72 $\mu\text{m/s}$	Glioma tumor cells: RT2, EGFP-RT2, U87MG, and C6	IF promoted CXCR4/CXCL12 mediated glioma tumor cell invasion.	[72]
2011	Shieh <i>et al.</i>	Modified Boyden chamber	0.5 $\mu\text{m/s}$	Human dermal fibroblast, IMR-90 fetal lung fibroblasts, MDA-MB-435S, DU-145, MDA-MB-231	IF promote TGF- β 1 and MMP dependent fibroblast migration and Rho-mediated contraction to locally reorganize collagen matrix, to enhance tumor cell invasion.	[75]
2013	Qazi <i>et al.</i>	Modified Boyden chamber	0.8–1.21 $\mu\text{m/s}$	human renal carcinoma cells: SN12L1 and SN12C	IF induced renal tumor cell invasion via glycocalyx mediated mechanotransduction	[74]
2016	Kingsmore <i>et al.</i>	Modified Boyden chamber	0.15–2 $\mu\text{m/s}$	Glioma stem cells: G2, G34, G62, and G528 cells	IF induced Glioma tumor cell invasion via CD44 mediated mechanotransduction along with CXCR4/CXCL12 chemosensing	[73]
2015	Tchafa <i>et al.</i>	Modified Boyden chamber	0.1 $\mu\text{m/s}$	Non-tumorigenic and breast tumor cells: MCF10A and MCF10A-ERBB2	IF induced ERBB2/HER2-expressing breast cancer cell invasion via activating phosphoinositide-3-kinase (PI3K)	[76]
2015	Shah <i>et al.</i>	Modified Boyden chamber	0.05 – 0.1 $\mu\text{m/s}$	Hepatocellular carcinoma cells: Huh7, Hep3B	IF promoted hepatocellular tumor cell invasion via CXCR4/CXCL12 chemosensing and MEK/ERK signaling	[77]

1.2.3 Extracellular matrix in tumor cell invasion

The extracellular matrix (ECM) is a major physical component that surrounds and penetrates solid tumors. Important physical ECM characteristics that are critical for tumor cell invasion include ECM overall stiffness and architecture [78, 79]. Stiffness, contributed mainly by dense and cross linked ECM fibrillar structures, is a prognostic and risk factor for breast cancer patients [80, 81]. Similarly, increasing evidence demonstrates that stiffer ECM promotes tumor cell invasion in *in vitro* assays [5, 82]. It has been found that malignant tumor cells and tumor associated stromal cells secrete collagen, which contributes to dense fibrillar structures [82]. They also express enzymatic cross linkers, such as lysyl oxidase, which increase the overall stiffness of the ECM [83, 84]. Breast tumor has been reported to be twenty times stiffer than the normal breast tissue [5].

Recent developments in intravital imaging reveal that tumor ECM is highly heterogeneous in space, and evolves with time [85-87]. This is not surprising because tumor and stromal cells are known to actively pull onto the ECM, and thereby remodel the ECM architecture [75, 88, 89]. Collagen bundles have been reported to align perpendicularly to the tumor periphery, possibly by active tumor and stromal cell contraction, facilitate collective tumor cell invasion and correlate with malignancy [90, 91]. Micro-tunnels, hollow micro-sized tunnels with diameter range of 1-30 μm , were recently observed to provide tumor cells fast moving pathways both *in vitro* and *in vivo* [92-94]. These hollow micro-sized tunnels are created by the degradation of collagen matrices via matrix metalloproteinase (MMP) secreted by the tumor and stromal cells. In the context of ECM architecture, the three dimensional nature of the ECM has been discussed extensively in the cell migration community and can be a critical regulator of cell migration [95-97].

1.3 Current state of art on microfluidic modeling of biophysical microenvironment in tumor cell invasion

Microfluidics has emerged to model the TME because of its tight control of flow rates within a 3D ECM. A good microfluidic model needs to be able to recreate blood/lymphatic vessels of appropriate physiological size and shape within a 3D ECM, with controlled flow rates. In addition, the microfluidics should be robust and high throughput. Here, we discuss current efforts in modeling the biophysical aspects of the TME using microfluidic devices. The goal is to create on chip vascular vessels and ECM with architecture, dimensions and flow rates closely mimicking the *in vivo* measurement results (see Tables 1 and 2). We emphasize the mathematical modeling of the flow rates/shear stress within the microfluidic platform using the relevant physical parameters including vascular permeability of endothelium layers (Table 6) and hydraulic conductivity of ECM (Table 7).

1.3.1 Microfluidic models for intramural flow in tumor cell invasion

A critical step for modeling intramural flow in the context of tumor cell invasion is to engineer a perfusable and functional vascular tube/network within a 3D ECM. Motivated by the development of vascularized biomaterial, early work began with the engineering of an endothelial cell (EC) tube in one single microfluidic channel within dense type I collagen matrices. The microfluidic channel was created through a micro-molding method, in which a hypodermic needle or a microfabricated PDMS positive channel feature was used as a template, and hydrogels as molding materials. After removing the template, ECs were introduced into the channel and formed an EC monolayer [98-103]. A recent alternative method for creating a single EC tube is through introducing a less dense fluid into a dense fluid (un-polymerized collagen) via a process known as

viscous fingering [104-106]. This method does not require microfabrication thus is cost effective, the downside being that it lacks precise control over the size of the vessel.

More complex 3D vascular networks embedded within synthetic or naturally derived matrices have been developed recently using a sacrificial method [107-111]. Here, one first creates an interconnecting fiber network using either microfabrication or 3D printing with sacrificial materials that are compatible with cell culture (e.g. gelatin and carbohydrate glass). The polymerized gelatin or solidified carbohydrate glass fiber network is then submerged within synthetic or naturally derived gels. After removing the sacrificial layers, ECs are introduced into the network to form lumens. We note that autonomous formation of microfluidic vascular networks by placing ECs in biomatrices along with a set of well-defined reagents and/or fluid flow that promote angiogenesis [112-114] and lymphangiogenesis [115] have been successful and been used in the context of drug delivery. This method can potentially be introduced for the purpose of tumor cell invasion.

An important way that intramural flow regulates tumor cell intravasation/extravasation is through the alteration of EC layer integrity and permeability via flow induced shear stress (Table 6). A key parameter that is commonly used to characterize the transport of solute across an endothelium layer is the permeability coefficient, $P(\text{cm/s})$, which is defined as $J_s/\nabla C$, where J_s ($\text{g/cm}^2/\text{s}$) is the solute flux through a unit area, ∇C (g/cm^3) is the spatial gradient of solute concentration. In Table 6, we list permeability of both blood and lymphatic vessels measured in healthy and tumor tissues. It is interesting to note that one *in vivo* study by Gerlowski *et al.* revealed that the vascular permeability is significantly increased in tumor compared to normal vasculature [116], echoing the notion that tumor vasculature is leakier than healthy vasculature. We also note that error bars for these measurements are typically large. Looking forward, the microfluidic

platform allows us to make precise spatial arrangement of solute concentration, obtain temporal information of the concentration field, and thus has the potential to improve the permeability measurements in the future.

Shear stress from the intramural flows are known to alter EC permeability as well as integrity. Flow induced shear stress has been reported to increase the barrier function or lower the permeability coefficient of the EC layer [103, 117, 118] and suppress VEGF-driven EC sprouting [119]. Progress has been made to incorporate tumor cell laden ECM into a single engineered microfluidic blood vessel or vascular networks for dynamic tumor trans-endothelial migration [100, 103, 118, 120-122], making it possible to examine quantitatively the impact of intramural flow on tumor cell invasion. Using a microfluidic model, we have learned that blood flow through the capillaries reduces tumor cell extravasation rates [118]. This is not surprising because the EC layer junction is strengthened under flow shear stress, and increases its ability to prevent transmigration. From another study, we learned that blood flow strengthened the endothelial layer of an engineer blood vessel, but the vessel integrity was disrupted by the periphery tumor cells that are undergone mitosis, allowing tumor cell intravasation [123]. It is interesting to note that lymph flow on the other hand, promotes intravasation using a flow chamber modified from the Boyden chamber [124]. This discrepancy can likely be explained by the differential responses of blood and lymphatic vessels to flow shear stress. In this context, a tight control over the flow rates, in which microfluidic models have the advantages over other conventional models, will allow us to gain a deeper understanding of the impact of intramural flow on tumor cell transmigration.

Table 6: Vascular permeability measured *in vivo* and *in vitro*. Vascular permeability (or permeability coefficient across an endothelium layer), *P*, is the ratio of solute flux and solute concentration gradient across the endothelium layer [125].

	In vivo		In vitro modeling
	Heathy tissue	Tumor	
Permeability across blood and lymphatic endothelium [cm/s]	<u>Capillaries and postcapillary venules</u> [116]: (for dextran MW=150,000) $7.26 \pm 3.29 \times 10^{-8}$	<u>Capillaries and postcapillary venules in VX2 carcinoma</u> [116]: (for dextran MW=150,000) $5.7 \pm 3.9 \times 10^{-7}$	<i>In transwell:</i> <u>EC monolayer</u> [131]: (for Albumin) 5.6×10^{-6}
	<u>Postcapillary venules</u> [126]: (for sodium fluorescein) $1.4 \pm 0.11 \times 10^{-5}$ (for α -Lactalbumin) $4.4 \pm 0.5 \times 10^{-7}$ (for BSA) $4.9 \pm 0.32 \times 10^{-8}$	<u>Microvascular in adenocarcinoma</u> [129]: (for BSA) $6.06 \pm 4.30 \times 10^{-7}$	<i>In microfluidics:</i> <u>Hollow EC lumen with tumor cells</u> [121]: (for 10kDa) $4.08 \pm 1.11 \times 10^{-5}$ (for 70kDa) $7.5 \pm 0.93 \times 10^{-6}$
	<u>Postcapillary venules</u> [127]: (for 4kDa dextran) $9.2 \pm 4.6 \times 10^{-7}$ (for 10kDa dextran) $3.1 \pm 1.3 \times 10^{-7}$ (for 20kDa dextran) $2.4 \pm 1.0 \times 10^{-7}$ (for 40kDa dextran) $1.9 \pm 1.1 \times 10^{-7}$ (for 70kDa dextran) $1.5 \pm 0.5 \times 10^{-7}$	<u>Arterioles and venules in mammary adenocarcinoma</u> [41]: (for BSA) $1.7 \pm 0.6 \times 10^{-7}$ $2.9 \pm 1.5 \times 10^{-7}$ $1.9 \pm 0.5 \times 10^{-7}$	<u>Single blood EC tube</u> [98, 102] (for BSA) $5.5 \pm 3.5 \times 10^{-6}$ $7.9 \pm 3.5 \times 10^{-6}$ (for 70kDa dextran) $4.1 \pm 0.5 \times 10^{-6}$ (for 332Da fluorescein) $7.0 \pm 1.5 \times 10^{-6}$
	<u>Venules</u> [128]: (for RSA) $3.5 \pm 1.0 \times 10^{-7}$	<u>Arterioles and venules in glioblastoma</u> [41]: (for BSA) $3.8 \pm 1.2 \times 10^{-7}$ $1.1 \pm 0.5 \times 10^{-8}$	<u>Self-assembled blood vessels</u> [112, 118]: (for 70kDa dextran) $8.9 \pm 3.1 \times 10^{-7}$ (for 70kDa dextran) 4.5×10^{-7} (for 150kDa dextran) 1.2×10^{-7}
	<u>Collecting lymphatic vessels</u> [128]: (for RSA) $4.0 \pm 1.0 \times 10^{-7}$	<u>Vasculature in squamous carcinoma</u> [130]: (for 3.3kDa dextran) 1.54×10^{-5} (for 40kDa dextran) 9.5×10^{-7} (for 2MDa dextran) 1.7×10^{-7} (for BSA) 4.9×10^{-7}	

1.3.2 Microfluidic models for IF in tumor cell invasion

Broadly speaking, there are two types of assays for creating IFs. One is the modified Boyden Chamber assay and the other is the microfluidic platform (Fig. 1.3). The modified Boyden Chamber assay uses a commercially available platform, and is straightforward to implement, but

results are population based and end points. The microfluidic platform, on the other hand, allows for dynamic and single cell imaging, but is typically difficult to make, requiring engineering training for the users. Here, we discuss the evolution of several platforms developed to date for creating IFs. We will highlight biological insights gained using these platforms in the context of tumor cell invasion.

Pioneering work on roles of IFs in tumor cell invasion was carried out in a modified Boyden chamber [70]. A layer of tumor cell embedded biomatrix was introduced into the insert of a Boyden chamber. IF is gravity driven, facilitated by the fluid level difference between the fluid within the insert and the cup surrounding it (Fig. 1.2A). Type I collagen, a main structural component of mammalian tissue, has been used in most of the current studies for its ability to mimic *in vivo* ECM architecture and compatibility with cell invasion assay [94]. In addition, the mechanical properties [89, 132, 133] and specific hydraulic conductivities (Table 7) of collagen gels have been studied and documented extensively in the literature from the biomaterials community. Here, the readout is the total number of cells transmigrated through the porous membrane after experimental time. Using the modified Boyden chamber, a number of biological insights have been gained (Table 5) [70, 72], most notably the autologous chemotaxis of breast tumor cells mediated by flow induced lymphoid chemokine gradients.

Although the modified Boyden chamber assay is straightforward to use, the results are population based and end points. One of the hallmarks of tumor cells is the heterogeneity of a single cell population. It is thus important to develop assays that are amenable to single cell analysis. Microfluidic platforms have emerged to model IFs. A critical component for modeling IF through 3D ECM in a microfluidic platform is to confine natively derived or synthetic ECM within an area where fluid flow can be applied through the ECM in a controlled way. To create a

microfluidic platform for tumor cell invasion in the presence of IF, a number of labs have developed unique microfabrication methods to pattern type I collagen in a three parallel channel configuration [134-138]. The common feature of all the devices is to develop micro-patterned structures to confine biomatrices in designated places. In the work of Hassler *et al.* or Polacheck *et al.*, tumor cells embedded in collagen (unpolymerized) are introduced into a channel lined with two parallel lines of micropillars (see red or green channel in Figure 1.3. B and C). IF is introduced in the horizontal direction after gel polymerization. This configuration has advantages over the early engineering method for vascular tube using micro-molding method for its flexibility of the channel layout, and also for its ease of integrating tumor cells within ECM. The use of spaced micropillars utilizes surface tension to confine the un-polymerized collagen solution, while leaving space between the micropillars for IF to pass through the polymerized collagen matrices. This method offers robust confinement of the ECM, but the micropillars block a significant amount of the flow and complicate the spatial distribution of the flow field (see right panel in Figure 1.3. B). To overcome this limitation, our lab confined cell-embedded collagen using a contact line pinning method [136, 137]. In our work, parallel PDMS microridges (or contact lines) with a cross section of 10 μm by 5 μm were fabricated to confine collagen within a wall-less channel (a channel with nearly no walls). This method allows IF to run through the collagen matrices with over 80% spatial uniformity in the area of interest. For details of the device designs, see Figure 1.3D.

Darcy's law is often useful for computing IFs during the device design stage. For a given layout of the device, one can compute accurately the flow rates in different parts of the channels by applying the Brinkman equation in a multi-physics software package such as COMSOL. A key parameter required is the hydraulic conductivity, K' , of the biomatrices. Hydraulic conductivity is defined through Darcy's law, $K' = J/\nabla P$, where J is the fluid flux, ∇P is the spatial pressure

gradient. Because of the small dimension of the system, fluid flows are slow, and Darcy's law is typically valid [136]. Values of hydraulic conductivity of healthy and tumor tissue, as well as reconstituted ECM are listed in Table 7. We note that hydraulic conductivity times fluid viscosity, $K'\eta$, named specific hydraulic conductivity (K), is typically reported in *in vitro* ECM measurements.

Table 7: Hydraulic conductivity of ECM measured *in vivo* and *in vitro*. Hydraulic conductivity, K' is the ratio of fluid flux and pressure gradient as defined in Darcy's law. Specific hydraulic conductivity (K) is $K'\eta$, where η is the fluid viscosity.

	In vivo		In vitro modeling
	Heathy tissue	Tumor	
Hydraulic conductivity of ECM	Hydraulic conductivity (K') [$cm^2/mmHg \cdot s$] (From references [139] and [140])		Specific hydraulic conductivity (K) [cm^2]
	<u>Abdominal muscle:</u> 1.5×10^{-7} to 7.8×10^{-7}	<u>HSTS 26T sarcoma:</u> 9×10^{-8}	<u>Type I collagen matrices</u> [141]: 3mg/mL: 3×10^{-7} 8mg/mL: 3.5×10^{-8} 10mg/mL: 7.5×10^{-9} 15mg/mL: 9×10^{-10} 20mg/mL: 1.5×10^{-10}
	<u>Dermis:</u> 5.3×10^{-8}	<u>U87 glioblastoma:</u> 6.5×10^{-7}	<u>Type I collagen matrices</u> [142]: 10mg/mL: 1×10^{-11}
	<u>Tail skin:</u> 7×10^{-7} to 1.5×10^{-6}	<u>LS174T carcinoma:</u> 4.5×10^{-7} <u>MCAIV carcinoma:</u> 2.5×10^{-6}	

Using the microfluidic platform developed, we have started to learn how IFs modulate tumor cell heterogeneity and plasticity. This information is difficult to obtain in population level assays such as the Boyden Chamber assay. Haessler *et al.* showed that IF at flow speed of 10 $\mu\text{m/s}$ enhanced a subpopulation of breast tumor cell migration, highlighting the heterogeneous nature of tumor cells within a single population [135]. Work in our lab demonstrated that IF at flow speed of 2 $\mu\text{m/s}$ promotes amoeboid over mesenchymal motility of breast cancer cell invasion by carrying away adhesion molecules such as fibronectin. Cells lacking adhesion contacts prefer to migrate via amoeboid motility [137]. These studies revealed critical information on how IF

influences tumor cell invasion at the single cell level and the dynamic interaction of tumor cells with their environment. The Kamm lab learned that IF can impact tumor cell migration directly via chemosensing or mechanosensing molecules. In the case of chemosensing, Polacheck *et al.* demonstrated that IF at flow speeds of 0.3 and 3.0 $\mu\text{m/s}$ induced directional migration of breast tumor cells along/against the flow direction in a chemokine receptor CCR7 dependent manner [134]. In later work from the Kamm lab, they reported that the directional migration of breast tumor cells along/against IF was triggered by mechanosensing molecules [138].

Taken together, a quantitative understanding how IF impacts tumor cell invasion within 3D ECM has just begun. Results from these studies are far from converging into a coherent theoretical understanding. Current reported results are very sensitive to experimental conditions, and differ from lab to lab. In particular, it is known that the conditions under which collagen is polymerized is critical in determining collagen fiber architecture, including pH [143], polymerization temperature [144], as well as the actual reagents used. It is thus of paramount importance to carefully record all the detailed cell culture condition for an eventual unified understanding. Looking ahead, many questions remain to be explored. The comparative roles of chemosensing or mechanosensing in the presence of IF remain to be investigated, as well as whether IF drives collective cell migration [145]. The latter is important because increasing evidence has suggested that collective cell migration may contribute to cancer cell survival and successful metastasis [146-148]. Current studies are limited to mainly breast tumor cells, but similar microfluidic platforms can be easily extended to study other cell types such as brain tumor cells [72, 73] and ovarian tumor cells [149].

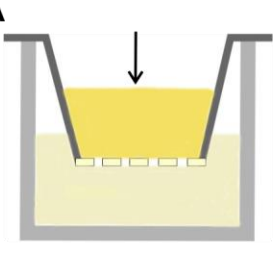
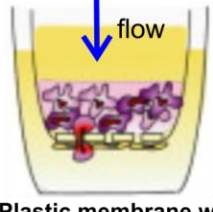
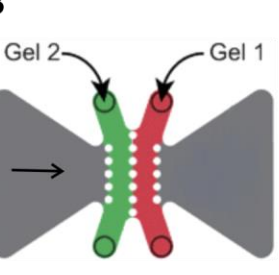
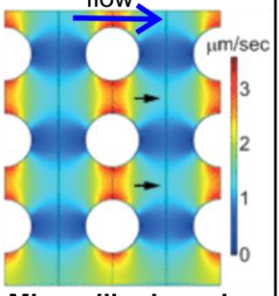
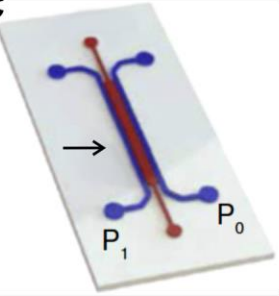
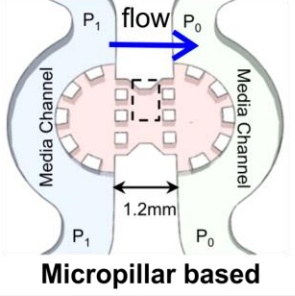
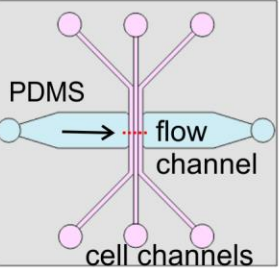
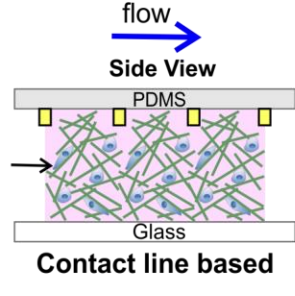
	Device design	Key feature	Advantages/ Disadvantages	Biological insights
Modified Boyden Chamber		 Plastic membrane with micro-sized pores	+ Easy to use + High throughput - Average and population level results	Interstitial flow induced breast tumor cells invasion via autologous chemotaxis [61].
Microfluidic Platform		 Micropillar based	+ Tunable flow rates + Capable to recreate a more complex tumor environment + Allow single cell dynamic studies - Nonuniform fluid flow through the ECM	Only a subpopulation of breast tumor cells respond to interstitial flow because of the heterogeneous nature of cancer cells [116].
		 Micropillar based	+ Capable to recreate a more complex tumor environment + Allow single cell dynamic studies - Nonuniform fluid flow through the ECM	Interstitial flow induced directional migration of breast tumor cells via chemosensig receptors and mechanosensing molecules [65, 115].
		 Contact line based	+ Uniform flow through the ECM + Can incorporate both interstitial and intramural flows + Allow single cell dynamic studies - Restrict to surface properties	Interstitial flow promoted amoeboid over mesenchymal motilities of breast tumor cells via adhesion molecules [118].

Figure 1.3: Modeling IFs in tumor cell invasion studies. A, Modified Boyden chamber platform. Tumor cell embedded biomatrix is introduced into a Boyden Chamber insert, which is placed in a well. The gravitational pressure, provided by the fluid level difference between the fluid within the insert and that in the surrounding well, drives the IF. The invasion rate is marked by the number of cells transmigrated through the porous membrane at the bottom of the insert. B,C,D: Three different microfluidic platforms for modeling IFs. B. In this device, lines of pillars with circular cross section of diameter 500 μm are used to confine collagen. IF is driven by gravity along the horizontal direction. Numerically simulated flow field is shown in the right panel of B. C: In this

device, lines of square pillars, each with a cross section of $250\ \mu\text{m} \times 250\ \mu\text{m}$, are used to confine collagen. Gravity driven flow is introduced horizontally across collagen matrices. D: In this device, contact lines with cross section of $10\ \mu\text{m} \times 5\ \mu\text{m}$ are used to confine collagen within the cell channel. IF is introduced using a syringe pump in the horizontal flow channel. Image on the right side of panel A is reproduced from reference [70], with permission from Elsevier. Images in B are reproduced from reference [135] with permission from the Royal Society of Chemistry. Images in C are reproduced from references [134, 138] with permission from the Proceedings of the National Academy of Sciences, and images in D are reproduced from reference [137] with permission from the Royal Society of Chemistry.

1.3.3 Microfluidic models for coupling intramural and IFs in tumor cell invasion

In vivo, both IF and intramural flow coexist. Recent progress has been made in recreating both interstitial and intramural flows within one experimental setup in the context of tumor cell invasion. Tung *et al.* developed a microfluidic device that allows for the introduction of intramural flow, and at the same time controlling IF. This device can potentially be used to study tumor cell invasion and transmigration in the presence of both flow types [136]. The Swartz lab developed an experimental platform that integrates a Boyden chamber and a flow channel, in which IF was introduced through the Boyden chamber and intramural flow was introduced through a flow channel underneath the Boyden chamber [124]. Using this platform, they revealed for the first time that IF and lymph flow synergistically increase tumor cell transmigration rates through lymphatic vessels. We note that currently, microfluidic platforms that include both interstitial and intramural flows for tumor cell transmigration are at early stages of development.

1.3.4 Microfluidics for modeling ECM architecture in tumor cell invasion

Microfabricated devices provide a unique opportunity for decoupling the contributions of individual ECM properties (e.g. alignment and pore size) from tumor cell invasion, enabling a mechanistic understanding of cell-ECM mechanical interactions.

Two important features within the TME that promote fast and persistent tumor cell invasion are aligned collagen fibers and embedded hollow micro-sized tunnels. To investigate molecular mechanisms that cells use to migrate along one dimensional (1D) collagen fibers, synthetic 1D tracks have been fabricated, including nano/microfabricated topographic lines and fibronectin lines that have line widths ranging from submicrometer to tens of micrometers [95, 150, 151]. While these engineered lines are straightforward to produce and easy to manipulate, the disadvantage is that these lines are made on a 2D surface which do not recapitulate the 3D *in vivo* situation where cells are supported by fiber network around all surfaces. Alternative methods have been developed to circumvent this limitation. One way of producing aligned collagen fibers within a 3D ECM is to use shear stress. One can flow un-polymerized collagen through a micro-sized channel in microfluidics, and the flow shear force has been shown to be able to align collagen fibers along the flow direction [152-155]. A second method is to flow a less dense collagen solution (low concentration) into a dense solution (Matrigel solution at high concentration) within a channel to form aligned collagen fibers at the gel interface [156]. A third method is to repeatedly stretch and relax a collagen fiber network already polymerized on a 2D substrate [157]. Recently, self-assembled micro-sized magnetic bead strings embedded within hydrogel have been used as mimics of 3D collagen fibers for the purpose of tumor cell invasion studies [158]. These studies revealed that alignment promote directional cell migration by limiting the cellular protrusion sites within the line/fiber or contact guidance. In addition to 1D topography, confined micro-tunnels have been discussed extensively as a highway for tumor cell migration recently. Microfabricated tunnels/channels surrounded by collagen provide a controlled way to study molecular mechanisms that cells use to migrate through these tunnels. Interestingly, MMPs are required for making these

micro-tunnels in the first place, but then existing microfabricated tunnels facilitate MMP independent tumor cell invasion [159, 160].

A limiting factor for tumor cell migration within the 3D ECM network is the nucleus, which is the stiffest part of a cell. It has been reported that tumor cells fail to migrate when their nucleus size is larger than the ECM pore size [161]. To understand the nuclear mechanics, microfluidic models have been developed to precisely mimic the constrictions presented to the cells by the ECM pores. Here, an array of micropillars with a few micrometers spacing is fabricated on a substrate [162-164]. Nuclear envelope rupture and DNA damage is observed when tumor cells squeeze through gaps with spacing smaller than the nucleus. Interestingly, the majority of tumor cells are seen to self repair and survive [164, 165].

With the rapid progress in biomaterials, we can now fine tune the stiffness of type I collagen as well as its architecture individually or together, enabling a mechanistic understanding of the role of mechanical properties of ECM in tumor cell invasion. Increasing collagen concentration is a simple and straightforward method for increasing gel stiffness, however, this generates significantly smaller pore sizes at the same time [141, 161, 166]. A number of other techniques have been developed to increase the collagen stiffness without altering the concentration, they include varying polymerization temperature [144, 167] and pH [143], nonenzymatic cross-linking of the fibers [168, 169], and applying mechanical tension [153, 170]. Future development requires integrating these biomaterial manipulation techniques with microfabricated device to pattern precisely the matrix stiffness or pore size in space for high throughput studies of tumor cell-ECM interactions.

1.4 Overview and aims for this dissertation

This dissertation focuses on examining the roles of IFs in breast tumor cell invasion. The primary aims of this dissertation are to i) develop a microfluidic platform that is capable of generating well-defined microenvironment for breast tumor cells that is physiologically relevant including IFs and three-dimensional extracellular matrices; ii) investigate the roles of IFs in breast tumor cell and spheroid invasion using the microfluidic platform.

CHAPTER 2

Development of a contact line pinning microfluidic device for interstitial flows

2.1 A need for developing microfluidics that can generate well-defined IFs

Tumor cells are known to behave differently in response to the complex TME [171]. To better understand the heterogeneity and plasticity of tumor cells, there is a need for tools that can capture the dynamics of tumor cells in real time. Although modified Boyden chamber models have played instrumental roles in revealing effects of IFs on molecular mechanism governing tumor cell invasion [70, 72, 75], these results are limited in endpoints and population levels. Recently, microfluidic models have emerged for studying effects of IFs on tumor cell invasion because of their compatibility with optical microscope, making it possible to follow single-cell dynamics in both time and space [134, 135, 172]. In addition, microfluidic models have the advantage of providing well controlled microenvironments, such as fluid flows within a 3D ECM [173].

2.2 Design principles for a contact line pinning microfluidic device

A microfluidic device using the contact line pinning method was developed earlier in our lab with a goal to generate well-defined intramural and IFs [136]. The idea of contact line pinning came from the well-known phenomenon known as coffee ring effect. When a spilled drop of coffee dries on a surface, the coffee particles were carried by the outward flow. The particles then are deposited mostly at the perimeter of the drop and the buildup particles serve as a contact line (Figure 2.1A), resulting the ring shape stain [174]. The basic idea of contact line pinning is to increase the fluid contact angle with a solid surface, as a result to confine the fluid from moving further, as illustrated in Figure 2.1B. Recently, microfabrication techniques were incorporated to micropattern contact lines for microfluidic application to guide fluid flows [175]. In our work, we

microfabricated micro-sized contact lines and patterned onto our microfluidic model to pin or confine cell embedded matrix within a desired channel.

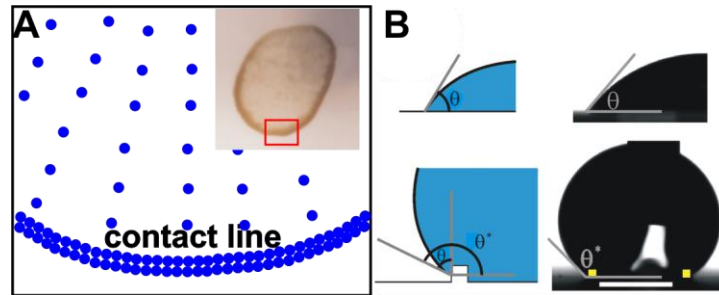


Figure 2.1: Illustration of contact line pinning idea. A. coffee ring effect: a region of a drop of coffee (insert) illustrating particles accumulated towards the edge of a ring and form a contact line [174]. B. Enhancement of the contact angle of a water drop on a flat substrate by a microfabricated ridge (white/yellow square) in illustration (left column) and micrographs (right column). The initial contact angle was increased from $51^\circ(\theta)$ without ridge to $139^\circ(\theta^*)$ with ridge. Figure B is modified from Tung *et al.* in reference [172].

The microfluidic device design is illustrated in Figure 2.2. The device includes three cell channels, each with a cross section of $400\ \mu\text{m} \times 200\ \mu\text{m}$ for tumor cells embedded in 3D matrices and a flow channel with a cross section of $3\ \text{mm} \times 200\ \mu\text{m}$, where fluid flow will be applied (Figure 2.2A). Parallel contact lines are patterned in between two neighboring cell channels as well as the interface of the cell and flow channels (Figure 2.2 B). The cross section of each contact line is $10\ \mu\text{m} \times 5\ \mu\text{m}$. The purpose of the contact lines is to confine cell embedded collagen solution within a desired cell channel, so that IFs can run through the cell-matrix without blockage (only 2.5% blockage from the flow direction). Figure 2.2C demonstrates a collagen matrix is confined within the middle cell channel in the device.

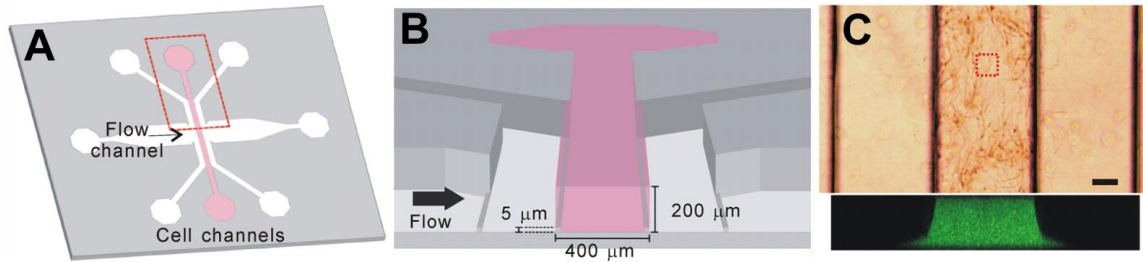


Figure 2.2: Design principle of a contact line pinning based microfluidic device for modeling IFs. A and B. Schematics of the microfluidic device in top view and side view. B is a zoom in of the rectangle outline in red dashed lines shown in A. C. Micrograph of collagen matrix confined within the middle cell channel. Scale bar is 100 μm . Figure C is modified from Tung *et al.* in reference [172].

2.3 Fabrication of the microfluidic device

The master mold for the microfluidic device was made using the standard photolithography technique at the Cornell Nanoscale Science and Technology Facility (CNF). The negative features on the silicon master were made using a two-step etching method. The layer with 5 μm height ridges was etched first, followed by a second layer etching for the 200 μm deep channels. The positive features shown in Figure 5 were made in the PDMS replica from the silicon mold. For the most recent generation of the device, we added two contact lines (10 μm in width and 5 μm in height) on the surface of the flow channel to avoid trapping air bubbles when initially introducing IFs into the flow channel [175].

The fabrication method was adapted from reference [172]. To obtain the ridge layer, positive photoresist (Microposit S1813, Shipley, Marlborough, MA, USA) was first spun on a 4" silicon wafer at 3000 rpm for 45 sec, baked at 115°C for 1 min, and then exposed on a contact aligner (Karl Suss MA/BA 6 aligner, Suss Microtech, Garching, Germany) at a dosage of 128.7 mJ/cm². The exposed photoresist on the wafer was developed using the program MF-321 for 60 sec (HamaTech-Steag Wafer Processor, Santa Clara, CA, USA), the wafer was then etched for 5 μm using a deep silicon etching method (Unaxis 770 Deep Silicon Etcher, Oerlikon, Pfäffikon,

Switzerland). To obtain the channel layer, photoresist (Megaposit SPR220-7.0, Shipley) was spun at 2500 rpm for 40sec, baked at 115°C for 90 sec, and then exposure at a dosage of 1.05 J/cm². After waiting for 90 min, the wafer was developed using the program AZ 726 MIF for 90 sec and then etched for 200 µm. After stripping the photoresist for 60 min (Anatech Plasma Asher, Anatech USA), the clean wafer was coated with a single layer of FOTS (1H,1H,2H,2H-Perfluorooctyl Trichlorosilane) using a vapour deposition method (Molecular Vapor Deposition, Applied Microstructures, San Jose, CA, US) to help release of PDMS from the silicon master. For repetitive device usage, standard 10:1 PDMS base to curing agent (SYLGARD 184 Silicone Elastomer Kit, Dow Corning, Midland, MI, US) was used to make the inversed PDMS replica from the silicon master.

2.4 Microfluidic device preparation

A critical step to confine collagen successfully within the cell channels using the contact lines is to make sure that the hydrophilicity of the PDMS is optimal. The following steps have been optimized to achieve this goal. Before each experiment, PDMS devices were first made from the silicon mold and then autoclaved. Second, PDMS devices were treated with oxygen plasma (Harrick Plasma Cleaner PDC-001, Harrick Plasma, Ithaca, NY) for 30 seconds on high power mode and left in a laminar hood for 5 hours in room temperature. Finally, the PDMS device was sandwiched between a Plexiglas manifold and a standard 1" × 3" size glass slide, supported by a metal frame at the bottom. After assembling, 0.6% of agarose solution was prepared to fill the void space around the PDMS device to prevent medium from evaporating during cell experiment. In a typical experiment, two microfluidic chips were assembled in parallel and stored at 4°C for 30 minutes before cell seeding.

2.5 IF measurement and validation within the 3D microfluidic device

Fluorescence recovery after photobleaching (FRAP) method was used to measure the flow speeds through the collagen matrix (see Figure 2.3 and Ref. [172]). For each measurement, 1.5 mg/mL collagen solution was first introduced into the three cell channels and polymerized in the same way as discussed (Figure 2.3A). Second, a 10^{-4} M fluorescein sodium (Fisher Scientific, Pittsburgh, PA) solution was pumped into the flow channel, and through collagen matrix using a syringe pump (KDS-230, KD Scientific, Holliston, MA). Third, a focused light spot ($\sim 400\mu\text{m}$ in diameter) was brought to the location of interest (Figure 2.3B at positions a, b, c in Fig. 2.4A) for 6-8 seconds using a high magnification lens (40X, NA=0.6, Olympus) together with a xenon lamp (LB-LS-30 Sutter Instrument, Novato, CA, USA). A series of 11 images (on GFP mode) were immediately captured at an interval of 1.5 second using a low magnification lens (4X, NA=0.13, Olympus). Finally, the images were post processed using ImageJ to obtain the flow speeds. This measurement was repeated at five different pumping flow rates (0.05 – 0.25 $\mu\text{L}/\text{min}$).

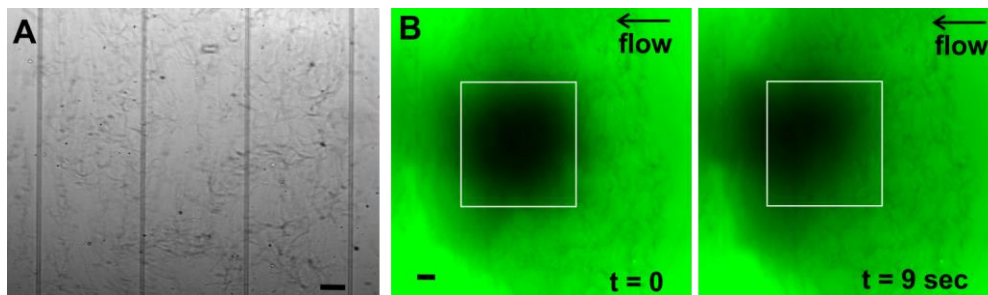


Figure 2.3: IF measurement using fluorescence recovery after photobleaching (FRAP) method. A. Bright field image illustrates collagen is filled in three cell channels for the FRAP measurement. B. Fluorescent images of photobleached spot at $t = 0$ sec (left) and $t = 9$ sec (right). Scale bars are 100 μm .

The flow within the device was characterized and validated using both computational and experimental methods (Figure 2.4). The computed flow speed using a multiphysics program

(COMSOL) within the device showed that the flow speed was uniform within the central portion of the three cell channels. The speed variation was less than 8.0% in the central 80% of the cell channels (Fig. 2.4A). This spatial uniformity of the flow was verified in experimental measurements as shown in Fig. 2.4B. Here, the IF speeds at three different spatial locations a, b, and c (as marked in Fig. 2.4A) within the collagen matrix were obtained using a FRAP technique [172, 176]. The measured flow speeds at three spatial locations were essentially the same within experimental uncertainties, confirming the spatial uniformity of the flow speed within the device. Furthermore, the experimentally measured flow rates were validated against the calculated values as shown in Fig. 2.4C. We note here that the advantage of using the contact line pinning based method is the spatial uniformity of the flow speed within the collagen matrix.

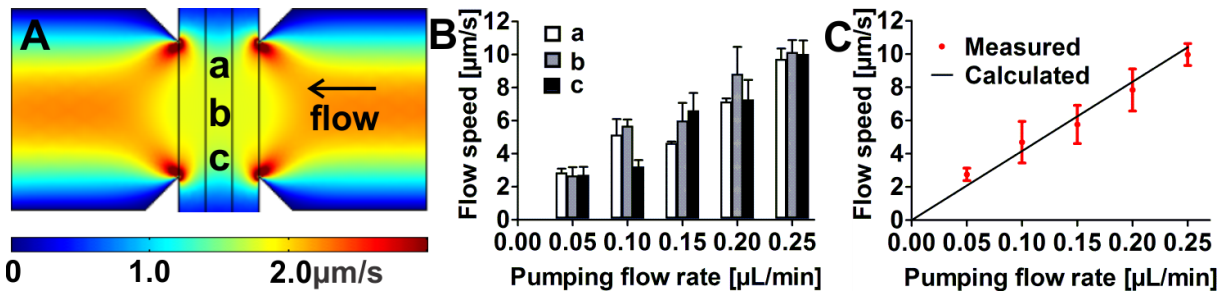


Figure 2.4: IF measurement and validation. A. Flow speed profile within the three cell channels along the flow path computed by COMSOL Multi-physics. The average speed through the cell channel is approximately $2.0 \mu\text{m/s}$. B. Measured flow speed at three spatial locations that are 1 mm apart (see position a, b, and c as marked in Figure 7A using a fluorescence recovery after photobleaching (FRAP) method. C. Measured flow speed in the cell channels is validated against the calculated speed using the known pumping flow rate and channel geometry. The red dots are experimental data, and the solid line ($y = 41.7x$) is the calculated flow speed.

COMSOL Multiphysics program was used to compute the flow field within the collagen matrix. To set up the computation model, the device geometry with the central region of the three cell channels (the region of interest where IF will run through) and part of the flow channel (shown

in Figure 2.4A) was used for the simulation. The right side of the flow channel is set as inlet the left side of the flow channel is set as the outlet. No-slip boundary condition was applied.

In the flow channel regions (no collagen), Navier-Stokes equation (Equation 1) was applied to generate the flow field.

$$\rho \left(\frac{\delta u}{\delta t} + \vec{u} \cdot \nabla \vec{u} \right) = -\nabla P + \mu \nabla^2 u \quad (1)$$

In the collagen region, Brinkman Equation (Equation 2) for a porous medium was applied to generate the flow field.

$$\mu \nabla^2 \vec{u} - \frac{\mu}{k} \vec{u} = -\vec{\nabla} P \quad (2)$$

Where ρ is the fluid density, u is the flow velocity, P is pressure, μ is the fluid dynamic viscosity, and k is the permeability of the porous medium. In the computation, we used $\rho = 997 \text{ kg/m}^3$ as the density of water, $\mu = 0.000692 \text{ Pa} \cdot \text{s}$ as the dynamic viscosity of water at 37°C , average inlet velocity of $u = 1.5 \text{ } \mu\text{m/s}$, outlet pressure $P_{\text{out}} = 0 \text{ Pa}$, and $k = 10^{-11} \text{ m}^2$ as the permeability of Type I collagen matrix at 1.5mg/mL [141].

CHAPTER 3

Interstitial flows promote an amoeboid over mesenchymal motility of breast cancer cells

3.1 Introduction

IFs are ubiquitous in human tissues. They are driven by the hydrostatic and osmotic pressure differences among the arterial, venous, and lymphatic vessels [177]. In healthy tissue, IF rates are on the order of a few micrometers per second [178]. Within malignant tumor, IF rates can reach as high as 10 $\mu\text{m/s}$ in animal models [64, 178, 179], and up to 55 $\mu\text{m/s}$ in human cancer patients [179, 180]. A number of dynamically evolving TME factors have been identified to contribute to the elevated interstitial fluid flows, including the continual expansion of tumor mass which builds up the interstitial fluid pressure within the tumor [181, 182], the subsequent abnormal growth of vascular vessels via angiogenesis [183, 184] and/or lymphangiogenesis [52, 185, 186], as well as the denser ECM deposited and remodeled by stromal cells with higher hydraulic conductivity [187, 188]. Clinically, lymph nodes are known to be the first metastatic sites for many cancer types, including breast [189] and prostate cancers [190]. Recognizing that IFs drain towards lymph nodes, an emerging question is: whether and how IFs guide and modulate tumor cell invasion into the lymph nodes [70]. Indeed, pioneer work from the Swartz lab has demonstrated that IFs (0.2 and 0.7 $\mu\text{m/s}$) can spatially redistribute chemokine secretions of breast and glioma tumor cells, and direct tumor cells invasion along the flow direction in a chemokine receptor CCR7/CXCR4 dependent manner using a modified Boyden Chamber model [70, 72].

Tumor cells are known to be heterogeneous (ensemble variability) and plastic (temporal variability) in response to the complex TME [171]. In cancer metastasis, only a subpopulation of the tumor cells or rare cells break away from the primary tumor and migrate through the interstitial

space, with only a fraction of those eventually establishing a secondary tumor at an ectopic site. Cancer cell heterogeneity and plasticity are also demonstrated through their diverse motility types. Single animal cell migration within a 3D architecture can be broadly categorized into amoeboid and mesenchymal motility phenotypes [85, 191]. In amoeboid motility, cells appear rounded in shape, form actin protrusions and dynamically change their shapes to squeeze through pores within the collagen fiber network [192-194]. Traction is distributed all around the cell surface through many short-lived adhesive contacts with the ECM [195, 196]. In mesenchymal motility, cells appear elongated in shape, climb along the collagen fibers, and proceed by either remodeling or degrading the matrix in an integrin and/or proteolysis dependent manner [197, 198]. Traction is exerted through long-lived, polarized and highly localized focal adhesion complexes [146, 199, 200]. While leukocytes typically exhibit amoeboid motility, and fibroblasts assume mesenchymal motility, cancer cells are known to be able to switch between these two motility types depending on the microenvironment [201, 202]. Wolf *et al.* discovered that fibrosarcoma cells switch from a mesenchymal to amoeboid motility when matrix metalloproteinase (MMPs) was inhibited in both 3D *in vitro* model and mouse model [201].

For understanding the heterogeneity and plasticity of tumor cell, there is a need for tools that can interrogate cancer cell invasion at single-cell or subpopulation level, and in real time. Current microfluidic models have revealed that flow-guided cell migration depended on a number of critical parameters within the TME, including chemokine receptors, matrix stiffness, cell density, and flow rates [134, 135, 203]. In a recent work, Polacheck *et al.* showed that breast tumor cells (MDA-MB-231) can migrate either along or against the IF direction depending on cell density and CCR-7 receptors [134]. Haessler *et al.* demonstrated that IFs modulate migration characteristics of a subpopulation of the MDA-MB-231 cells, highlighting the heterogenetic response of tumor

cells under the influence of IFs [135]. In this article, we focus on the impact of IFs on cell morphology and motility phenotypes.

In our early work on breast cancer cell chemotaxis using a 3D microfluidic device with a gradient generator, we found that MDA-MB-231 cells switched between amoeboid and mesenchymal motility depending on whether or not the system was perfused [110]. Inspired by this finding, we carried out a systematic study on the roles of IFs on the morphology and motility of MDA-MB-231 cells using a 3D microfluidic model. In this article, we show that MDA-MB-231 cells embedded in a 3D collagen matrix are more rounded and execute mostly an amoeboid motility in the presence of IFs; while they are more elongated and execute mostly mesenchymal motility in the absence of the flow. The addition of the exogenous adhesion molecule, fibronectin (FN), partially rescues a mesenchymal cell phenotype in the presence of the flow. Our work reveals that IFs modulate cancer cell morphology and motility phenotypes, emphasizing roles of fluid flows in regulating cancer cell migration heterogeneity.

3.2 Materials & Methods

3.2.1 3D cell culture preparation

MDA-MB-231, a malignant breast tumor cell line, was provided by the Cornell Center of Microenvironment and Metastasis. DMEM medium (Invitrogen, Carlsbad, CA), supplemented with 10% FBS (Atlanta Biologicals, Lawrenceville, GA) and 1% antibiotics (Invitrogen, 100 units penicillin and 100 µg streptomycin) was used. Cells were cultured in a humidified incubator with 5% CO₂ and 37°C environment and harvested at 50%-70% confluence for each experiment.

Type I collagen was extracted from rat tails (Pel-Freez, Rogers, AR) using a modified protocol [141] and stored at a concentration of 5 mg/mL in 0.1% acetic acid at 4°C . A volume of 60 μ L collagen stock was titrated with 1.32 μ L 1N NaOH and 20 μ L 10X M199 to yield a final pH of approximately 7.4 and then mixed with cell culture solution to a final volume of 200 μ L. The final collagen concentration was 1.5 mg/mL. For some experiments, soluble form of fibronectin (human plasma, EMD Millipore, Calbiochem, Billerica, MA) was supplemented into the cell-collagen solution with a stock concentration of 100 μ g/mL and yield to a final concentration of 20 μ g/mL in the microfluidic device. This concentration was chosen to provide optimized cell motility [198]. For all the experiments reported below, a cell concentration of 10^6 cells/mL was used.

3.2.2 Experimental procedures

First, cell-embedded collagen solution was introduced to fill two or three cell channels in each device (See Figure 8B,C) on an ice pack. The assembled microfluidic chips were then placed in a humidity controll incubator (37 °C, 5% CO₂) to allow collagen polymerization for 45 minutes. To prevent cells from gravitationally settling down to the bottom of the device, the microfluidic chips were positioned up-side-down for the first 11 minutes and then flipped over for 34 more minutes in the incubator. Second, 37 °C medium was introduced into the empty flow channels until the outlet reservoirs were full, both the inlets and outlets of the flow channel were then plugged with PDMS filled gel loading tips. Third, the microfluidic chip was transferred to the microscope stage enclosed by a humidity control chamber, which is kept at 37 °C with and 5% CO₂. The chip was typically left on the stage for an hour for reaching thermal equilibrium before imaging. Finally, IFs were pumped through the flow channel and the cell channels were imaged. We defined $t = 0$ as the time when the flows and imaging were started, which typically was three hours after the cell seeding. In each experiment, one device was used as control (no flow) and the

other two were connected to a syringe pump to introduce IFs of $0.05\mu\text{L}/\text{min}$ ($2.0\ \mu\text{m}/\text{s}$). This speed was chosen to represent the high end of IFs in healthy tissue.

3.2.3 Microfluidic device experimental setup

IFs were generated within a 3D collagen matrix using a microfluidic device developed previously in our lab (Ref. [172]). Briefly, three identical devices were patterned in a 3 mm thick PDMS membrane, which was subsequently sandwiched between a glass slide and a Plexiglas manifold (Fig. 3.1A). In a typical experiment, collagen was first introduced into three parallel cell channels. After the collagen was polymerized, medium was introduced through the flow channel that is perpendicular to the cell channels via a syringe pump (Fig. 3.1B). The key feature of the device was that it used a contact line pinning technique to confine collagen matrix within the wall-less cell channels (Fig. 3.1C), such that IFs could run through the collagen matrix without obstructions and were spatially uniform.

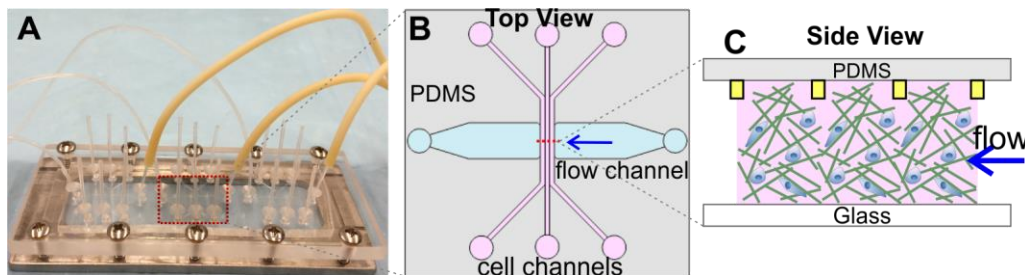


Figure 3.1. Microfluidic device setup for single cell experiment. (A) Illustration of the microfluidic setup: three identical devices were patterned on a 3 mm thick PDMS membrane and sandwiched between a Plexiglas manifold and a $1'' \times 3''$ glass slide. (B) Within each device, cell embedded collagen is seeded in the three parallel cell channels, each with a cross section of $400\ \mu\text{m} \times 200\ \mu\text{m}$. Fluid flows are introduced in the horizontal flow channel with a cross section of $3\ \text{mm} \times 200\ \mu\text{m}$. (C) Collagen is confined within the three cell channels by the contact lines, marked by the yellow rectangles (not to scale), each with a cross section area of $10\ \mu\text{m} \times 5\ \mu\text{m}$.

3.2.4 Staining for actin filaments

Actin filaments were stained using Actin Cytoskeleton and Focal Adhesion Staining Kit (EMD Millipore). MDA-MB-231 cells were first seeded in 1.5 mg/mL collagen matrix placed in 96-well plate and incubated in a humidified condition with 5% CO₂ at 37°C for at least 5 hours to allow cells to spread and attach to the collagen matrix. Cells were fixed with 4% paraformaldehyde for 15 minutes at room temperature and washed twice with 1X wash buffer (1X PBS with 0.05% Tween-20). Cells were then permeated with 0.1% Triton X-100 for 5 minutes and washed twice, followed by applying the blocking solution (1X PBS with 1% BSA) for 40 minutes. TRITC-conjugated phalloidin with 1:100 dilution was applied to the cell culture for 60 minutes at room temperature. The samples were then imaged using a Zeiss LSM 710 confocal microscope after being washed three times.

3.2.5 Imaging and data analysis

An inverted microscope (IX81, Olympus America, Center Valley, PA, USA) with a CCD camera (Orca-ER, Hamamatsu Photonics, Japan) was used for all the experiments. In cell experiments, images at three or more positions of the cell channel were taken using 10X objective (Olympus, NA=0.3) in bright field mode. All the images were taken in the mid-z plane of the channel. Here z refers to the vertical direction. A sequence of 192 images was captured every 5 minutes for a total of 16 hours. $t = 0$ is defined as the time when the first image was taken, at which the flow was applied.

To quantify cell morphology, the cell shape was fitted to an ellipse outline using a ROI manager tool from ImageJ. The aspect ratio of each cell is defined as the ratio of the major to the minor axis of the ellipse. Cells with aspect ratio smaller than 2.0 were considered as amoeboid cells and otherwise were considered as mesenchymal cells to be consistent with previous work [204].

To quantify cell motility, cell migration trajectories were first tracked using manual tracking in ImageJ. The cell speed (total distance traveled divided by 16 hours of imaging time), x -velocity (displacement along the flow direction divided by 16 hours), persistence (displacement divided by the entire length of the track), x -persistence (displacement in the flow direction divided by the entire length of the track), and mean square displacements (MSDs) were computed using an in house MATLAB program. The x -velocity and x -persistence were converted in all experiments, with positive values indicating motion against the flow and negative values indicating motion along with the flow. To minimize the variations from experiment to experiment, speed was normalized by the average speed of the control group (no flow) and the normalized x -velocity was the average velocity along flow direction subtracted by that of the control group, and divided by the average speed of the control group. We note that although cells embedded within a 3D collagen matrix, and images were taken in the mid-plane along the vertical direction of the cell channel, almost all the tracked cells remained in the field of view during the 16 hour imaging time. Thus, only 2D trajectories were obtained and presented. Cells migrate faster than a threshold speed of 0.2 $\mu\text{m}/\text{min}$ were considered to be motile cells. 60 motile cells were randomly selected from each condition for computing all the motility parameters. Student t-test was performed for two-group analysis using Prism GraphPad. All experiments were repeated three to four times independently.

3.3 Results and Discussion

3.3.1 IFs promote an amoeboid cell morphology and motility

A distinct effect of IFs on MDA-MB-231 cells is that it promotes an amoeboid over mesenchymal cell motility phenotype (Fig. 3.2). Initially, almost all the cells were round or in an

amoeboid shape at the moment they were mixed with the un-polymerized collagen. In the absence of flow, most cells appeared to be round at $t = 0$. As time evolved, cells stretched, adhered to the collagen fibers, became elongated, and executed a mesenchymal motility phenotype (Fig. 3.2A top panel). We observed that about 30% of the MDA-MB-231 cells dynamically evolved from amoeboid to mesenchymal motility within a time duration of 16 hours. In the presence of flow, most cells remained round and executed an amoeboid motility phenotype (Fig. 3.2A bottom panel). The distribution of the cell aspect ratio was found to have a distinct shift towards smaller aspect ratio values for the case with the flow in comparison to the case with no flow at $t = 16$ hr (Fig. 3.2B). At all time points between $t = 0$ and 16 hr, we found that cells in the absence of flow had a larger percentage of mesenchymal cells than those with flow (Fig. 3.2C). For example, the percentage of mesenchymal cells at $t = 16$ hr was $58 \pm 4\%$ with no flow, in contrast to $27 \pm 4\%$ with a flow of $2 \mu\text{m}/\text{s}$. It should be noted that the initial fraction of about 25% of the mesenchymal cells were a result of the 3 hours time difference between the time of cell seeding and the time of imaging.

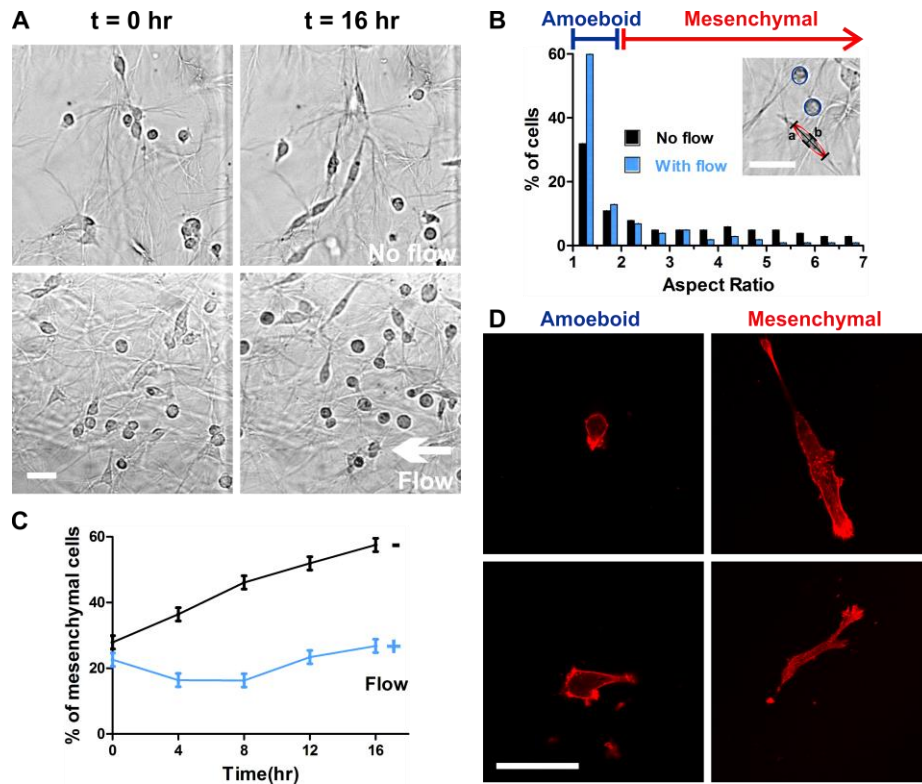


Figure 3.2: IFs promote an amoeboid cell morphology and motility. (A) Micrographs of MDA-MB-231 cells embedded in a collagen matrix at two time points ($t = 0$ and $t = 16$ hr) in the absence (top row) and presence (bottom row) of the flow. The flow speed is $2 \mu\text{m/s}$ (or a flow rate of $0.05 \mu\text{L/min}$). (B) The distribution of the aspect ratio of MDA-MB-231 cells in the absence (black) and presence (blue) of the flow at $t = 16$ hr. Cells with aspect ratio (a/b) less than 2.0 are defined as amoeboid cells, and cells with aspect ratio greater than 2.0 are defined as mesenchymal cells. (C) Percentage of mesenchymal cells versus time in the absence and presence of flow. 600 cells from three independent experiments are used towards the computation of each data point. (D) Micrographs of amoeboid and mesenchymal cells taken at one z-plane. The red color shows actin staining. All scale bars are $50 \mu\text{m}$.

Cell aspect ratio (long axis divided by short axis of the cell shape, see insert of Fig. 3.2B) was used for quantifying cell morphology. Cells with aspect ratio less than 2.0 were defined as amoeboid cells, and larger than 2.0 as mesenchymal cells. This definition was derived from our own observations and is consistent with previous literature [201, 204, 205]. In our own experiments, round or amoeboid cells extended their protrusions in all directions, formed short lived adhesion to the fibers, and squeezed through the collagen matrix when finding a suitable path

(Fig. 3.3A). The elongated or mesenchymal cells, on the other hand, were highly polarized. They formed long-lived adhesions and climbed along the fibers (Fig. 3.3 B). A summary of the cellular and molecular differences between amoeboid and mesenchymal cells is shown in Fig. 3.3 C. Additionally, we visualized spatial distribution of actin filaments within cells of these two types using actin staining. Clearly, the round cells displayed an amoeboid phenotype where the actin filaments were mostly distributed around the cell peripherals and the elongated cells demonstrated a mesenchymal phenotype where the actin filaments formed a highly polarized bundle (Fig. 3.2 D). In the previous literature, aspect ratio of 2.0 was used as a threshold for the definition of amoeboid (round) versus mesenchymal (elongated) cells migrating within a 3D matrix for a variety of cell types, including, breast tumor cells (MDA-MB-231) [201], melanoma cells (A375M2) [205], and fibrosarcoma cells (HT-1080) [204]. This definition was based on the observations of cell motility types, proteolytic activities and the co-cluster of integrins [201], GTPase Rac or Rho-kinase signaling activities [205], and localization of actin or focal adhesion molecule paxillin [204]. For the remaining of the paper, we will refer to round cells (or cells with aspect ratio less than 2.0) as amoeboid cells, and elongated cells (or cells with aspect ratio larger than 2.0) as mesenchymal cells.

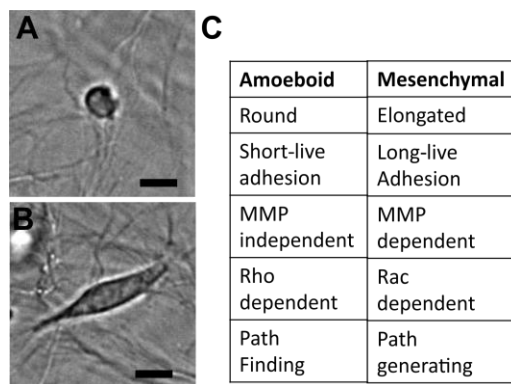


Figure 3.3. Amoeboid versus mesenchymal motility. Micrograph of an amoeboid (A) and mesenchymal (B) MDA-MB-231 cell embedded in 3D collagen matrix. (C) A table summarizes differential aspects of amoeboid and mesenchymal cells. All scale bars are 20 μm .

Mesenchymal to amoeboid transitions have been reported in cancer cell invasion in previous literature in response to the changes in their 3D microenvironments [201, 206, 207]. Wolf *et al.* discovered that blocking pericellular proteolysis of HT-1080 fibrosarcoma cells and MDA-MB-231 carcinoma cells embedded in collagen encouraged mesenchymal to amoeboid transition [201]. Yamazaki *et al.* showed that Rac signaling was correlated with elongated cell morphology, and inhibiting Rac1 led to a mesenchymal to amoeboid transition of HT1080 cells in 3D collagen matrix [207]. Sahai *et al.* demonstrated that Rho was correlated with round cell morphology, and inhibiting Rho signaling of the A375m2 cells in a 3D environment, in contrast, promoted elongated mesenchymal phenotype [208]. Kumar's group reported a mesenchymal to amoeboid transition by modulating the matrix stiffness of the ECM. More specifically, they found that U373-MG human glioma cells changed from a mesenchymal to an amoeboid morphology when the collagen matrix was stiffened by the addition of the agarose gel [206]. Here, our experimental results revealed that IFs promoted an amoeboid phenotype of MDA-MB-231 cells. It remains to be explored whether other cell lines also undergo motility phenotype transitions under the influences of IFs.

In contrast to the amoeboid cell migration, mesenchymal cells require integrin-based adhesion to migrate. It is known that mesenchymal cells form long-lived adhesions with the ECM fiber bundles, which trigger the downstream signaling that activates actin remodeling and thus cell migration [209]. We hypothesized that IFs modulate cell motility through adhesion. Fibronectin (FN) is an important adhesion molecule in mediating mammalian cell migration [210]. In the absence of flow, cell secreted FNs assemble into fibrillar form, and bound with collagen, which promote a mesenchymal cell phenotype. In the case of flow, the interstitial-flow-induced amoeboid cell motility was likely caused by the lack of assembled endogenous adhesion molecules such as FN. More specifically, the flows carried away the cell-secreted adhesion molecules before they

were assembled into fibrils and anchored to the collagen fibers. To test this hypothesis, we carried out experiments to investigate the roles of exogenous FN on cell morphology and motility in the absence/presence of the flows.

3.3.2 Exogenous FN promotes a mesenchymal cell phenotype

To study the cooperative roles of IFs and adhesion molecules on breast tumor cell motility phenotype, we investigated cell aspect ratio under four different flow and FN conditions. Overall, cells were more elongated in the presence of FN than those without (Fig. 3.4A). Cell aspect ratio distribution shifted distinctively towards larger aspect ratio values in the presence of FN (Fig. 3.4B) in the case of no flow. Furthermore, the percentage of mesenchymal cells was significantly higher with FN than no FN at all time points (Fig. 3.4C). For example, the percentage of mesenchymal cells at $t = 16$ hr was $76 \pm 4\%$ with FN, in contrast to $58 \pm 4\%$ with no FN. In the presence of the flow, this shift towards mesenchymal phenotype due to the presence of FN was mild, and was less evident than the case with no flow (Fig. 3.4C). The percentage of mesenchymal cells at $t = 16$ hr was $32 \pm 4\%$ with FN, similar to $27 \pm 4\%$ with no FN.

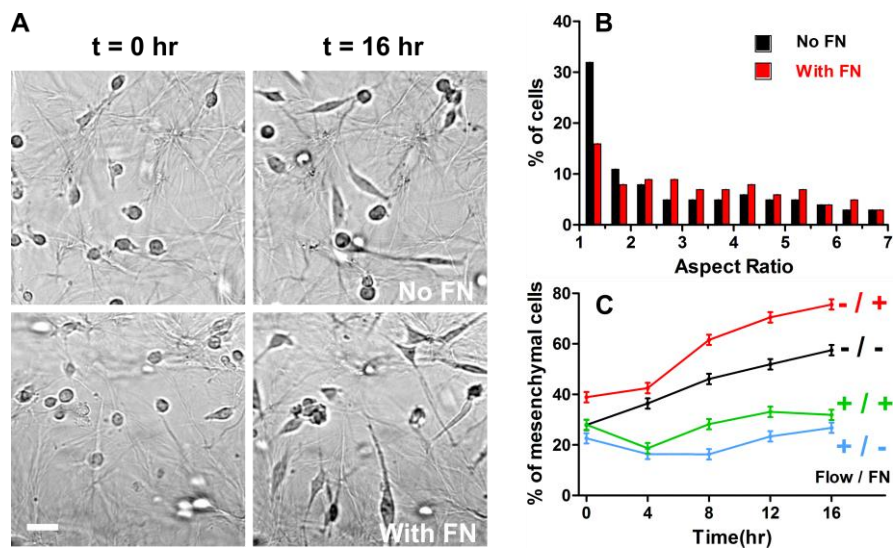


Figure 3.4: Exogenous FN promote a mesenchymal cell phenotype. (A) Micrographs of MDA-MB-231 cells embedded in a collagen matrix at two time points ($t = 0$ hr and $t = 16$ hr) in the absence (top row) and presence (bottom row) of FN. The FN concentration is $20 \mu\text{g/mL}$. There is no flow in all four cases. Scale bar is $50\mu\text{m}$. (B) Histograms of the aspect ratio in the absence (black) and presence (red) of FN at $t = 16$ hr with no flow. (C) Percentage of mesenchymal cells versus time for four flow and FN conditions. Number of cells tracked in each group is 600 cells from three independent experiments.

The presence of exogenous FN provides cell adhesion sites to cells, encourages actin filament polarization and thus promotes a mesenchymal cell phenotype. The observed shift towards mesenchymal cell phenotype due to FN was more evident in the absence of the flow than with the flow possibly due to the fact that flows carried away the exogenous FN with time. The results here indicate that the MDA-MB-231 cell motility type switch depends on the availability of the adhesion molecules, which can be modulated through the IFs. We note that FN is added to the cell-embedded collagen prior to the introduction of the flow. An alternative explanation of this phenomena is that the shear flow activates membrane surface receptor $\beta 1$ -integrin [138], which renders the receptors less sensitive to FN in the presence of flow. Thus, flow reduced the cell surface integrins binding to the ECM and exhibit amoeboid phenotype [211, 212]. Future experiments using in-soluble form of fibronectin will help elucidating the exact roles that FN play in cell motility phenotypes switch in the presence of flow.

3.3.3 IFs mildly enhance cell speed but no significant directional cell migration is observed

Cell motility was examined via the tracking of each individual cell, which was subsequently used to compute cell migration parameters, including cell speed and velocity along the flow, as shown in Figure 3.5. Figure 3.5A shows the cell migration trajectories under four combinations of flow and FN experimental conditions.

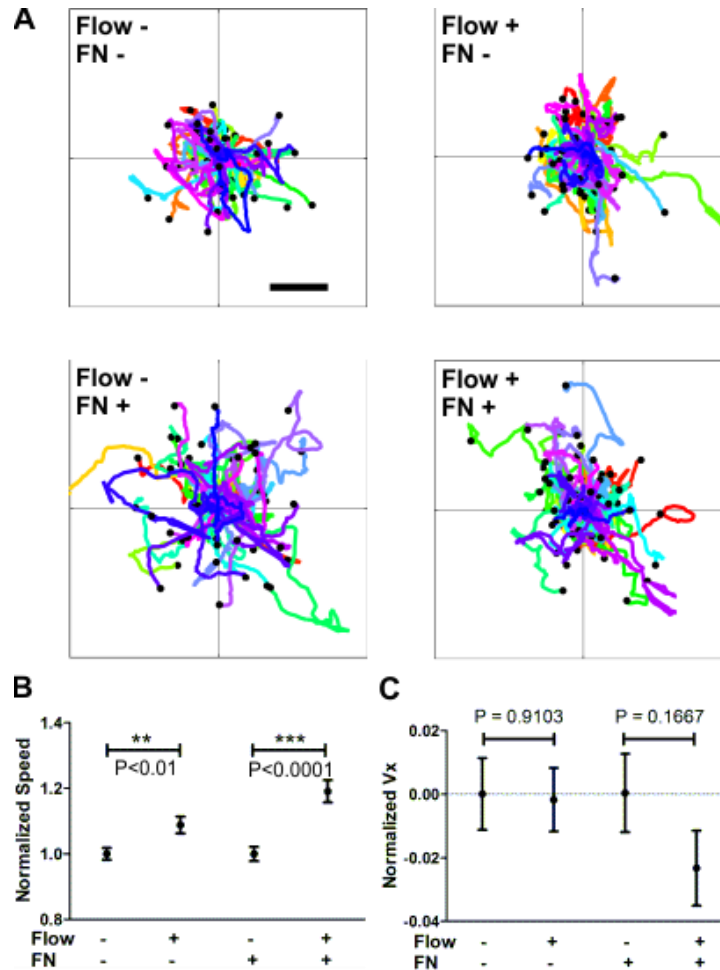


Figure 3.5: IFs slightly enhance cell speed but no significant directional migration is observed. (A) Cell trajectories under various flow and FN conditions. Each plot has 60 cell trajectories, and each colored line represents one cell trajectory of 16 hours long. Flow is from left to right in this data set. Scale bar is 100 μ m. Normalized speed (B) and normalized velocity along flow direction V_x (C) along the direction of the flow for four conditions. 180 cells combined from three experiments in each condition are used here.

Using normalized cell speed, we observed that IFs enhanced cell migration speed mildly, with approximate $10 \pm 7.5\%$ and $20 \pm 7.5\%$ increase for the case of no FN and FN respectively (Fig. 3.5B). The normalized cell velocity did not show a significant deviation from zero in any of the four flow and FN experimental conditions (Fig. 3.5C), indicating no significant directed cell migration in parallel to the flow was observed at the population level. A detailed comparison of

our results on MDA-MB-231 cell motility along with the experimental conditions from three different labs was included in the supplementary information section (Table S1) [134, 135].

3.3.4 *The fastest migrating cells are within the subpopulation of amoeboid cells*

We observed that MDA-MB-231 cells dynamically changed their cell shape during the observation period. To investigate the relationship between cell aspect ratio and cell speed, we computed the hourly average speed of each individual cell together with its cell aspect ratio. Fig. 3.6A-D shows the scatter plots of hourly cell speed versus the corresponding aspect ratio under four different experimental conditions. Interestingly, we saw a common feature from all four plots in that the maximum speed of a sub-population (within a narrow range of aspect ratio) is inversely proportional to its aspect ratio as indicated by the red dashes lines in Fig. 3.6. By closely examining the spread of the scatter plots along x -axis in Fig. 3.6A-D, we also found that the cell aspect ratio distribution spanned in a wider range (or more heterogeneous) in the absence of flow than with the flow. In the presence of the flow, more cells had smaller aspect ratios (or assume an amoeboid motility type), which was consistent with the computed average values shown in Figure 3.2C. It is interesting to note that our discovery, that the fastest migrating cells are within the amoeboid cell phenotype, is consistent with intravital imaging where the fast migrating cells *in vivo* are also seen to be amoeboid cells [85, 192].

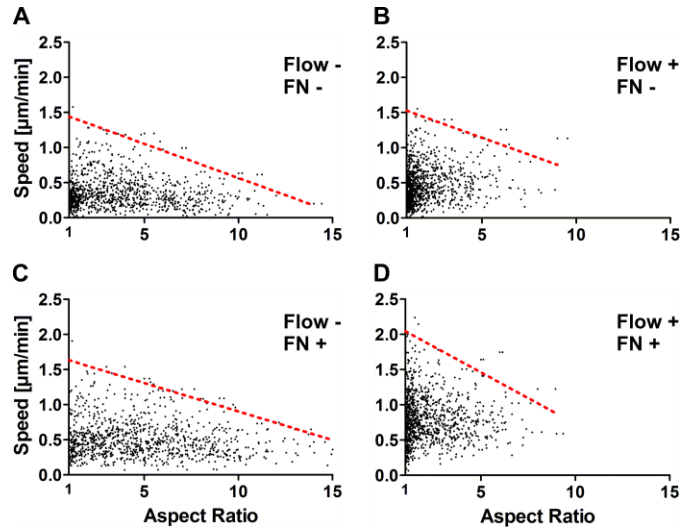


Figure 3.6: Maximum cell speed is inversely correlated to the aspect ratio of cells. (A-D) MDA-MD-231 cell speed versus aspect ratio under four flow and FN conditions. Each dot represents an hourly average speed at a defined aspect ratio. Number of dots for each experiment is 960. Dashed lines are linear fits to the measured maximum speed at a narrow range of aspect ratio (A.R. range = 1) versus cell aspect ratio.

3.3.5 IFs impair the mean square displacements and the persistence of the cell tracks

An important characteristic for cancer cell invasion within a 3D ECM is its ability to spread to a distant location. Towards this end, we computed the mean square displacements (MSDs) using the cell trajectories as shown in Figure 3.5A for all four experimental conditions. We found that the MSDs were lower in the presence of flow compared to the case with no flow over the observation period (Fig. 3.7A), indicating IFs impaired the average displacement of the whole cell population, and thus the ability to spread. This was also observed in the two cases with FN. We also computed the diffusion coefficient of the cells using the first order diffusion equation in the four conditions, and found that the coefficients are $2.67 \mu\text{m}^2/\text{min}$ and $1.71 \mu\text{m}^2/\text{min}$ for control and flow in the absence of FN. We obtained the coefficients of $4.5 \mu\text{m}^2/\text{min}$ and $3.62 \mu\text{m}^2/\text{min}$ for control and flow in the presence of FN. These data indicated that IFs decreased the tumor cell's ability to invade. In addition, all the MSD profiles display an exponent (measured from a fit of MSDs $\sim t^\alpha$)

greater than 1 (Fig. 3.7B), indicating that cell displacements in 3D did not follow a Gaussian distribution, and can be described by a super diffusive model [213]. Our observation on MDA-MB-231 cell motility was consistent with previous work on the non-Gaussian random motility of HT1080 cells in a 3D type I collagen matrix [213]. The lower exponent for the case with flow, $\alpha = 1.27 \pm 0.013$, in contrast to $\alpha = 1.46 \pm 0.013$ for the case of no flow, also shows that cell migration is closer to a random walk (e. g. $\alpha = 1$) in the presence of flow. Again, flow impairs the cells ability to spread. We note that this observation was derived from combining all three sets of experimental results.

To understand the impaired MSDs in the presence of the flow, we computed persistence of the cells in the presence and absence of the flow. Fig. 14C shows that IFs impaired the average cell migration persistence, from 0.26 ± 0.02 with no flow to 0.16 ± 0.01 with flow, for the case of no FN. The two groups with FN also exhibited the same trend, from 0.20 ± 0.02 with no flow to 0.14 ± 0.01 with flow (Fig. 3.7C).

This decrease in persistence in the presence of flow was consistent with our observation that IFs promote amoeboid motility. Amoeboid cell motility is less persistent than that of mesenchymal cells because amoeboid cells migrate via squeezing through the pore structure of the collagen fiber in a path-finding fashion while mesenchymal cells migrate via climbing along collagen fibers in a path-generating fashion [79]. Mesenchymal cells exhibited larger average persistence than amoeboid cells, with 0.21 ± 0.02 compared to 0.13 ± 0.02 (Fig. 3.7D).

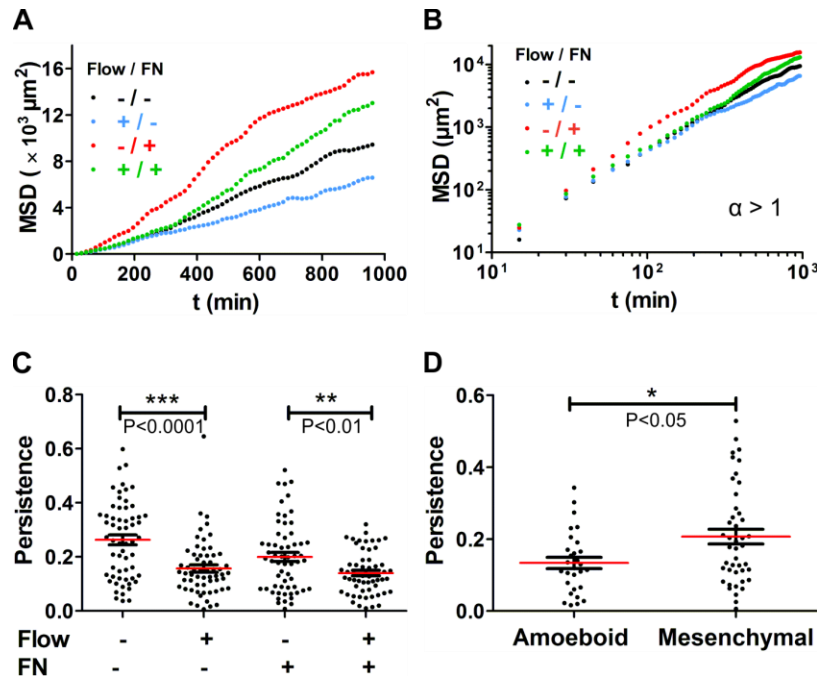


Figure 3.7: IFs impair MDA-MB-231 mean square displacements and persistence. (A) Linear scale plot and (B) logarithmic scale plot of the mean square displacements (MSDs) for four flow and FN conditions over 16 hours. The exponent, α , is measured from a fit of MSDs $\sim t^\alpha$ and are equal to 1.46 ± 0.013 , 1.27 ± 0.013 , 1.45 ± 0.025 , and 1.48 ± 0.007 for four conditions. 180 cells combined from three experiments in each condition are used. (C) Scatter plots of cell migration persistence for four flow and FN conditions in a typical experiment. 60 cells are used for each condition. (D) Scatter plots of cell migration persistence for amoeboid versus mesenchymal cells in one experiment. Approximately 35 amoeboid or mesenchymal cells are used for analysis.

In order to metastasize, cancer cells need to break away from the primary tumor and migrate through interstitial space before entering vascular vessels. It is important to understand how environmental cues influence cancer cells' ability to disseminate. Here, we propose to use MSD, the average distance squared of all the cells within a population to characterize cell dissemination. This is important, because cell speed or cell persistence alone is not sufficient to describe cell spreading [214]. Through MSD measurements, we observed that although IFs enhanced average cell speed, they nonetheless reduced the cancer cells' probability of migrating persistently. The combined outcome, characterized by MSD, is the impaired ability to spread to a distant site in the presence of flow.

As different microfluidic and modified Boyden chamber models emerge for studying roles of IFs on cancer cell invasion, we note that cell migration characteristics sensitively depend on experimental conditions. In our work, we did not observe the flow-guided cell migration that had been observed in a microfluidic model by Polacheckl *et al.*[134] and in a modified Boyden chamber [70]. One critical factor could be the different stiffness of the ECM or substrata in which cells were embedded. In Polacheck *et al.*, cells were embedded in type I collagen matrix with a pH of 8.9, and higher pH condition have been shown to increase the mechanical properties such as the stiffness of the ECM (also with smaller pore sizes) [143]. In Shields *et al.*, cell-embedded matrix was placed on a cell culture insert within the Boyden chamber. The cell culture insert was made of a porous polycarbonate with a stiffness on the order of GPa. In these two cases, IFs coupled with the stiffer matrix or substrata may promote rheotaxis along the flow direction. In our experiment, cells were embedded in a 1.5mg/mL collagen matrix, with a Young's modulus close to 50Pa [215, 216]. We find this apparent impact of matrix stiffness on motility particularly interesting because this is consistent with the recent reports on the effects of the altered tumor mechanical microenvironment. Specifically, it has been observed that stiffer stroma contributed from the cell-aligned collagen fibers[217] and high density of crosslinking fibers [218] promote tumor cell invasion [219].

3.4 Conclusion and future perspectives

TME is complex and evolves constantly in space and time. It is thus critical to develop *in vitro* models that can recapitulate this spatially and temporally changing landscape. Using a microfluidic model, we reveal that IFs promote an amoeboid cell motility phenotype, and the fast moving cells belong to the subpopulation of amoeboid cells. Using cell shape analysis, we find that maximum cell speed within a specific cell aspect ratio range is inversely related to cell aspect

ratio. Using cell migration trajectory analysis, we find that IFs impair the cell ability to migrate persistently and subsequently their ability to spread. These results raise a number of important questions at molecular level with respect to how IFs influence cell migration. For example, how IFs impact the GTPase RhoA and Rac1 signaling activities, which are known to directly correlate with amoeboid and mesenchymal cell motility.

Cell adhesions to the ECM via integrins are central to cell migration within a 3D architecture. There is still much to explore before we fully understand how cell adhesion is coupled with fluid flow to alter cell migration. The work presented here demonstrates that exogenous FN partially rescues a mesenchymal phenotype in the presence of the flow. This result indicates that fluid flow may influence cell migration through carrying away adhesion molecules or through direct shear activated integrins [203]. The next level of inquiry requires the development on utilization of biosensors [220, 221] that are compatible with dynamic imaging in microfluidic device to allow for direct monitoring of molecular activities and at the same time cell migration behavior.

3.5 Supplementary information

3.5.1 Summaries of role of IFs on breast tumor cell invasion experiments using microfluidics from three labs.

Table S1: Summaries of the experimental settings and results from three labs on the roles of IFs on cell motility using microfluidic models.

		Polacheck <i>et. al.</i> (2011) PNAS	Haessler <i>et. al.</i> (2012) Integrative Biology	Huang <i>et. al.</i> This manuscript
Flow experiment set up	Cell Line	MDA-MB-231	MDA-MB-231	MDA-MB-231
	Cell Density	High: 2.5×10^5 cells/mL Low: 0.5×10^5 cells/mL	2.5×10^5 cells/mL	1.0×10^6 cells/mL
	Flow Speed	0.3 and 3.0 $\mu\text{m/s}$	10 $\mu\text{m/s}$	2.0 $\mu\text{m/s}$
	Flow Generation	40 Pa Pressure head	Peristaltic pump	Syringe pump
	3D ECM	2.0 mg/mL type I collagen (PH=8.9)	1.5 mg/mL type I collagen with 10% matrigel (PH=7.4, private communication)	1.5 mg/mL type I collagen (PH=7.4)
	Pre-incubation	overnight incubation	overnight incubation	no pre-incubation
	Medium supplement	10 ng/mL EGF	no additional supplement	no additional supplement
	Imaging	15min interval for 16-24 hr	15min interval for 16 hr	5min interval for 16 hr
Results and interstitial flows effect	Average cell speed in static condition	0.1 $\mu\text{m/min}$	0.17 $\mu\text{m/min}$	0.36 $\mu\text{m/min}$
	Motile cell speed gate	one cell diameter in 8hr	0.02 $\mu\text{m/min}$	0.2 $\mu\text{m/min}$
	Motility of entire cell population	No significant effect	flow increases population of motile cells	-
	Average cell speed/velocity	no significant effect on average velocity	flow increases average speed, also reflected on a histogram plot	flow enhances the normalized average speed
	Persistence or directionality	flow increases directionality from 0.39 to 0.63	no significant effect on overall average persistence (~0.45)	flow decreases persistence (~0.2)
	Average x -velocity	cells prefer to migrate along the streamline	no significant effect on overall average x -velocity	no significant effect
	Directed velocity/directional migration (within 45° of x -axis)	<u>high cell density</u> : cells migrate against the flow; <u>low cell density</u> : cells migrate along with the flow	flows increase the percentage of cells migrate along with the flow direction	no significant effect on directional migration was observed
	Directed persistence (P_x)	-	no significant effect on overall average P_x ; flow increases the percentage of cells (5-10%) with P_x both along and against the flow direction	no significant effect on overall average P_x and directed P_x in the flow direction was observed
Morphology	-	-	flow enhances amoeboid phenotype	

CHAPTER 4

Interstitial flows modulate breast tumor spheroid invasion

4.1 Introduction

The human body is composed mostly of fluids (~60 % the body mass), and approximately one third of the body fluids are in constant movement through the blood circulation as well as the interstitial extracellular tissue [222]. The movement of the fluid within the interstitial space, or interstitial flows (IFs), is driven by the hydrostatic and osmotic pressure differences among the blood, vein and lymphatic vessels [139]. IFs are critical for maintaining healthy tissue homeostasis, and are known to provide necessary nutrients, essential chemicals to the cells and at the same time remove metabolic wastes from the cells [222]. In healthy tissue, the measured flow rate of IF is typically low, on the order of a few micrometers per second in animal models [178]. In the TME, IFs are often elevated due to high interstitial fluid pressure within the tumor as a result of abnormal angiogenesis, and can increase at least five-fold in magnitude [65, 179]. Although the importance of the TME in tumor progression has been emphasized in recent literature, the biophysical cues within the environment, with the exception of matrix stiffness and architecture, in tumor invasion have not been explored extensively.

We now know that IFs can impact tumor invasion via redistribution of the chemical signaling molecules within the TME and/or direct application of shear stresses onto the cells [223-226]. Using a modified 3D Boyden Chamber assay, pioneering work from the Swartz lab showed that IFs can skew the tumor secreted chemokine gradients along the direction of the flow and subsequently guide tumor cell migration along the flow direction via chemotaxis, a phenomena now known as autologous chemotaxis [70, 72]. Using a 3D microfluidic platform, recent work from the Kamm lab showed that IFs can redistribute focal adhesion kinase to the upstream side of

the tumor cells via β 1-integrin on the cell surface, leading to cell migration against the flow direction [138, 227]. More recently, the Munson lab showed that IFs can influence brain tumor cell invasion via both autologous chemotaxis (CXCR4/CXCL12 axis) and mechano-sensing (CD 44) [73].

The TME is complex, and it consists of extracellular matrices and interstitial fluids as well as other cell types such as stromal, immune, endothelial, and normal epithelial cells [7, 228-230]. The question of whether IFs can modulate other cell types within the TME, and subsequently regulate tumor invasion, has been explored recently [226, 228]. Using a fibroblast and melanoma tumor cell co-culture assay, work from Shieh *et al.* demonstrated that IFs modulated the fibroblast-ECM interaction via matrix alignment, and subsequently promoted tumor cell invasion [75]. A more recent study conducted by Li *et al.* showed that IFs induced the macrophages to change their phenotype to subsequently promote tumor cell invasion [231]. When examining roles of IFs on tumor invasion, co-culture of stromal (fibroblast), immune (macrophage), or endothelial cells (blood and lymphatic) and tumor cells has started to be explored in the literature [70, 75, 231, 232]. Early stage breast carcinoma consists of mostly normal epithelial as well as malignant tumor cells [5, 233-236], however, the roles of IFs on normal epithelial cells within the TME have not been explored

In vivo, tumors typically appear in the form of a tumor mass or cell clusters. Mounting evidence has shown that cell architecture including direct cell-cell contact and ECM mechanical support critically regulates tumor cell invasion behaviors [228, 233, 237]. It is thus important to create assays that recapitulate the *in vivo* TME. To our knowledge, studies of impact of IFs on tumor invasion are limited to single cell assays [70, 72, 74, 138, 227, 238]. Here, we report a tumor spheroid invasion assay that provided a 3D architecture that mimicked the direct physical

cell-cell and cell-ECM contacts typically seen in the avascular areas of tumors *in vivo* [239]. Using a microfluidic model previously developed in our lab, we investigated breast tumor cell invasion in a co-culturing spheroid model (a 1:1 mixture of malignant and non-tumorigenic cells, MDA-MB-231 : MCF-10A cell line) in the absence or presence of IFs. We show that IFs significantly downregulated the cell-cell adhesion of non-tumorigenic cells and subsequently led to tumor spheroid dissociation.

4.2 Materials and Methods

4.2.1 Fabrication of microwells for spheroid formation

The master mold for the microwell pattern was made using the standard photolithography technique at the Cornell Nanoscale Science and Technology Facility (CNF). The negative feature of the microwell arrays on the silicon master were made using negative photoresist. Briefly, the silicon wafers were dehydrated in 90°C oven for overnight. The wafers were first spun with SU8-100 at 500 rpm at 100 rpm/second for 20 seconds to spread the SU8-100, and spun at 300 rpm/second for 45 seconds to coat the wafers evenly, with a final spun at 1400rpm/second to achieve a thickness of 200 μm . Following that, the wafers were baked for 15 minutes at 65°C and then baked for 90 minutes at 95°C, and cooled down to room temperature for 1 hour. Next, the wafers were exposed (670mJ cm^{-2}) on a contact aligner (ABM Contact Aligner). After waiting for 10 minutes, the wafers were baked for 30 minutes at 65°C and another 45 minutes at 95°C, and cooled to room temperature for 1 hour. After developed for overnight, the wafers were treated with FOTS using a vapor deposition method (Molecular Vapor Deposition) to help releasing PDMS from the silicon master.

4.2.2 Cells, spheroids and 3D spheroid culture preparation.

Cells: Metastatic breast adenocarcinoma cells (MDA-MB-231 cell line) and non-tumorigenic mammary epithelial cells (MCF-10A cell line) were provided by the Cornell Center of Microenvironment and Metastasis. MDA-MB-231 cells were cultured every 3 to 4 days from passage 2 to 20, and used at 50-70% confluency. The growth medium for MDA-MB-231 cells was composed of DMEM high glucose medium (Catalog No. [Cat.] 11965092, Gibco, Life Technologies Corporation, Grand Island, NY), 10% fetal bovine serum (Cat. S11150, Atlanta biologicals, Lawrenceville, GA), and 1% antibiotics (100 units/mL penicillin and 100 µg/mL streptomycin, Cat. 15140122, Gibco). MCF-10A cells were cultured every 3 to 4 days from passage 2 to 10, and used at 70-90% confluency. The growth medium for MCF-10A cells was composed of DMEM/F-12 medium (Cat. 11320033, Gibco), 5% donor horse serum (Cat. S12150, Atlanta biologicals), 20 ng/mL human EGF (Cat. PHG0311, Gibco), 0.5 µg/mL hydrocortisone (Cat. H0888-1G, Sigma-Aldrich, St. Louis, MO), 100 ng/mL Cholera Toxin (resuspend at 1mg/ml in sterile DI H₂O, Cat. C8052-.5MG, Sigma-Aldrich), 10 µg/mL insulin (Cat. 10516-5ML, Sigma-Aldrich), and 5% antibiotics (Gibco). MDA-MB-231 expressing EGFP and MCF-10A cells expressing dTomato variants were kind gifts from Dr. Joseph Aslan at the Oregon Health & Science University. Fluorescently labeled MDA-MB-231 and MCF-10A cells were cultured in the same way as the non-labeled cells and were used for the co-culture spheroid experiments.

Spheroids: Tumor spheroids with uniform size were generated using a microfabricated microwell array platform (See Fig. 15 and also work from the Ma lab [240]). Briefly, each spheroid was formed within a 200 µm diameter and 220 µm height non-adherent microwell treated with 1% pluronic F-127 solution (Cat. P2443-250G, Sigma-Aldrich) (see Fig. 4.1A). A 36 by 36 microwell array was patterned in a thin PDMS membrane with a dimension of 1cm × 1cm (Fig. 4.1B), and 6 of the microwell arrays were placed in 6 wells out of a 12-well plate (Fig. 4.1C). To prepare

three different types of spheroids, the protocols were slightly different. For co-culture spheroids, 2 million cells (1:1 ratio of MDA-MB-231:MCF-10A) suspended in 2.5mL medium (1:1 ratio of DMEM and DMEM/F12 growth media) were introduced to each well of the 12-well plate. For MCF-10A spheroids, 2 million MCF-10A cells suspended in 2.5mL F12 growth medium were introduced to each well of the 12-well plate. Cells were first allowed to settle down into all microwells for 30 minutes in the incubator before the device was placed on a rocker at a speed of 4RPM (Boekel Scientific, Rocker II Model 260350). Spheroids were formed after overnight (see Fig 4.1) and cultured for 5 to 6 days before experiments, with medium change every 2-3 days. This design allowed us to generate about 1296 spheroids of approximately 100 μm in diameter in a robust way. We targeted this spheroid size so that spheroids can fit within the microfluidic device with the device height constraint of 200 μm . For MDA-MB-231 tumor spheroid formation, 1.25 million MDA-MB-231 cells were suspended in 2.5mL DMEM growth medium supplemented with 4.5% Matrigel (Cat. 356234, Corning, Bedford, MA) (v/v) were introduced to each well of the 12-well plate. The supplemented Matrigel was to help the MDA-MB-231 cells to form compact spheroids. Cells were allowed to settle down into all microwells for 40 minutes on ice pack and then placed in the incubator for spheroid formation. Spheroids were formed after overnight and cultured for 2-3 days before experiments.

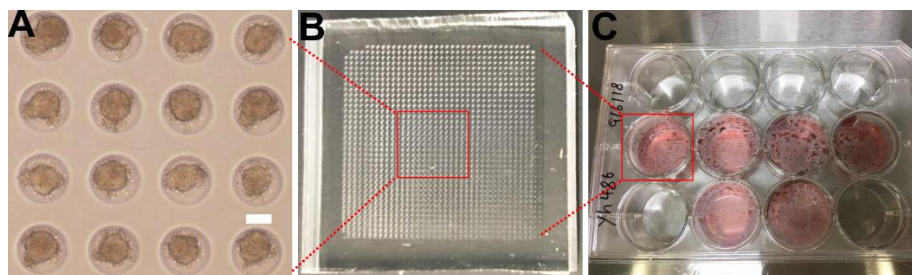


Figure 4.1: Robust and high throughput tumor spheroid formation assay. A. Micrograph of tumor spheroid formation within the microwells. Each microwell has a diameter of 200 μm and a depth of 220 μm . B. A PDMS device (1cm by 1cm) contains an array of 36 by 36 microwells, each microwell can culture one spheroid. C. 12-Well plate is used for spheroid formation and growth.

6 out of the 12 wells contain a PDMS spheroid formation device. Typically, spheroids collected from 4 PDMS arrays are used for each experiment. Scale bar is 100 μm .

3D spheroid culture: To prepare spheroid embedded collagen matrices, 60 μL Type I collagen from stock concentration of 5.0 mg/mL (Cat. 354249, Corning, Discovery Labware Inc., Bedford, MA) was first titrated with 1.32 μL 1N NaOH and 20 μL 10X M199 (Cat. M0650-100ML, Sigma-Aldrich) to yield a final pH of approximately 7.4. The collagen was then mixed with the collected spheroids in medium (1:1 ratio DMEM : DMEM/F12 growth medium for co-culture spheroids, F12 growth medium for MCF-10A spheroids, and DMEM growth medium for MDA-MB-231 spheroids) to a final volume of 200 μL . The final average spheroid concentration was approximately 33 spheroids per device (about 1 spheroid per mm^2 under the top view) and the final collagen concentration was 1.5 mg/mL. We note that spheroids were collected from four arrays of microwells for each experiment and filtered by a Falcon® Cell Strainer (Cat. 352350, Corning) with 70 μm pores to ensure the uniformity of the spheroid size.

4.2.3 Immunostaining of *E-cadherin*.

MDA-MB-231 cells expressing EGFP and unlabeled MCF-10A cells were used to form co-culture spheroids and used in the microfluidics for both static and flow conditions. Immunostaining was performed within the microfluidics after the spheroid embedded collagen was subjected to the flow for 36 hours. Spheroids with/without flow were first fixed with 4% (v/v) paraformaldehyde (Cat. Sc-281692, Santa Cruz, Dallas, TX) in PBS (Cat. 10010023, Gibco) and washed three times with 1X wash buffer (0.05% Tween-20 in PBS, Cat. P9416-50ML, Sigma-Aldrich). The spheroids were then permeabilized with 1% (v/v) Triton X-100 (Cat. T8787-50ML, Sigma-Aldrich) in PBS, washed twice with 1X wash buffer, and blocked with 0.5% (v/v) Tween-

20 with 3% BSA (Cat. 05470-1G, Sigma-Aldrich) in PBS. Anti-E-cadherin primary antibody (Cat. ab1416, Abcam, Cambridge, MA) solution (1:50) in 1% (w/v) BSA in PBS was flowed through the spheroid embedded collagen and incubated for overnight at 4°C. After washing three times, Alexa Fluor 594 conjugated secondary antibody (Cat. ab150116, Abcam) (1:100) in 1% (w/v) BSA was flowed through the sample and incubated for 1.5 hours in room temperature. The samples were washed three times before being imaged using a Zeiss LSM 710 confocal microscope. A z-stack images with each slice thickness of 14.7 μm were taken for each co-culture spheroid under 10X objective (Pinhole setting is AU=1.01). Fluorescent images were taken for E-cadherin (EX:561, EM:659) and MDA-MB-231 cells (EX:488, EM:536).

4.2.4 Microfluidic design and experimental procedure.

A microfluidic platform (See Fig. 4.2) previously developed in our lab was used to provide spatially uniform IFs through the spheroid embedded collagen matrices [172]. The original design of the device was to confine cell-matrices within the cell channels using the contact lines, where cells were confined in the cell channels only. In the spheroid experiments here, spheroid embedded collagen was introduced to both the cell and the flow channels to increase the experimental throughput (See Fig. 4.2A&B). IFs at flow speed of 2.0 $\mu\text{m}/\text{s}$ were introduced through the flow channel using a syringe pump (Kd Scientific, Model #:78-0230). There were three identical devices as shown in Fig. 4.2A patterned on a (1" \times 3" chip) for parallel experiments.

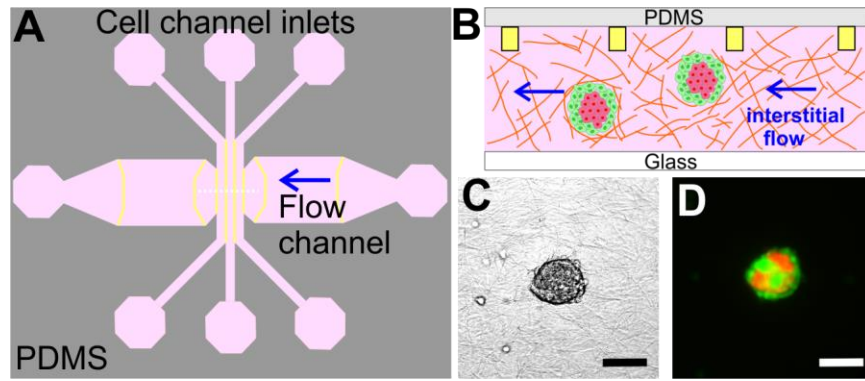


Figure 4.2: Microfluidic platform for tumor spheroid invasion. A. Top view of the microfluidic device design with three cell channels and a flow channel. Spheroid embedded collagen matrices were introduced into the three cell channels and the flow channel and IFs (flow speed = $2.0 \mu\text{m/s}$) were introduced through the flow channel as indicated by the blue arrow. Yellow lines mark the contact lines between two neighboring cell channels. Each cell channel is $400 \mu\text{m}$ wide and the flow channel is 3.0 mm wide, with $200 \mu\text{m}$ in depth and the contact line is $10 \mu\text{m} \times 5 \mu\text{m}$ in cross section. B. Cross sectional diagram of the microfluidic device showing spheroid embedded collagen within the cell channels. Yellow rectangles are the cross section of the contact lines and are not to scale. C-D. Micrographs of a co-culture tumor spheroid [1:1 ratio of MDA-MB-231 (green) and MCF-10A (red) cells] embedded in type I collagen at a concentration of 1.5mg/mL in bright field (C) and in fluorescent mode (D). Scale bar is $100 \mu\text{m}$.

The silicon master of the microfluidic device was fabricated in the Cornell Nanofabrication Facility using a two layer photo-lithography method. The PDMS device was made from the silicon master using a soft-lithography method. Details of the fabrication method can be seen in reference [172]. For sterility, PDMS devices were autoclaved and then treated with oxygen plasma (Harrick Plasma Cleaner PDC-001, Harrick Plasma, Ithaca, NY) for 1 minute on high power mode. To ensure proper surface properties for binding with collagen, the PDMS devices along with a standard $1'' \times 3''$ size glass slides (Fisher Scientific, Pittsburgh, PA) were activated with 1% Poly(ethyleneimine) (Cat. P3143-100ML, Sigma-Aldrich) for 10 minutes followed by a 0.1% Glutaraldehyde (Cat. 16019, Electron Microscopy Sciences, Hatfield, PA) treatment for 30 minutes. The PDMS and glass slides were left in a biohood for overnight in room temperature after being rinsed three times. The PDMS device was then sandwiched between the glass slide and a

plastic manifold. A 0.6% of agarose solution was used to fill the void space around the PDMS device to prevent medium from evaporation during spheroid invasion experiment. In a typical experiment, two such microfluidic chips were prepared in parallel and stored at 4°C for 30 minutes for later use.

At the day of experiments, spheroid-embedded collagen solution was introduced to the cell channels and the flow channel in each of the three devices on a chip (See Figure 16A and B) while the device was in direct contact with an ice block. The microfluidic device was then placed in a petri dish padded with wet tissues, and the petri dish was placed in an incubator to allow collagen polymerization for 45 minutes at 37°C. We note that the temperature ramping rate during polymerization is a critical factor for collagen structure, faster warming leads to a uniform and small pore size network, while slow warming (adopted here) leads to an inhomogeneous large pore size network. More details can be seen in ref [241]). To prevent spheroids from gravitationally settling down to the bottom of the device, the microfluidic chips were positioned up-side-down for the first 10 minutes and then flipped three times more at time points 5, 15, and 15 minutes in the incubator. Following polymerization, 37 °C medium (1:1 ratio for co-culture spheroids, F12 growth medium for MCF-10A spheroids, and DMEM growth medium for MDA-MB-231 spheroids) was flowed into all the channels and both the inlets and outlets of the channels, then were plugged with PDMS filled gel loading tips. The microfluidic device was then transferred to the microscope stage enclosed by an environmental control chamber (WeatherStation, PrecisionControl LLC), which was kept at 37 °C, 5% CO₂ and about 70% humidity. Right before imaging starts, IFs were pumped through the flow channels. Here t=0 is defined as when the flow was introduced, about 2 hours after the spheroid embedded collagen was polymerized. In each

experiment, one device was used as control (no flow) and the other two were connected to a syringe pump to introduce flow of $0.05\mu\text{L}/\text{min}$ (or $2.0\ \mu\text{m}/\text{s}$). Experiments were repeated three times.

4.2.5 Imaging and data analysis.

An inverted microscope (IX81, Olympus America, Center Valley, PA, USA) with a CCD camera (Orca-ER, Hamamatsu Photonics, Japan) was used for all the invasion experiments. In a typical experiment, the middle z-plane of the spheroids in the channels were captured using a 10X objective (Olympus, NA=0.3) in bright field mode (Figure 16C) for all three types of spheroids, and in green fluorescent (EX:460-500nm, EM:510-560nm) and red fluorescent (EX: 510-560nm, EM:572.5-647.5nm) modes (Figure 16D) for co-culture spheroids. For co-culture and MDA-MB-231 spheroids, a sequence of 108 images was captured every 20 minutes for a total of 36 hours. For MCF-10A spheroids, A sequence of 73 images was captured every 30 minutes for a total of 36 hours.

To quantify tumor spheroid dissociation, a stack of time-lapse fluorescent images of one cell type, either EGFP labeled MDA-MB-231 cells or dTomato red MCF-10A cells, was used to calculate spheroid sizes with an in house Matlab program. Here, the cell density along the y-axis of Fig. S2A,B is computed using the azimuthal average fluorescence intensity of the cells at a specific radial distance from the center of the spheroid (Figure S2AB). Each cell density profile is for a specific time point, with $t=0$ is about 2 hours after the spheroids were introduced into the collagen matrices. Next, each cell density profile was fitted to a Gaussian function to obtain the sigma value as the spheroid size or radius (Figure S2C), which represents a region where 2/3 of the cells reside. All the spheroid sizes were then normalized to the initial spheroid size.

To quantify the E-cadherin intensity, a Z-stack of confocal images of the co-culture tumor spheroid was taken (shown in Figure S3B), and the Z-stack images were projected onto a 2D image using the Z Project function in ImageJ. Each 2D image summed up all the pixel intensity from each slice using the sum slides function. The average intensity of E-cadherin for each invaded co-culture spheroid was measured, and subtracted the background, and then normalized to initial spheroid size in control and flow. To measure the E-cadherin intensity of MCF-10A cells as single cells and as cell clusters, image from one z-plane was used to measure the average E-cadherin intensity for single and cluster of MCF-10A cells.

To quantify tumor cell morphology, aspect ratio, defined as major over minor axis of single cell, was used. Cells with aspect ratio greater or equal to 2 were considered mesenchymal cells, and otherwise amoeboid cells [238, 242]. A total of 150 invading MDA-MB-231 cell aspect ratios were measured at t=36 hour per condition in each experiment for three repeated experiments.

To quantify MCF-10A spheroid invasion, spheroid periphery was outlined every four hours to obtain the area of the spheroid, and then normalized to the initial spheroid area at $t = 0$ hr.

To quantify tumor cell motility, time-lapse images of tumor spheroid invasion were processed in ImageJ and in house Matlab programs. MDA-MB-231 cells were tracked after they invaded out of the spheroid. Note that the starting time for each cell varied because each cell invaded out from the spheroid at different times. All the tracked trajectories were used to compute the cell migration speed and the mean square displacements (MSDs). For definition of these parameters, please refer to ref. [238]. A total of 60 cells were tracked for each condition in each experiment for three repeated experiments.

All the data were plotted using Matlab or Prism GraphPad software. Student's t-test was performed for two-group analysis using Prism and mean \pm SEM were presented in all numerical results as well as the average line and error bars in the plots.

4.3 Results and Discussion

4.4 IFs promote co-culture tumor spheroid invasion

4.4.1 IFs enable co-cultured tumor spheroid dissociation

To recreate the complexity of the TME, we embedded co-culture spheroids within a type I collagen gel. The co-culture spheroids consisted of non-tumorigenic epithelial cells (MCF-10A cell line), and malignant breast tumor cells (MDA-MB-231 cell line), representing the cell diversity within the TME [5, 228, 236]. Type I collagen provided the 3D architectural support and the spheroid model provided physical cell-cell contacts that is typically present in the *in vivo* environment. When observing co-culture spheroids within the type I collagen gel in the presence and absence of IFs, a striking phenomenon was immediately evident in that the co-culture spheroids dissociated in the presence of IFs in contrast to the no flow case (control) during the starting 36 hour imaging time window (Figure 4.3.). In the case of flow (lower panel of Fig. 4.3A), both MDA-MB-231 cells (Green) and MCF-10A cells (Red) spread out leaving no spheroid core behind. In the case of no flow (control, top panel of Fig. 4.3A), almost all MCF-10A cells stayed within the spheroid core and some MDA-MB-231 tumor cells invaded outwards.

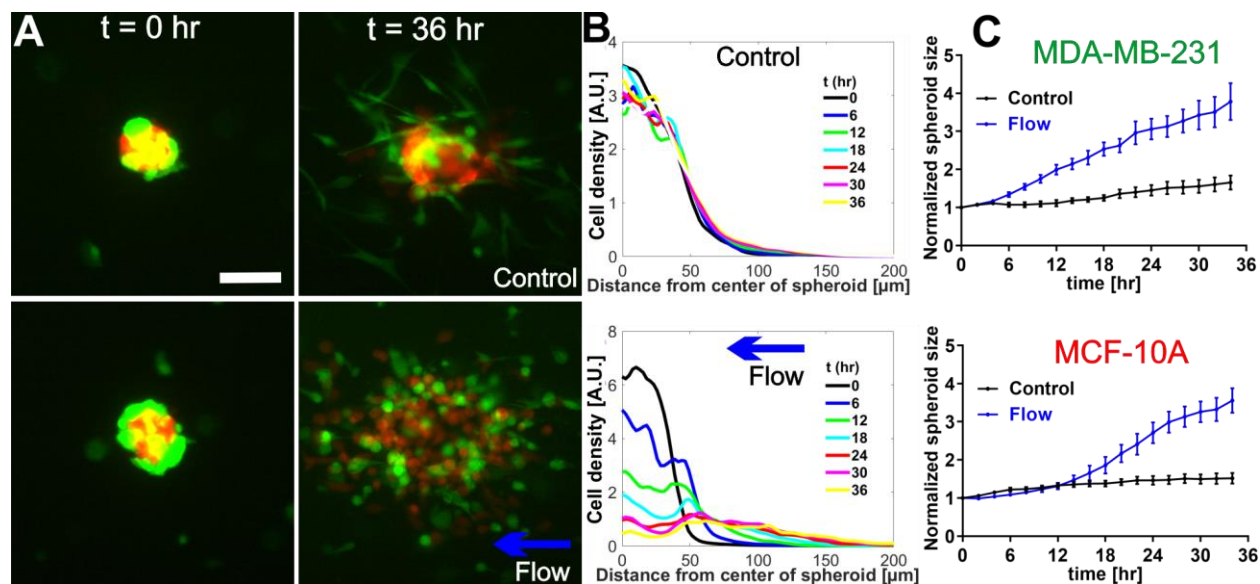


Figure 4.3: IFs enable co-culture tumor spheroid dissociation. A. Micrographs of co-culture tumor spheroid embedded in collagen matrices of 1.5 mg/mL at $t = 0$ hour (left panel) and $t = 36$ hour (right panel) in the absence (top panel) and presence (bottom panel) of the flow. Green: MDA-MB-231 cells expressing EGFP. Red: MCF10A cells expressing dTomato variants. Scale bar is $100 \mu\text{m}$. B. Quantification of MCF-10A distributions using radial cell density in control (top) and flow (bottom). Here, cell density along the y-axis is computed using the azimuthal average fluorescence intensity at a specific radial distance from the center of the spheroid. Each colored line is a radial cell density profile at a specific time point, with $t=0$ is about 2 hours after the spheroids were introduced into the collagen matrices C. Normalized spheroid size time evolution for MDA-MB-231 (top) and MCF-10A cells (bottom) with and without flow. Spheroid size is determined by fitting the radial cell density profile to a Gaussian function, and the sigma value is extracted as the spheroid size. IFs significantly increased spheroid size to almost four-fold of its original size. $N=17$ spheroids (no flow) and $N=11$ spheroids (flow) were used to generate the statistics. Mean and standard error of the mean are shown.

To quantify the co-culture tumor spheroid dissociation, we computed the radial cell density profile using the azimuthal average of the cell fluorescence with the center of the spheroid as $(0,0)$ coordinate. The time evolution of the radial cell density profiles for MCF-10A cells is shown in Figure 4.3B in control (top) and flow (bottom). In control, the radial cell density profiles at different time points were about the same, which was consistent with Fig. 4.3A (top panel) where MCF-10A cells remained intact within the spheroid core. In the presence of the flow, the radial cell density profile spread out distinctly as time progressed, indicating that the MCF-10A cells

invaded away from the spheroid center and the spheroid core disappeared towards the end of the experiment. The radial cell density profiles for MDA-MB-231 cells are shown in Fig. 4.4A, in which the cell spreading difference between flow and control was less pronounced compared to MCF-10A cells.

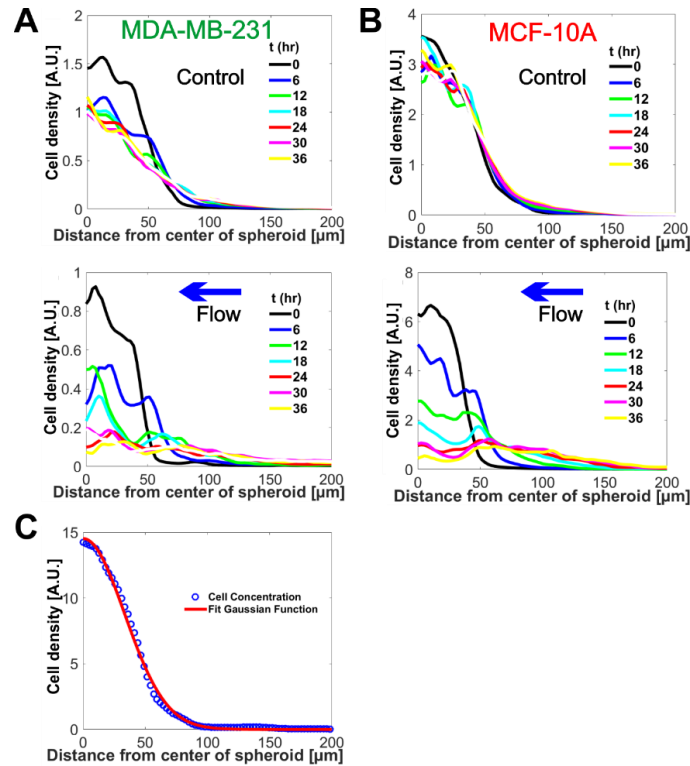


Figure 4.4: Time evolution of radial cell density profile to quantify tumor spheroid dissociation using azimuthally averaged radial cell intensity. A, B. The radial cell density at various time points for MDA-MB-231 cells (A) and MCF-10A cells (B) in control (top panel) and flow (bottom panel). C. A radial cell density profile (at $t=0$ for MCF-10A cells) is fitted to a Gaussian function. The fitted sigma value is used as the size (radius) of the spheroid, which represents the region where $2/3$ of the cells reside.

To quantify the spheroid size, we fitted the radial cell density profile shown in Fig. 2B to a Gaussian function (see Figure 4.4C). The fitted sigma value of the Gaussian function was used as the spheroid radius (or size) as shown in Fig. 4.3C. We note that tumor spheroid size (radius) here represents a region in which $2/3$ of the cell population resides. In Fig. 4.3C, spheroid size for

both MDA-MB-231 cells and MCF-10A cells increased in the presence of flow in contrast to the no flow case. For MDA-MB-231 cells, the normalized average spheroid size was about 2 fold larger in flow (3.8 ± 0.49 fold) compared to control (1.7 ± 0.18 fold) at $t=36$ hours (Figure 4.3C top panel). For MCF-10A cells, the average normalized spheroid size was also about 2 fold larger in flow (3.6 ± 0.32 fold) compared to control (1.5 ± 0.14 fold) at $t=36$ hours (Figure 4.3C bottom panel).

Our results show that IFs increased the spheroid sizes almost 4 fold compared to the initial spheroid size for both cell types in the presence of flow, significantly larger than the spheroid size increase in the absence of flow. We note that the spheroid dissociation had about 14 hours delay in the case of MCF-10A cells in contrast to about 4 hours delay for MDA-MB-231 cells (Fig. 4.3C). This striking difference indicated that the adhesion forces that were essential for the formation of spheroids were different for MDA-MB-231 and MCF-10A cells, and this adhesion force is stronger in the case of MCF-10 cells than that of MDA-MB-231 cells. From this observation, we conjectured that the dominant force that kept the spheroid together was the cell-cell adhesion via E-cadherin for MCF-10A cells, and a second force was the relatively weak cell – ECM adhesion or cell-cell adhesion via N or P cadherins for MDA-MB-231 cells. We thus further investigated whether IFs promote co-culture spheroid dissociation by down regulating the cell-cell adhesion molecule, E-cadherin, of MCF-10A cells.

4.4.2 IFs promote co-culture tumor spheroid dissociation via downregulating cell-cell adhesion E-cadherin of the non-tumorigenic MCF-10A cells.

We quantified E-cadherin expression of MCF-10A cells and MDA-MB-231 cells using a standard immunostaining method. Fig. 4.5A shows the total E-cadherin expression of the co-culture spheroid in the control (top panel) and in the presence of flow (low panel), in which the

images represented a maximal z-projection of a z-stack images. For single image slices from the z-stacks, please see Figure 4.6. In control, cells were mostly connected within the spheroid while cells dissociated in the presence of the flow. To examine closely the relation of E-cadherin expression and the cell types, we superimposed an image of green MDA-MB-231 EGFP cells onto the image of red E-cadherin expression of the co-culture spheroid (See Fig. 4.5B). Fig. 4.5B showed that E-cadherin was mostly expressed on MCF-10A cells, with almost none on MDA-MB-231 cells, consistent with the literature [243].

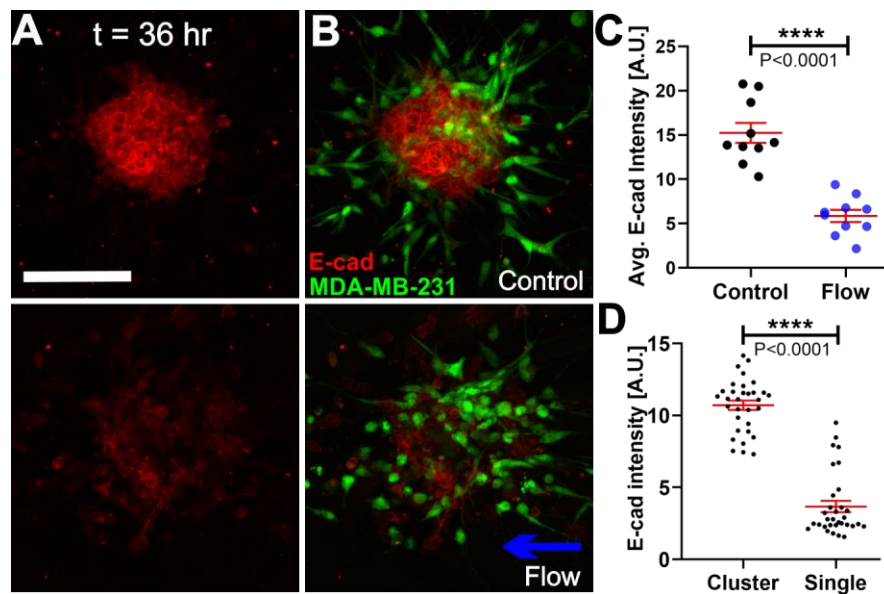


Figure 4.5: IFs promote co-culture tumor spheroid dissociation via downregulating E-cadherin of the non-tumorigenic MCF-10A cells. A. Micrographs of E-cadherin expression of co-culture spheroid using immunostaining in the absence (top) and presence (bottom) of the flow. B. Corresponding images of MDA-MB-231 cells expressing EGFP (Green) superimposed onto the E-cadherin expression image of the co-culture spheroid shown in A in the absence (top) and presence of the flow (bottom). Scale bar is 100 μm . C. Average E-cadherin intensity of the co-culture spheroids in control and flow condition. N=10 spheroids in each condition were measured. D. Average E-cadherin intensity of MCF-10A cells as cluster remaining in the spheroid core v.s. cells as single cells invading out of the spheroid.

We then quantified the E-cadherin intensity of co-culture spheroids in control and flow using fluorescent images such as the one shown in Fig. 4.5A. The average E-cadherin intensity

was significantly higher in control than in flow (Figure 4.5C). To address our question of whether E-cadherin was downregulated by IFs for single MCF-10A cells, we measured the average E-cadherin intensity of MCF-10A cells within a cluster in comparison to the average E-cadherin intensity of MCF-10A cells as individual cells that invaded out of the co-culture spheroids. The average E-cadherin intensity was significantly higher in the cluster compared to those MCF-10A single cells (Figure 4.5D). We note that this measurement was performed on single image slice for both cell cluster and single cells to exclude the overlapping signal from other z-plane images. These data suggest that IFs downregulated cell-cell adhesion via reducing E-cadherin expression in the MCF-10A cells, as a result, the MCF-10A cells disassociated in the presence of the flow.

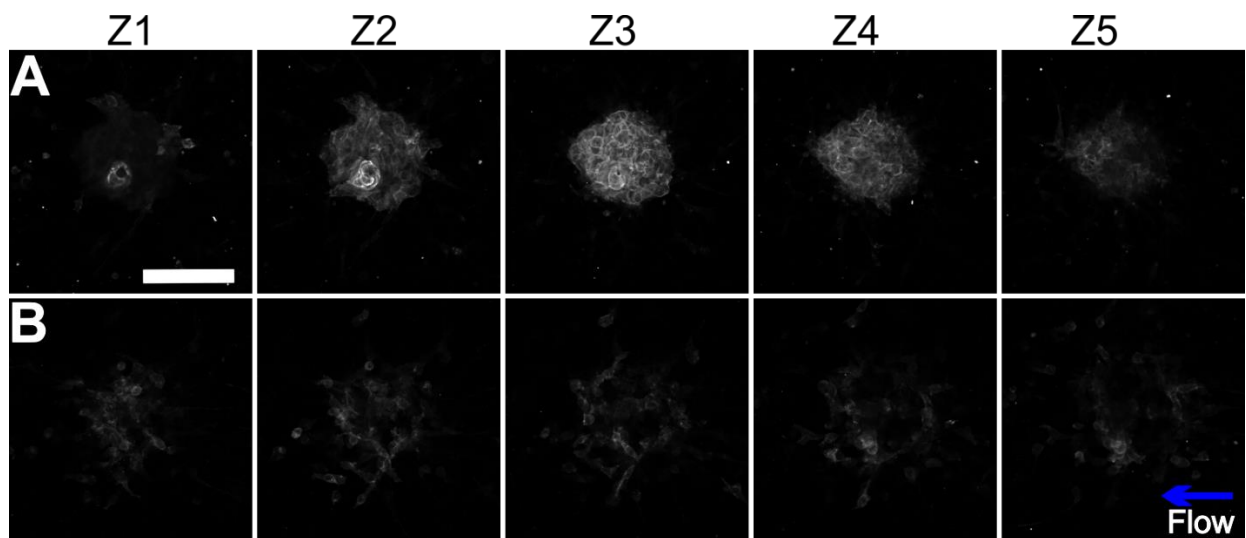


Figure 4.6: Confocal images of E-cadherin on single slices from a z-stack images of the invaded co-culture spheroid in control (A) and flow (B). Each image slice has a thickness of 14.7 μm .

To further understand the roles of IFs in co-culture spheroid dissociation, we investigated cell shape and motility in the presence and absence of flow. Interestingly, we found that metastatic MDA-MB-231 cells and non-tumorigenic MCF-10A cells responded to flow differently.

4.4.3 IFs promoted an amoeboid over mesenchymal cell motility of the malignant MDA-MB-231 cells.

In the absence of flow, MDA-MB-231 cells invaded out of the spheroid core to less of an extent than the case of with flow. In the absence of flow, the cells were found to be more elongated and mesenchymal like in control than round and amoeboid (Fig. 4.7A). This observation was consistent with our previous findings on the IF effects on single MDA-MB-231 cell invasion in 3D collagen matrices [238]. We then used aspect ratio to quantify the cell morphology and found that IFs shifted the aspect ratio towards smaller values (Figure 4.7B). By defining amoeboid cells as cells with aspect ratio smaller than 2.0 [238, 242], IFs decreased the percentage of mesenchymal cells from $79 \pm 4.7\%$ in control to $24 \pm 4.7\%$ in flow (Fig. 4.7C).

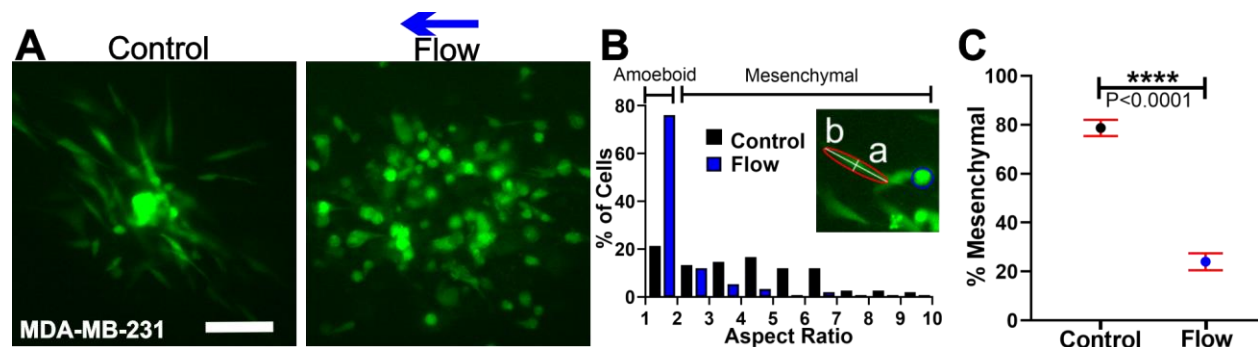


Figure 4.7: IFs promoted amoeboid cell morphology of MDA-MB-231 cells. A. Micrographs of MDA-MB-231 cells expressing EGFP invaded out of the co-culture spheroids at $t = 36$ hr in the absence (left) and presence (right) of the flow. B. Aspect ratio distribution for MDA-MB-231 cells in the absence/presence of flow. The insert image illustrates the definition of aspect ratio, the ratio of major over minor axis of the cell (a/b). C. Percentage of mesenchymal cells in control and flow. 150 cells for each condition were analyzed. Scale bar is $100 \mu\text{m}$.

4.4.4 IFs promoted a single over collective cell motility of non-tumorigenic MCF-10A cells.

In the absence of flow, the majority of the MCF-10A cells stayed connected within the spheroid core, with some peripheral cells migrating collectively as a stream or as a sheet (See Figure 4.8A left image). This observation was consistent with previous literature report that MCF-

10A cells were able to invade collectively following the leader malignant MDA-MB-231 cells from a co-culture tumor spheroid model [235]. In the presence of flow, MCF-10A cells disassociated from the spheroid and migrated as single cells (Figure 4.8A right image). We counted the total number of single MCF-10A cells disassociated from each co-culture spheroid in control and flow as was done in reference [36], and found that the total number of single MCF-10A cells was significantly higher in the flow case than in the control case (Figure 4.8B). The larger number of disassociated single MCF-10A cells in the presence of flow, in contrast to the intact MCF-10A spheroid and collective movement in control, is further consistent with our observation that IFs down regulated the E-cadherin of the MCF-10A cells as shown in Fig. 4.5.

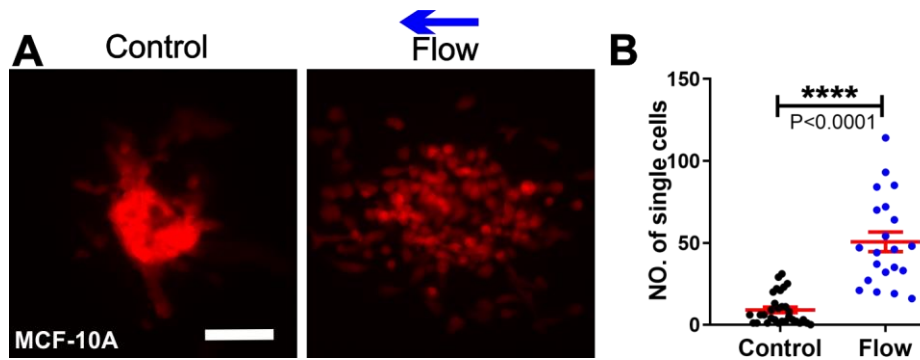


Figure 4.8: IFs promoted single over collective cell invasion of the MCF-10A cells from the co-culture spheroids. A. Micrographs of MCF-10A cells expressing dTomato variants invaded out of the co-culture spheroids at $t = 36$ hr in the absence (left) and presence (right) of flow. Scale bar is $100 \mu\text{m}$. B. Number of single MCF-10A cells dissociated from the co-culture spheroids in the absence/presence of the flow.

We then looked at whether IFs influence the cell morphology of the single MCF-10A cells after invading out of the co-culture spheroids. Different from the flow effect on MDA-MB-231 cells, we found that the MCF-10A cell morphology was about the same for control and flow, as shown in the cell aspect ratio distribution plot in Figure 4.9A. The percentage of mesenchymal cells was $35.4 \pm 5.3\%$ and $38 \pm 2.5\%$ for control and flow, respectively (Fig. 4.9B). In addition,

we found that the percentage of mesenchymal cells was low in both no flow and with flow conditions. These results suggested that MCF-10A cells do not express much integrins that bind to collagen matrix and thus are not as sensitive to IFs as MDA-MB-231 cells that express significant higher level of integrins [243].

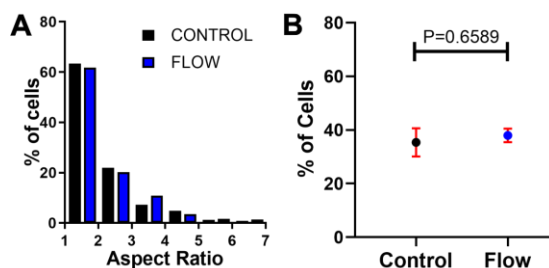


Figure 4.9: MCF-10A cell morphology was not affected by IF. A. Aspect ratio distribution for MCF-10A cells in the absence/presence of flow. B. Percentage of mesenchymal cells in control and flow. 82 cells in control and 366 cells in flow from combining three experiments were analyzed.

4.4.5 IFs significantly enhanced the motility of both the metastatic MDA-MB-231 and non-tumorigenic MCF-10A cells.

To quantify the MDA-MB-231 tumor cell motility from the co-culture spheroid experiments, we tracked each individual MDA-MB-231 cell that invaded out of the spheroids. Using the cell trajectories (Figure 4.10A), we computed the tumor cell migration speed as well as its mean square displacements (MSDs). The cell migration speed was significantly enhanced by flow, with an average speed of $0.23 \pm 0.01 \mu\text{m}/\text{min}$ in control compared to $0.30 \pm 0.01 \mu\text{m}/\text{min}$ in flow (Figure 4.10B), with a 30% increase. To examine how far the tumor cells spread in space, we computed MSDs and found that the MSDs were greater in the presence of flow than in the absence of the flow (Figure 4.10C), indicating MDA-MB-231 tumor cells spread further in the presence of flow. In addition, using the first order diffusion equation, we approximated the diffusion coefficients for tumor cells are $4.23 \mu\text{m}^2/\text{min}$ for no flow case and $6.41 \mu\text{m}^2/\text{min}$ for the

flow case, further confirming that flow enhanced the tumor cell motility. The cell migration persistence was not influenced by IF, as shown in Figure 4.10D.

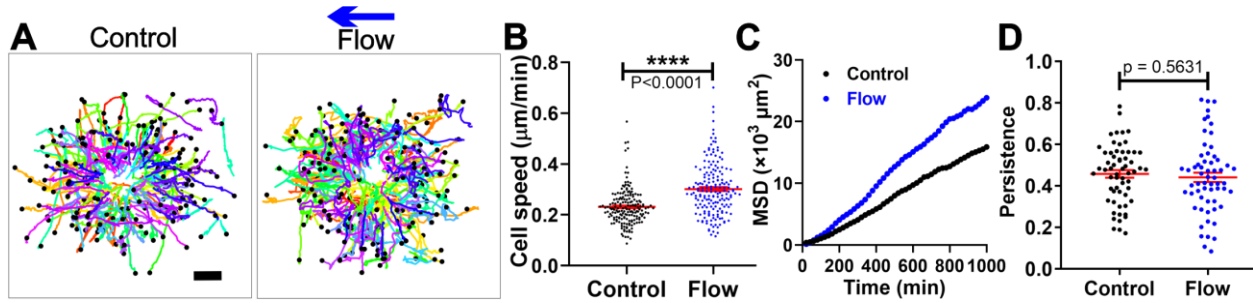


Figure 4.10: IFs enhanced the cell motility and MSDs for malignant MDA-MB-231 cells invading out of the co-culture spheroids. A. Trajectories of MDA-MB-231 cells invading out of the co-culture tumor spheroid in control (left) and flow (right). 180 cell trajectories were presented in each condition. The time duration of the trajectories is 11-35 hours (average of 22 hours) for control and 8-35 hours (average of 27 hours) for flow case. Scale bar is 100 μm . B-D. Tumor cell migration speed, mean square displacements (MSDs), and cell migration persistence for MDA-MB-231 cells with/without flow. 169 cells in control and 121 cells in flow with time duration of 17 hours were used for the MSDs plot.

We also compared the cell migration velocity (V_x) and the persistence (P_x) with respect to the flow direction in control and flow, but did not find any significant bias in the flow direction (Figure 4.11). This result was similar to the results from our previous findings when single MDA-MB-231 tumor cells were embedded within type I collagen [238].

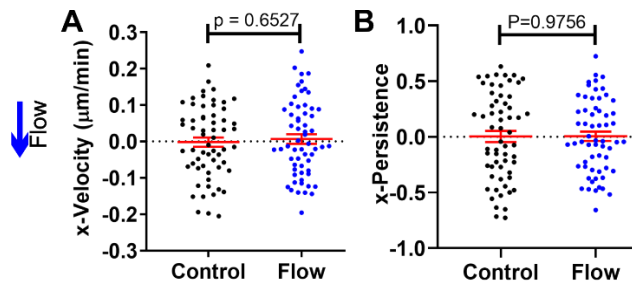


Figure 4.11: No significant directional cell migration was observed for MDA-MB-231 tumor cells from the co-culture spheroids. A. Tumor cell velocity in the flow direction. Control: $V_x = -0.0019 \pm 0.013 \mu\text{m}/\text{min}$. Flow: $V_x = 0.0065 \pm 0.014 \mu\text{m}/\text{min}$. B. Tumor cell persistence in the flow direction. Control: $P_x = 0.0035 \pm 0.051$. Flow: $P_x = 0.0055 \pm 0.043$. Positive sign indicates a direction against the flow and negative sign indicates a direction that is along the flow.

Similarly, we analyzed the motility of the non-tumorigenic MCF-10A cells that have detached and migrated individually out of the co-culture spheroids. Interestingly, we found that IFs also increased the motility and MSDs of the single MCF-10A cells, as demonstrated in Figure 4.12A-C. We note that the number of single cells is less in control case than in the flow case because MCF-10A cells preferred to migrate collectively rather than individually in the absence of flow, as shown in Figure 4.8A and B. Finally, a noticeable observation from the trajectory plots (Fig. 4.10A v.s. 4.12A) and the MSD plots (Fig. 4.10C v.s. 4.12 C) was that the malignant MDA-MB-231 cells spread much further compared to the non-tumorigenic cells in both control and flow, but the migration speed in the presence of flow was comparable for the two cell types (Fig. 4.10B v.s. 4.12B), with $0.30 \pm 0.01 \mu\text{m}/\text{min}$ for MDA-MB-231 cells and $0.33 \pm 0.0087 \mu\text{m}/\text{min}$ for MCF-10A cells. This result can be explained by the fact that MCF-10A cells had a much longer delay time before starting to invade compare to MDA-MB-231 cells (as discussed earlier), thus the total tracking time is significantly shorter for MCF-10A cells than MDA-MB-231 cells. Interestingly, the cell migration persistence is significantly larger in the presence of flow compared to no flow case (Fig.4.12 D), possibly due to the co-culture spheroid dissociation.

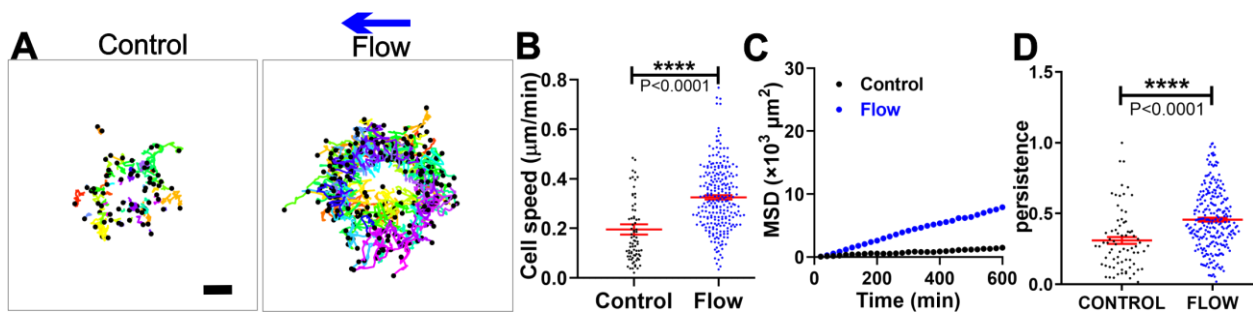


Figure 4.12: IFs enhanced the cell motility and MSDs for the non-tumorigenic MCF-10A cells invading from the co-culture spheroids. A. Trajectories of MCF-10A cells invading out of the co-culture tumor spheroid in control (left) and flow(right). The time duration of the trajectories is 2-31 hours (average of 14 hours) for control and 2-27 hours (average of 10 hours) for flow case. Scale bar is 100 μm. B.Cell migration speed for MCF-10A cells with/out flow. C-D. The MSDs and persistence for MCF-10A cells in control and flow. 46 cells in control and 107 cells in flow

with time duration of 10 hours were used for the MSDs plot. Data is presented by combining three repeating experiments.

4.5 IF is not sufficient to induce non-tumorigenic MCF-10A spheroid invasion

The distinct dissociation of the flow impact on the co-culture spheroids led us to ask a question of whether it is because of the impact of flow alone or the synergistic of the co-culture condition with the presence of MDA-MB-231 tumor cells. To answer our question, we performed experiments on IF on the MCF-10A spheroid using the same experimental conditions as the co-culture spheroid invasion experiments. Interestingly, we did not see a significant difference in invasion within the 36 hour window for control and flow (Figure 4.13). Note that 36 hour window used here was the same time duration for co-culture spheroid experiments. By the end of the flow experiments, most of the MCF-10A spheroids were remained in the core with only a few periphery cells probing out collectively in both control and flow (Fig. 4.13ABC left two columns). We then extended our experiment time window to 60 hours, in which we observed about 14% spheroids dissociate completely (Fig. 4.13 B right column) and about 27% spheroids dissociated partially (Fig. 4.13 C right column), where the spheroid core is remained with some cells invaded out from the spheroids.

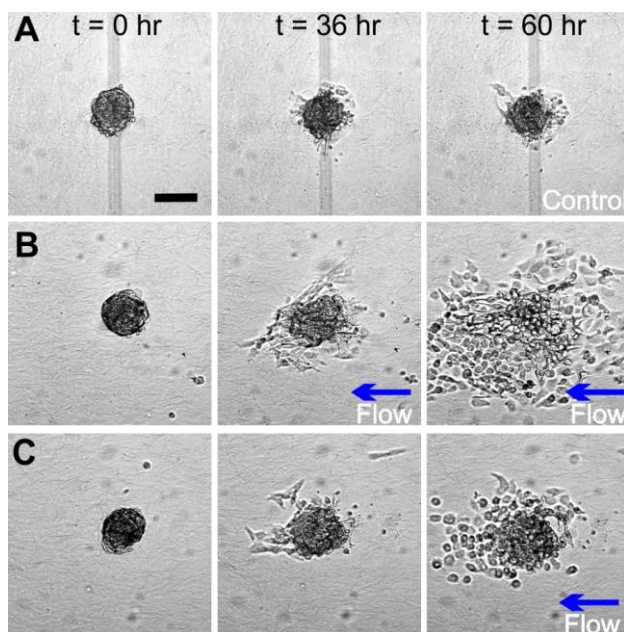


Figure 4.13: IF is not sufficient to induce MCF-10A spheroid invasion. Micrographs of MCF-10A spheroid embedded in collagen matrices of 1.5 mg/mL at t = 0 hour (left panel), t = 36 hour (middle panel), and t = 60 hour (right panel) in the absence (A) and presence (middle and bottom panel) of the flow (B and C).

The differential impact of IFs on the co-culture spheroids and the MCF-10A spheroids suggested that the presence of MDA-MB-231 within the co-culture assays facilitate the MCF-10A cell invasion in the presence of flow. Since the MCF-10A cells are mostly non-invasive in the co-culture spheroid in static condition, we concluded that a synergistic effect of MDA-MB-231 cells and IFs is promoting the MCF-10A cell dissociation and invasion. Another possible reason we speculated was the different cell-cell adhesion levels in these two types of spheroids. The cell-cell adhesions within the MCF-10A spheroids is stronger than the cell-cell adhesions within the co-culture spheroids, because half of the cell population (MDA-MB-231 cells) do not exhibit cell-cell adhesions E-cadherin. As a result, IF was sufficient to induce the co-culture spheroid dissociation, but could partially promote MCF-10A spheroid dissociation.

4.6 IFs inhibit malignant MDA-MB-231 spheroid invasion

4.6.1 IFs reduced the tumor cell motility

MDA-MB-231 cells are characterized as malignant cells that already lost the cell-cell adhesion, as a result, cells were not able to form compact spheroids using the same protocol as for the co-culture or MCF-10A spheroids. To generate MDA-MB-231 tumor spheroids on the non-adherent microwells, we supplemented Matrigel, an ECM that is similar to the basal membrane surrounding the epithelial and myoepithelial layer in the mammary duct, to the cell solution for compact spheroid formation. When subjecting the MDA-MB-231 tumor spheroids to IFs, we discovered that flow inhibit tumor spheroid invasion (Figure 4.14). Visually, we observed that MDA-MB-231 tumor cells significantly invaded out of the spheroid and spread much further in the absence of flow compared to the case of flow (Figure 4.14A). To quantify tumor cell motility, we first tracked each cell after they invaded out of the spheroids to obtain the cell trajectory in the absence and presence of IFs (Figure 4.14B). Here, the start position for each trajectory was at the spheroid periphery. Interestingly, the cell trajectories shown that tumor cells invaded much further in the control case than in the flow case. Using the cell trajectories, we computed the cell migration speed (Figure 4.14C) and the cell velocity along the flow direction (Figure 4.14D). The average cell migration speed in control (average value of 0.32 ± 0.01 $\mu\text{m}/\text{min}$) was almost two times faster than the cell speed in flow (average value of 0.180 ± 0.001 $\mu\text{m}/\text{min}$). In addition, no directional migration was observed for the tumor cells in the MDA-MB-231 spheroid assay with/out flow, consistent with our previous results in the single MDA-MB-231 cell experiments.

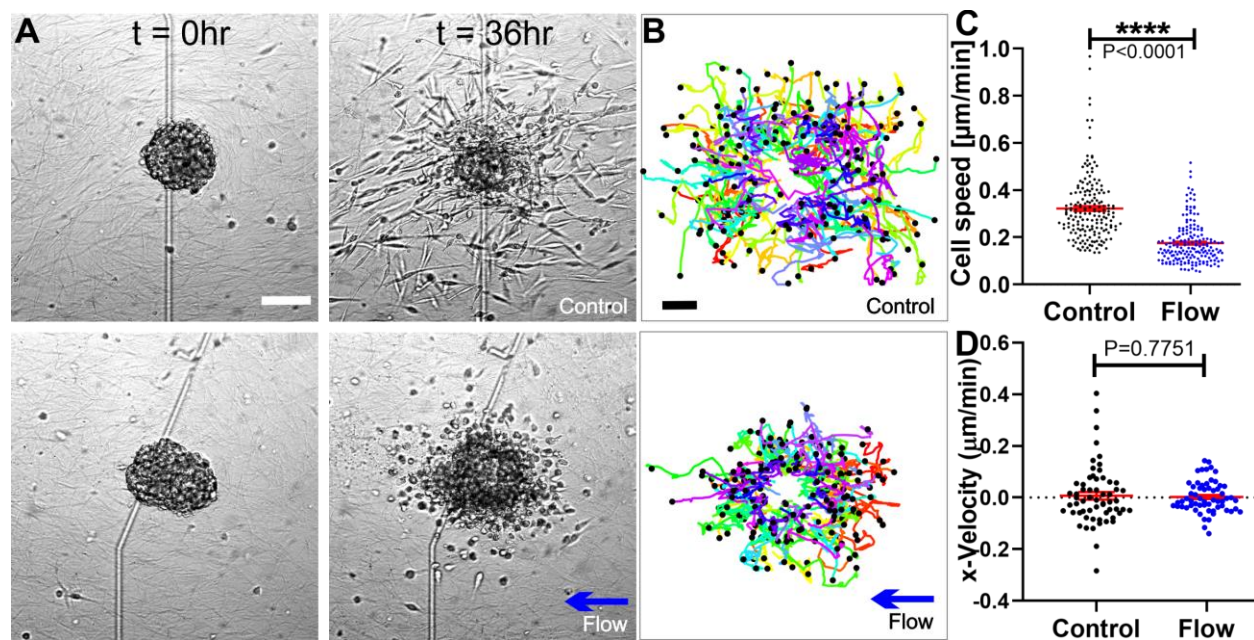


Figure 4.14: IFs inhibit MDA-MB-231 tumor spheroid motility. (A) Micrographs of MDA-MB-231 tumor spheroid embedded in collagen matrices of 1.5 mg/mL at t = 0 hour (left panel) and t = 36 hour (right panel) in the absence (top panel) and presence (bottom panel) of the flow. (B) Trajectories of MDA-MB-231 cells invading out of the tumor spheroid in control (top) and flow (bottom). 180 cell trajectories were presented in each condition. The time duration of the trajectories is 4-34 hours (average and SD of 20 ± 6.7 hours) for control and 4-36 hours (average and SD of 23 ± 7.1 hours) for flow case. Scale bar is 100 μm for A and B. (C-D). Tumor cell migration speed and velocity in the flow direction for MDA-MB-231 cells with/without flow. Positive sign indicates against the flow and negative sign indicates along the flow.

4.6.2 IFs diminished the tumor cell ability to spread

To learn about the ability of tumor cell ability to spread, we computed the tumor cell migration persistence and the MSDs. Interestingly, we found that the tumor cells are less persistent in the presence of flow than in the absence of flow (Figure 4.15A). Consistent with the cell trajectories, the MSDs plot demonstrates that cells migrate significantly further in flow than in control. In addition, we also observed significantly more cells invaded out from the spheroid in the control case compared to the flow case. This was confirmed when we counted the total number of cells invaded out from each spheroid after 36 hours, with an average of 239 ± 36 cells invaded

out of the spheroid in control compared to an average of 67 ± 10 cells in flow (Figure 4.15C). Taken all together, IFs significantly impair the ability of tumor cell spreading and the ability to invade into its surrounding collagen matrices.

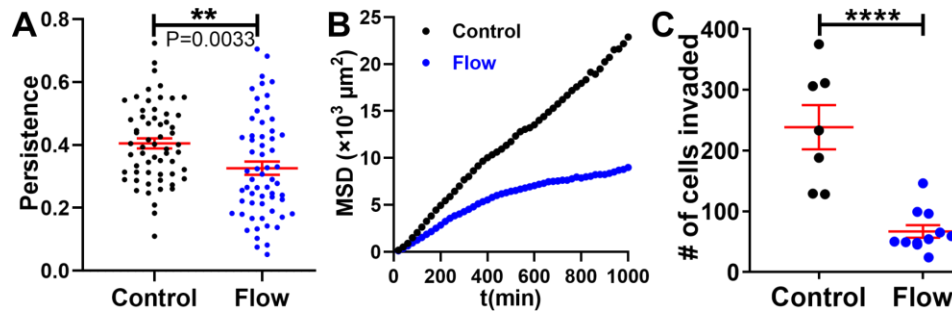


Figure 4.15: IFs inhibit MDA-MB-231 tumor spheroid ability to spread. (A-B) Tumor cell migration persistence and mean square displacements (MSDs) for MDA-MB-231 cells with/out flow. 160 cells in control and 188 cells in flow with time duration of 16 hours were used for the MSDs plot. (C) Number of tumor cells invaded out of the MDA-MB-231 spheroids in control and flow at $t = 36$ hour.

The differential flow impact on the MDA-MB-231 spheroid invasion, in comparison to the co-culture spheroid invasion, led us to hypothesize that IFs play differential role on cell-cell adhesion and cell-ECM adhesions. IFs promoted co-culture spheroid dissociation because flow downregulated cell-cell adhesions E-cadherin, a main driving force that form the co-culture spheroids. On the other hand, the main driving force for MDA-MB-231 spheroid formation is the cell-ECM adhesions via cell surface integrins binding to the supplemented Matrigel. We hypothesize that IFs may strengthen tumor cell integrin ($\alpha 3 \beta 1$) binding on the matrix presented in Matrigel such as laminin, as a result flow inhibit tumor spheroid invasion. Previously, Polacheck *et al.* reported that IF induced a mechanotransduction cascade on the MDA-MB-231 cells embedded on collagen matrix via $\beta 1$ integrins [138]. Future experiments could be conducted to visualize the integrin ($\alpha 3 \beta 1$) expression on the MDA-MB-231 spheroids in the absence/presence of IFs.

4.6.3 IFs promoted amoeboid cell morphology from MDA-MB-231 spheroids

In the absence of flow, we found that the cell population is more elongated and mesenchymal like in control but more round and amoeboid in flow (Fig. 4.16A). We then used aspect ratio to quantify the cell morphology and found that IFs shifted the aspect ratio towards smaller values (Figure 4.16A) and decreased the percentage of mesenchymal cells from $68 \pm 4.7\%$ in control to $16 \pm 4.7\%$ in flow (Fig. 4.16C).

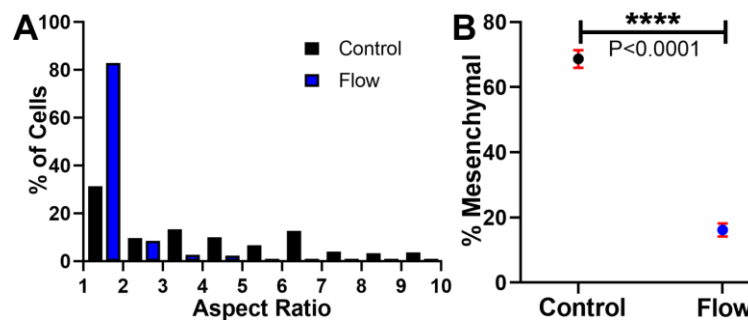


Figure 4.16: IFs promoted amoeboid cell morphology of tumor cells invaded out from the MDA-MB-231 spheroids. (A) Aspect ratio distribution of tumor cells in control and flow at $t = 36$ hour. (B) Percentage of mesenchymal cells in control and flow. 150 cells for each condition were analyzed.

4.7 Conclusion & future perspectives

The TME is complex and heterogeneous. It is therefore important to develop physiologically realistic models that recapitulate the key physical and chemical cues within the TME. Using a co-culture spheroid model, we explored the roles of IFs in tumor invasion. In particular, our results showed that IFs can modulate cells that are other than tumor cells within the TME, and subsequently modulate tumor cell invasion. More specifically, we showed that IFs downregulated the cell-cell adhesion molecule, E-cadherin, of non-tumorigenic cells within the tumor spheroid and promoted tumor spheroid dissociation. Using the MCF-10A spheroid model, we learned that IF alone is not able to dissociate the spheroid, suggesting a synergistic effect of IF

and the presence of MDA-MB-231 cells on regulating the MCF-10A cell migration. The MDA-MB-231 spheroid model formed via cell-ECM adhesion suggesting a differential impact of IF on the integrin-ECM adhesion. In addition to highlighting the roles of IFs in tumor invasion, our work also emphasizes the importance of the interplay between different cell types within the complex microenvironment in studying tumor cell invasion behavior. These insights are important for future designs of *in vitro* assays for cancer biology research, tissue engineering and therapeutic drug testing.

Besides the heterogeneity and diversity of the TME, understanding the evolution of tumor development processes at different stages is equally important. In breast cancer, the transition from normal duct to ductal carcinoma in-situ (DCIS, a preinvasive tumor) and from DCIS to invasive cancer is largely unknown. In addition to the genetic and molecular regulation, the spatial cell-cell organization of the epithelial cells and/or tumor cells along with other cell types could potentially play an important role in regulating tumor cell invasion. Thus, there is a need to develop *in vitro* models to mimic the cell-cell spatial arrangement at different disease stages. For example, in DCIS, the tumor cells typically are enclosed by a layer of normal epithelial cells while in invasive tumor, the tumor cells are prevalent inside and outside of the duct. Our current spheroid model can be extended to better model these cell-cell organizations by rearranging the cell layouts to study how IFs impact tumor cell invasion as the disease progresses from one stage to another.

CHAPTER 5

Summary, conclusion, and future perspectives

5.1 Summary on the roles of IFs on tumor cell invasion

To date, the effect of IFs on breast tumor cell invasion was carried out in four experimental settings: single MDA-MB-231 cell assays with and without FN, MDA-MB-231 spheroid assay, and co-culture spheroid assay (with MCF-10A cells). To have an overview on the impact of IFs on tumor cell invasion at four different experimental settings, we compared the flow induced cell changes in morphology and motility, as shown in Figure 5.1.

In all the experimental settings, IFs were shown to promote amoeboid over mesenchymal morphology of the tumor cells (Fig. 5.1A). The percentage of cells changed from mesenchymal to amoeboid under flow (the difference of percentage of amoeboid cells in no flow vs. with flow) increased from $30 \pm 4.0 \%$, $44 \pm 4.0 \%$, $53 \pm 4.7 \%$, to $55 \pm 4.7 \%$ as the experimental settings changed from single cell assays (no FN and with FN) to spheroid assays (MDA-MB-231 cells only and co-culture of MDA-MB-231 cells and MCF-10A cells).

Across four experimental conditions, IFs enhanced tumor cell migration speed in three assays (both single cell assays and the co-culture spheroid assay) but decreased the cell speed in the MDA-MB-231 cell alone spheroid assay that supplemented with Matrigel (Fig. 5.1B). IFs increased $10 \pm 7.5 \%$, $20 \pm 7.5 \%$, and $30 \pm 7.5 \%$ of the tumor cell migration speed in single cell assay without FN, single cell assay with FN, and co-culture spheroid assay, respectively. In the MDA-MB-231 alone spheroid assay, IFs decreased the cell migration speed to almost half fold ($46 \pm 7.5 \%$ decreased). The result indicates that the supplemented Matrigel inhibit the tumor cell migration in the presence of IFs.

In all the experimental settings, no significant directional cell migration was found after comparing the average cell velocity in the flow direction (Fig. 5.1C). In addition, IFs were shown to decrease the cell migration persistence in all four settings (Figure 5.1D), with significant decrease in single cell assays without and with FN (38 ± 7.5 % and 30 ± 7.5 % decreased) and in MDA-MB-231 spheroid assay (18 ± 7.5 % decreased), and a mild decrease (not statistically significant) in the co-culture spheroid assay (4 ± 7.5 % decreased). This result can be explained by the large population of amoeboid cells in the flow case, because amoeboid cells migrate in a path finding manner and are less directional and persistent compared to mesenchymal cells that predominantly presented in the no flow case.

In the four experimental settings, IFs were shown to significantly decrease the MSD and the diffusion coefficient in three assays without co-culturing but significantly increase the MSD and diffusion coefficient in the co-culture spheroid assay (Fig. 5.1E and F). The percentage of decrease in MSD is 30 ± 7.5 %, 20 ± 7.5 %, and 61 ± 7.5 % and similar percentage decrease was observed when comparing the coefficients in the single assays without and with FN, and the MDA-MB-231 spheroid assay, respectively. In the co-culture spheroid assay, the percentage increase is 50 ± 7.5 % in MSD and 52 ± 7.5 % in diffusion coefficient. These results implied that the MCF-10A cells in the co-culture spheroid model enhanced the MDA-MB-231 tumor cell ability to spread in the presence of IFs.

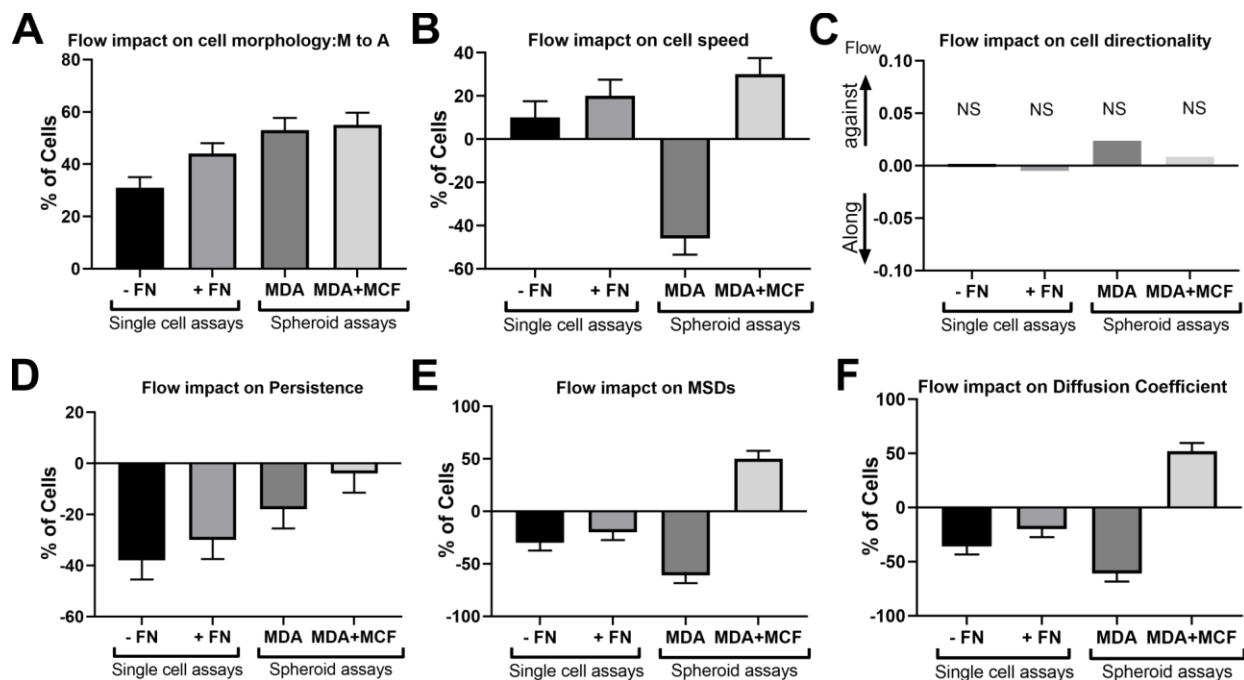


Figure 5.1: Summary on the impacts of IF on tumor cell invasion in four experimental settings: single MDA-MB-231 cell assays without FN and with FN, spheroid assays with MDA-MB-231 spheroid and co-culture spheroid embedded in 1.5 mg/mL collagen matrices. (A) Flow impact on dynamical cell morphology shift from mesenchymal (in control) to amoeboid cells (in flow). (B) Flow impact on the percentage of cell speed change. Positive sign indicates increase and negative sign indicates decrease in percentage. (C) Flow impact on directional cell migration. Positive and negative signs indicate directions against and along the flow direction, respectively. (D-F) Flow impacts on tumor cell migration persistence, MSDs, and diffusion coefficients. Positive and negative signs indicate increase and decrease in percentage, respectively. NS indicates no significant difference when comparing the effect of no flow and with flow. All other plots indicate significant difference when comparing no flow vs. with flow. The error bars are calculated from counting error, $\frac{\sqrt{N}}{N-1}$, where N is the total number of cells analyzed.

Taken together, IFs have differential impact on tumor cell invasion depending on the presence of the other cell type. In both the single cell and spheroid assays only with MDA-MB-231 tumor cells, IFs significantly diminished the tumor cell persistence, MSDs, and diffusion coefficients and thus inhibit the tumor cell's ability to spread further. However, in the presence of MCF-10A cells in the co-culturing spheroid condition, IFs significantly enhanced the tumor cell migration speed, MSDs, and the diffusion coefficient and thus promote tumor cell invasion. These

results suggested that the presence of the non-tumorigenic MCF-10A cells in the co-culture spheroid condition facilitated the malignant tumor cell invasion in the presence of IFs, highlighting the potential importance of a complex microenvironment for tumor cell invasion assays. In addition, IFs could play differential role in modulating tumor cell invasion via cell-ECM and cell-cell adhesions.

5.2 Conclusion

The advantages of microfluidics include the capabilities to capture the spatial and temporal dynamics at single cell level and dissect the complex TME. Using our microfluidic systems, we were able to add or subtract a level of complexity to the system while controlling IFs. Using our microfluidic model, we shown that breast cancer cells embedded in a 3D type I collagen matrix at collagen concentration of 1.5 mg/mL exhibit both an amoeboid and a mesenchymal motility, and IFs promoted the cell population towards the amoeboid motility phenotype. Furthermore, the addition of exogenous adhesion molecules (fibronectin) within the ECM (type I collagen) partially rescues the mesenchymal phenotype in the presence of the flow. Quantitative analysis of cell tracks and cell shape shows distinct differential migration characteristics of amoeboid and mesenchymal cells. Notably, the fastest moving cells belong to the subpopulation of amoeboid cells.

Using the mono-culture (MDA-MB-231 cells) spheroid models supplemented with Matrigel, we discovered that IFs inhibit malignant breast tumor spheroid invasion. This result suggested that IFs may strengthen the tumor cell-Matrigel adhesion (integrin $\alpha3\beta1$ binding to Matrigel) and subsequently inhibit tumor spheroid invasion. Using the co-culture spheroid (a 1:1 mixture of metastatic and non-tumorigenic epithelial cells) models, we found that IFs

downregulated the cell-cell adhesion molecules E-cadherins of the non-tumorigenic cells, and subsequently promoted tumor spheroid dissociation and invasion (Fig. 5.2).

Loss of cell-cell adhesion is a hallmark of cancer, in particular, when normal epithelial cells down regulate adhesion molecule E-cadherin and transition to a mesenchymal state. In vivo, the formation and detachment of malignant tumors are tightly controlled by the cell-cell and cell-ECM adhesion. The studies here indicated that IFs can participate in regulating this balance to favor/prevent tumor cell invasion. Moreover, loss of the integrity of basal membrane in invasive ductal carcinoma is often seen in malignant tumors. Thus, the results from mono-culture spheroid experiments suggested that the presence of basal membrane could serve as a barrier to protect tumor cells from the elevated IFs and subsequently prevent tumor invasion. In contrary, having the tumor cells or epithelial cells directly expose to elevated IFs could drive tumor cell invasion.

Together, these findings highlight the important roles of biophysical forces in modulating tumor cell migration heterogeneity and plasticity, as well as the suitability of microfluidic models in interrogating tumor cell dynamics at single-cell/spheroid and subpopulation level.

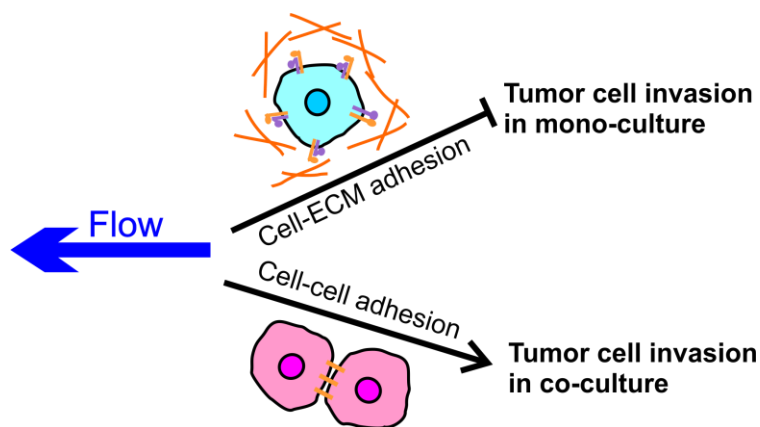


Figure 5.2: IFs play differential role on cell-ECM and cell-cell adhesions to prevent/promote tumor cell invasion.

5.3 Implications

Cancer therapeutic screening: Current platforms that studies roles of IFs on tumor cell invasion can easily be extended to study tumor cell in response to cancer therapeutics under IFs. Because IFs are everywhere in our body, it is one step more physiological realistic to include fluid flows in the therapeutic screening platforms. To date, most of the drug screening studies were carried out in static conditions in *in vitro* systems performed in laboratory and pharmaceuticals. I believe that incorporating IFs to those platforms could potentially transform our understanding of how tumor cells respond to cancer therapeutics, and potentially can aid to facilitate the drug approval processes.

5.4 Future project: IFs on tumor spheroid intravasation using a 3D microfluidic model

Cancer metastasis of solid tumors is a multi-step process, in which tumor cells first detach from the primary tumor, migrate through the interstitial ECM, enter and exit the vascular vessels (intravasation and extravasation), and establish a secondary tumor at a distant organ. Intravasation, a process where cancer cells enter the blood or lymphatic vessels, is a critical rate limiting step in metastasis, but the underlying mechanism is largely unknown. Knowing that IFs re-enters to the venules or drains to the lymphatic vessels, we hypothesize that IFs will drive cancer migration through the ECs of the blood or lymphatic vessels. Indeed, *in vivo* imaging revealed that malignant tumor cells often enter the circulation for further spreading [85]. Boyden chamber model was first used for this study, but its limitation is that it only provided endpoint measurement and population level. Microfluidic models, on the other hand, allow imaging of single cell motility to elucidate the intravasation process.

Our original microfluidic platform with three cell channels was particularly designed to model the tumor cell intravasation process under both intramural and IFs. To improve the throughput and take account of the tumor spheroid size, we fabricated a new microfluidic platform with five parallel cell channels (Fig. 5.3A). To model tumor spheroid intravasation, tumor cell embedded collagen matrices can be introduced and confined within two side cell channels and endothelial cells (ECs) can be introduced to the middle cell channel. Intramural flow can be applied through the middle cell channel to facilitate ECs to form a confluent EC tube. IFs can be applied via the flow channel to study its impact on tumor cell transendothelial migration (Fig. 5.3A bottom panel). In our new device, we were able to grow an EC tube in the middle cell channel two days after the ECs were introduced to the device (Fig. 5.3B). In our preliminary work, we demonstrated that we were able to form an EC tube surrounding by high concentration collagen matrix (4.5mg/mL with 2% Matrigel) in the presence of intramural flow. After introducing co-culture tumor spheroids next to the EC tube, we studied tumor cell migration through the collagen matrix and transmigrate into the EC layer at different time points in the absence of IFs (Fig. 5.3 C and D). Future studies can be continued on using the microfluidic platform to capture the spatial and temporal dynamics of tumor spheroid transendothelial cell migration into the blood vessel under IFs.

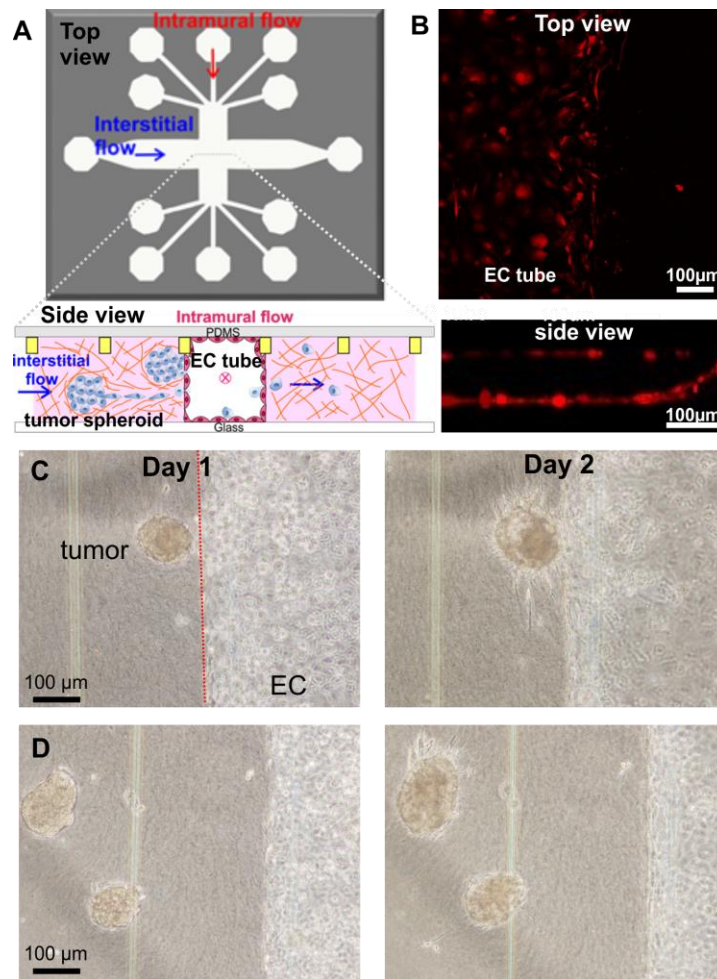


Figure 5.3: Microfluidic modeling of tumor transendothelial migration (TEM) under IFs. (A) Top and side view of the layout of the microfluidic platform. Tumor spheroid embedded extracellular matrices are introduced to the cell channels, and endothelial cells are introduced into the center cell channel to form an engineered blood vessel. Intramural flow is introduced along the central blood vessel, and IFs is along the horizontal direction. (B) Top/side view of a monolayer of HUVECs (Human Umbilical Vein Endothelial Cells with constitutively expressed red fluorescent protein) forming an engineered blood vessel. (C-D) Micrographs of co-culture tumor spheroids (MDA-MB-231 and MCF-10A cells) embedded in collagen matrix at 4.5 mg/mL with 2% (w/w) Matrigel without IFs and a layer of endothelial cells forming a tube with intramural flow perfusion.

5.5 Opportunities, challenges and perspectives

The biophysical microenvironment critically regulates tumor cell invasion. To date, the majority of the cell experiments *in vitro* are carried out in static conditions, whereas biological

flows are everywhere in the human body. Incorporating flows in tumor cell invasion experiments and beyond could potentially revolutionize our understanding in cancer biology. One can foresee the incoming impact will be similar to the impact brought by using 3D ECM in comparison to 2D platform for *in vitro* tumor cell invasion studies. Looking ahead, several challenges require our immediate attentions.

Recapitulating the complex tumor biophysical microenvironment

Microfluidic models have enabled us to learn the individual roles of ECM mechanical properties, intramural and IFs in tumor cell invasion. However, synergistic roles of multiple biophysical factors remain to be explored. Microfluidic devices provide a unique opportunity here, because one can easily introduce biophysical parameters into the platform in a reconfigurable way. An example of such a device is illustrated in Fig. 5.4, where biophysical parameters including intramural and IFs can be added or subtracted with ease. Here, two vascular vessels are created mimicking blood and lymphatic vessels respectively, with tumor cells embedded within ECM placed adjacent to the vascular vessels. In this platform, one can fine tune intramural, IFs and ECM stiffness or pore sizes while observing tumor cell dynamic behavior at the same time. This capability allows for a basic understanding of how these three physical parameters synergistically influence tumor cell invasion within a complex and well-defined TME.

Biochemical environments such as cytokine gradients are traditional driving forces for tumor cell invasion, and are coupled with the biophysical environment. Towards this end, it will be important to first learn how biochemical gradients influence tumor cell invasion [244], and incorporate this information into the biophysical models proposed. Microfluidic models such as the one shown in Figure 5.4 can be easily used to generate cytokine gradients to meet this purpose. For example, we can flow cytokine and buffer respectively into the arteriole and venule channels,

and a cytokine gradient can be established within the tumor embedded ECM space. The integration of biochemical and biophysical environments will be an important step towards a physiologically realistic microfluidic model.

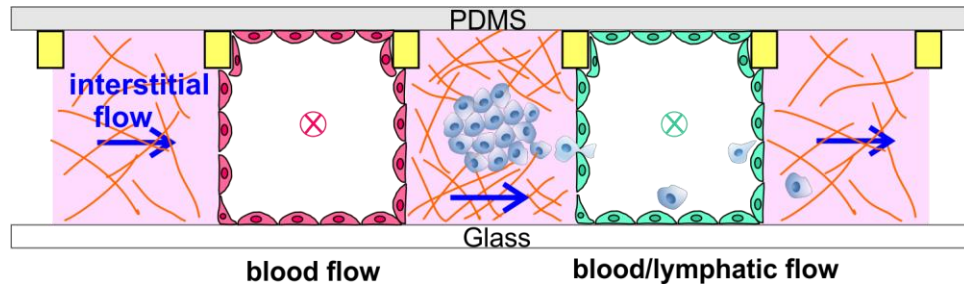


Figure 5.4: Illustration of a microfluidic model recreating the biophysical microenvironment for tumor cell invasion studies. ECM or tumor spheroid embedded ECM (pink) is introduced into three wall-less channels confined by contact lines (yellow rectangular, not to scaled). Blood vessel (red) and lymphatic vessel (green) are formed by growing a layer of blood and lymphatic EC cells respectively. Blood and lymph flows are introduced into two vascular vessels (direction marked by x), and IF is introduced horizontally (direction marked by an arrow).

Creating robust and highly reproducible platforms

Despite the aforementioned many advantages of using microfluidic models, microfluidic technology is still at an early stage, and is not widely accepted by many cancer biology labs. The bottlenecks are availability, ease of use, robustness and reproducibility. Most microfluidic models require engineering training for their use. To make a higher impact in cancer biology, it is important to design devices that are simple in concept, easy to use, and compatible with conventional biology labs. Partnering with industry is one possible route to make microfluidic models available to wider communities [19]. Various agencies such as National Institute of Health provide special funds (e. g. SBIR) to encourage industry/academy partnerships. It is commendable that many research groups have now taken the lead in translating their microfluidic tools into the commercial space. Recent development in 3D printing technologies enables production of

assembly-free microfluidics and eliminates the need of microfabrication for devices at micrometer or millimeter length scale [245]. For ease of use, applying the physical principle of fluids (viscous fingering) to make an EC tube or vascular network within a channel is an alternative method to fabricating complicated features on a device [104]. In addition, a design with gravitational driven flow will be more favorable than using pumps to create biological flows through a channel.

Developing quantitative analysis tools for understanding cell-environment interaction

Microfluidic devices allow us to collect large amounts of quantitative information. However, to make sense of the data, or to come up with a theoretical framework of the subject being investigated, it is important to develop quantitative analysis tools. For understanding the roles of physical parameters in tumor cell invasion, one useful tool is to track tumor cells in 3D in an automatic way. Commercial software such as Imaris has made significant progress in this direction, however, it still cannot handle the dynamic variability of tumor cells. A particularly difficult situation is when a cell dynamically changes its shape and merge and then dissociate with another cell in a trajectory - the tracking program does not have the ability to follow the cells. Recent advances in computer vision and machine learning could potentially resolve tracking of the shape and position of the moving cancer cells in space and time. U-Net is a recent developed program that is available for the biomedical community to automatically map out the dynamic cell shapes in time and in space. A second tool is cell traction force measurements in 3D. The key regulator for cell-physical environment interaction is cell generated force. A number of 3D single cell traction force microscopy methods have been developed for measuring cell generated forces, but are far from easy to use, and are limited to a few labs around the world at the moment [89, 246, 247].

Outlook

Cancer cells are known to be heterogenous phenotypically and genetically. The altered tumor physical microenvironment, e.g. matrix spatial restriction [248], is a highly relevant contributor to the phenotypic and genetic instability of the invading tumor cells. An ultimate solution to the problem is to reveal molecular and cell level information simultaneously with a controlled microenvironment at single cell level. Recent developments in biosensors (mechanosensors and chemosensors) has made this possible. In addition, microfluidics with on chip polymerase chain reaction capability can be incorporated to further study the gene expression for those invading single tumor cells [249, 250]. This platform will be powerful to illustrate the link between gene expression, molecular signaling, and phenotypes of single cancer cells and the altered biophysical microenvironment. Finally, to make an impact in our understanding on how biophysical cues in tumor cell invasion, a close collaboration among microsystems engineers and cancer biologists is critical for moving this field forward. This will require both parties to explore outside their field, attend meetings that they don't normally go to, and not be afraid to ask questions.

APPENDIX

Appendix A: Cooperative roles of interstitial flows and topography on tumor cell invasion

Motivation

Elevated IFs outward from the tumor and aligned collagen fibers perpendicular to the tumor periphery are two key features of malignant tumors (Fig. 1A). Knowing that both of these two features have the same direction from the tumor, we hypothesize that the elevated IFs coupled with collagen alignment can significantly facilitate tumor invasion through the ECM and enter the circulation for subsequent distant dissemination. It has been shown that radial alignment of collagen fibers from the tumor facilitates tumor cell invasion [90]. Understanding the conditions and mechanisms for contact guidance of tumor cells by these topographies will lead to increased understanding of tumor invasion. Previous 2D and 1D studies have been done on contact guidance of aligned fibers, grooves and ridges guiding cell migration, but the combined roles of IFs and surface microtopography in a 3D environment have yet to be clarified.

Materials and Methods

1. *Microfluidic device design*

The topography device consists of one large, major channel that is subdivided into five small subchannels in the middle (Figure 1B). Each subchannel is separated by a PDMS wall. Four of the five subchannels contain 10 μm -width, 20 μm -height ridges to mimic ECM topography. The ridges were designed to have a gradient of different spacings between them to investigate the effect of different confinement and contact guidance conditions. The middle subchannel does not have ridges, and serves as a control (no ridge). IFs are applied from one end of the major channel to the other, in a direction parallel to the ridges.

2. *Microfluidic device preparation and cell seeding*

The device was prepared as described above for the three-channel device, up to the oxygen plasma treatment step. After this step, however, the experiment was modified in order to increase the number of cells that attached to the ridges on the PDMS side of the device. These modifications were made so that more cells attached to the PDMS side, instead of staying in the 3D collagen matrix without making contact with the surface topography features of the device.

Glutaraldehyde treatment was done in order to increase the collagen binding to the device. After oxygen plasma treatment of the PDMS, the PDMS was treated with 1% polyethyleneimine for 10 minutes. It was then treated with 0.1% glutaraldehyde for 30 minutes. The PDMS device is rinsed thoroughly after this step.

The following day, the PDMS was coated with 50 $\mu\text{g}/\text{mL}$ soluble fibronectin for 4 to 5 hours at room temperature. Excess media was then aspirated. Cell seeding on the PDMS side of the device was then done at a concentration of 0.7×10^6 cells/mL. The cells were allowed to settle down on the ridges of the device during overnight incubation in DMEM medium.

The following day, the medium on the PDMS side was aspirated. The device was quickly assembled with the glass slide, Plexiglas, and metal frame, as described for the three-channel device. Then, 1.5 mg/mL collagen was injected into the device via the inlet hole and allowed to polymerize for 30 minutes in the 37 °C, 5% CO₂ incubator.

3. Flow generation and imaging

Similar to the three-channel device, the growth media was flowed into the device via a syringe pump to generate an interstitial flow of 0.04 μL/min (2.0 μm/s flow speed). The control device that did not have flows had its inlet and outlet holes blocked using plugs (pipette tips filled with cured PDMS). The device was placed in a humidified, 37 °C, 5% CO₂ microscope environment chamber for imaging. Imaging was done for 10 hours instead of 16 hours, every 5 minutes, at positions in the subchannels with ridges as well as the control subchannel without ridges.

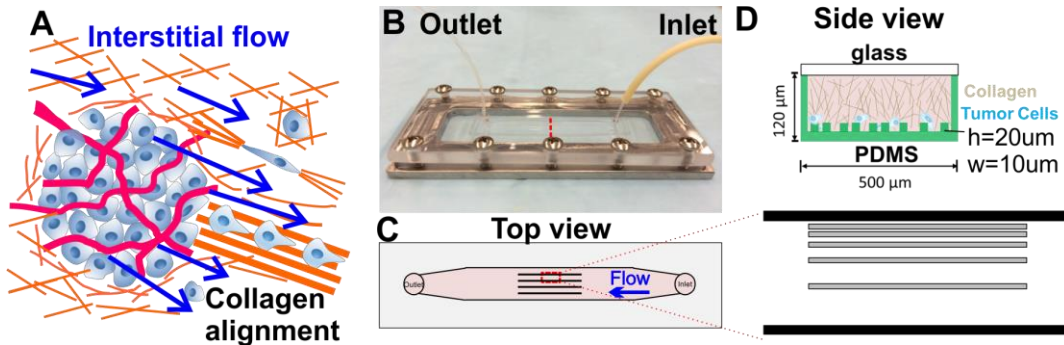


Figure 1: Schematic of microfluidic experimental setup to study the effects of topography and IFs on tumor cell migration. A. Schematic of in vivo tumor with aligned collagen perpendicular to the tumor periphery and IFs outward from the tumor. B. Microfluidic chip assembly. C. Top view of the microfluidic device. The major channel is subdivided into five subchannels, separated by walls (black lines in the middle of the figure). Four subchannels have ridges (shown in the zoom in figure), while the middle subchannel does not have ridges and serves as a control channel. Flow of cell culture medium is from the inlet on the right to the outlet on the left of the device and flow is from right to left. Zoom in figure shows one subchannel, with ridges at various spacing. Each ridge is 10 μm in width and 20 μm in height. The gap spacing between each ridge is 5, 10, 20, 40, and 70 μm from top to bottom.

Results and Discussions

1. Migration along ridges increases speed and persistence lengths

Tumor cell migration in four various conditions (no flow no ridge, no flow with ridge, with flow no ridge, with flow with ridge) were shown in Figure 2A. Each cell was tracked individually over the experimental course and the trajectories were shown in Figure 2B. Cells migrating along ridges can clearly be seen to be guided by the ridge topography, as shown by trajectory plots. Cells were observed to migrate along the sides of the ridges, as well as the top of ridges. Cells on ridges

may migrate in one direction, then switch directions on the ridge, or leave the ridge (either due to cell-cell interactions, the mesenchymal-amoeboid transition in the presence of flow, or other factors).

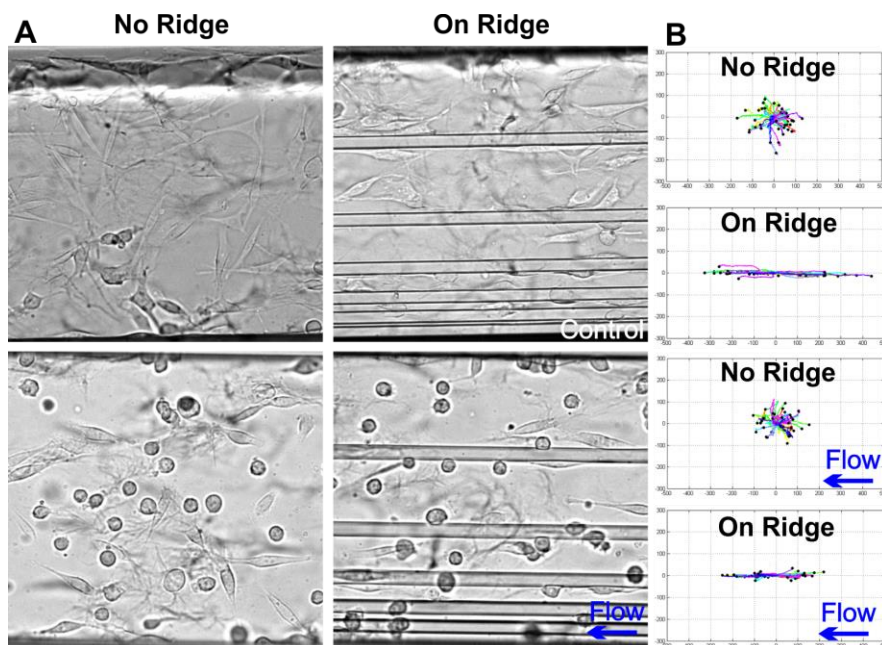


Figure 2: Experimental setting to study IFs and topography on tumor cell invasion. A. Micrographs of MDA-MB-231 tumor cells embedded in a quasi-3D environment, where cells are placed on the PDMS side with/out ridges covered with collagen matrix at 1.5mg/mL concentration. Cells are placed in four conditions: no flow no ridge, no flow with ridge, with flow no ridge, and with flow with ridge. B. Cell migration trajectories in the topography device. The trajectories of 40 motile cells over a 10-hour experiment are plotted on each $1000 \mu\text{m} \times 300 \mu\text{m}$ plot, with the conditions of flow and ridges shown.

We found that the cells that traveled along the ridges had significantly higher average speeds than the cells in the control channel without ridges (Figure 3A), both in the absence and presence of flow. In the absence of flow, the average cell speed was $0.4410 \pm 0.025 \mu\text{m}/\text{min}$ (increased from $0.3066 \pm 0.012 \mu\text{m}/\text{min}$ without ridges, $P \leq 0.0001$), with a 44% increase. In the presence of flow, the average cell speed was $0.4053 \pm 0.028 \mu\text{m}/\text{min}$ (increased from $0.3087 \pm 0.008 \mu\text{m}/\text{min}$ without ridges, $P \leq 0.05$), with a 31% increase. Contact guidance by microtopography thus can be seen to significantly increase motility, in terms of the overall speed of cell migration.

The cells that migrated along ridges also had significantly higher persistence than cells without ridge guidance (Figure 3B). In the absence of flow, the average persistence increased from 0.4351 ± 0.025 without ridges to 0.7429 ± 0.036 with ridges, with a 71% increase. The same trend but less pronounced was found in experiments with flow: the average persistence increased from 0.4286 ± 0.024 without ridges to 0.6241 ± 0.035 with ridges, with a 46% increase. These high

persistence are due to the migration of cells along the ridges, highlighting the importance of surface microtopography in guiding persistent cell migration.

2. IFs may compete with topography guidance in guiding cell migration

As shown in the three-channel device experiments, interstitial flows encourage an amoeboid phenotype. The phenomenon of a mesenchymal-to-amoeboid transition was very clearly observed in the topography device as well. At the beginning of the experiment, many cells were elongated and attached to the ridges. During the course of imaging, we observed that cells that initially were crawling along a ridge at a relatively fast, constant speed, with an elongated push-pulling motion, would slow down and become more round in shape toward the end of the experiment. These cells that became rounded would often detach from the ridge.

The combined effect of fluid flow and topography guidance may provide conflicting signals to the cells. While in the three-channel experiments we found that IFs decrease persistence by encouraging an amoeboid phenotype. Interestingly, we found that IFs significantly decrease the cell migration persistence on the ridges, from 0.7429 ± 0.028 on ridge to 0.6241 ± 0.041 ($P = 0.0009$), with a 20% decrease. Thus IFs imposed a competing effect against the topography on tumor cell invasion.

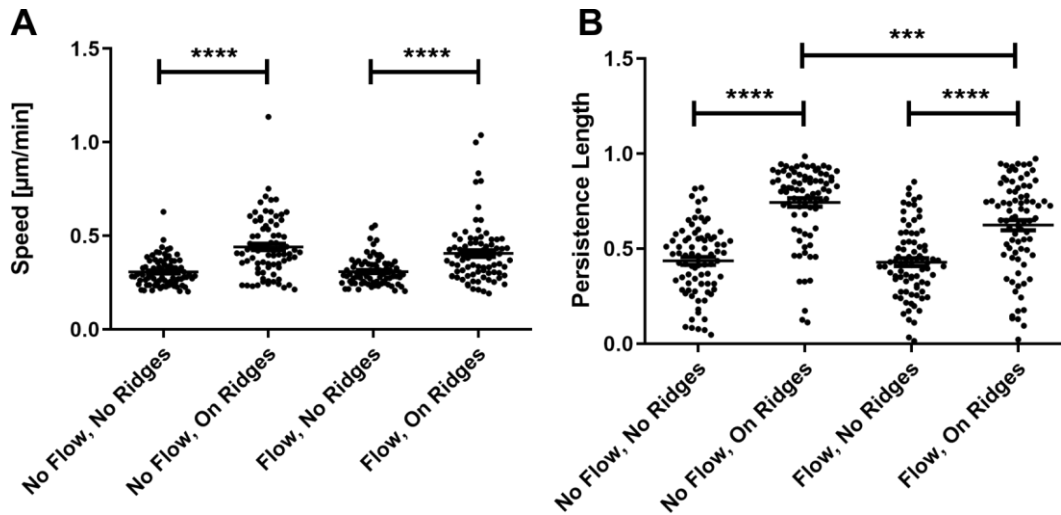


Figure 3. Average cell migration speed (A) and persistence (B) of tumor cells in four conditions. Each group comprises 80 cells.

Appendix B: Micro-indentation method to characterize the mechanical properties of Collagen Gels

MATERIALS & METHODS

1. Glass activation & collagen binding

A 65x48mm No. 1 cover glass was sealed with a 80x70x10mm Poly(methyl methacrylate) (PMMA) with a hole ($D=3\text{cm}$) by applying a layer of High Vacuum Grease. Then the glass/PMMA device and a layer of PDMS with 4-6 punched wells ($D = 4\text{mm}$) were treated with oxygen plasma and the PDMS was bonded onto the cover glass. The punched wells were first treated with $5\mu\text{l}$ 1% poly-ethylene-imine (PEI) for 10min to activate the glass, then was treated with $5\mu\text{l}$ crosslinker reagent 0.1% glutaraldehyde(GA) for 30min. The wells were washed three times thoroughly and dried well.

2. Preparation of collagen gel

2.0mg/mL and 3.5 mg/mL Collagen samples were prepared. Two carboxylated fluorescent bead ($D=0.51\mu\text{m}$) concentrations were used to achieve $10\mu\text{m}$ and $40\mu\text{m}$ bead to bead spacing for z-stack tracking and defocusing ring method, respectively. Briefly, fluorescent beads were diluted with DMEM media with 10% FBS and centrifuged in sonicator for 30min. Then the diluted bead solution was mixed with M199/NaOH and collagen on ice to achieve a final PH of 7.4.

3. Flat collagen surface preparation

A No. 1 circular cover glass ($D=12\text{mm}$) was spin coated with Sigmacote, a siliconizing reagent, to be hydrophobic. The treated glass was gently placed on the surface of the collagen-filled-wells. Then the collagen sample was allowed to polymerize in the incubator at 37°C for 20min. After polymerization, 5ml media was warmed up to 37°C and filled in the PMMA well to merge the polymerized collagen. Meanwhile, the treated circular glass would gently float up and was removed.

4. Preparation of slow & fast warming gels

For slow warming collagen gel, the sample was placed on beta wipe inside a petri dish. For fast warming gel, the sample was directly placed in contact with a medal to allow faster heat transfer from the medal to the collagen sample. Both samples were first placed upside down for 6.5min and then flipped over for 13.5min.

5. Disk indentation method

A No. 1 cover glass ($D=3\text{mm}$, $\rho= 2510 \text{ kg/m}^3$, $h=0.15\text{mm}$) was used to submerge in the media and indent on collagen gel in the 24 well plate. The net force of the disk was $15.7 \mu\text{N}$.

6. Microsphere indentation (Force control)

Black paramagnetic microspheres ($D = 350\text{--}650\mu\text{m}$, $\rho= 1140 \text{ kg/m}^3$, Cospheric. Inc) were used to submerge into the media and indent on the center of the collagen gel. The resulting net force was from $0.02\text{--}0.16\mu\text{N}$. The sphere was brought to the center of image frame from low (10X) to

high magnification (40X). Then the Green Fluorescent Protein (GFP) mode was turned on to track the beads and take z-stack images.

7. *MicroIndentation(Semi-displacement control)*

A micro scale indenter was developed with a targeting spring constant to be smaller than $1\mu\text{N}/\mu\text{m}$. The indenter composed of a glass tube with a thin tip ($\sim 1.2\text{cm}$ long) forged to be $5\text{-}10\mu\text{m}$ in width and glued with a hollow glass sphere ($D=920\mu\text{m}$). The indenter was mounted on a micrometer to control the indentation depth. Similarly, the indenter was brought to the center of the image frame (IX51, Olympus America) from low (10X) to high magnification (40X, $\text{NA}=0.6$). Then the epi-fluorescent mode was turned on to track the beads.

8. *Z-stack images bead tracking*

A stack of 50 images (1344×1024) with $0.7\mu\text{m}$ spacing on z-axis was taken on the surface and bottom of the gel and on the contact point between the bottom of the sphere and the surface of the gel. The florescent beads in the image volume ($xyz: 200\mu\text{m}\times 160\mu\text{m}\times 46.0\mu\text{m}$) were tracked using Imaris, and the bead positions were converted into two-dimensional ($x\text{-}z$ & $y\text{-}z$) plots using an in-house customized MATLAB program. Finally, the 2D bead positions were used to map out the global z position, estimate the thickness of the gel before and after indentation, hence to extract the indentation depth.

9. *Defocused particle tracking method*

A defocused particle-tracking method adopted from Hall et al. was used to measure the indentation depth of collagen gel for the Microindentation method. When the point light source was positioned between the focal plane and the lens plane, a defocused circular ring due to aberration was observed. The ring diameter was measured using ImageJ. A calibration plot of the distances from the focal plane (multiply by correction factor 1.31) versus the ring diameters was generated and used to compute the bead displacement in the z direction.

RESULTS

1. Disk indentation: tilted disk

After indented the disk, the thickness of the gel under the disk was measured at four edge points and the center point of disk. The result shown that the disk was tilted, $31\pm 7.0\mu\text{m}$ in x-axis and $50\pm 46\mu\text{m}$ in y-axis for six trials.

Theoretically, disk indentation experiment can measure the poroelasticity and viscoelasticity separately, hence was proposed to characterize the complex properties of collagen gel. However, since the disk theory is assuming that the gel substrate is perfectly flat (within $2\mu\text{m}$ tolerance), the obtained results would be inaccurate.

2. Microsphere indentation: modulus

By placing the Sigmacote coated glass on the gel, the surface flatness was improved to be within $10\mu\text{m}$ across the 4mm well. This step was needed because there was no control on where to place the sphere and the gel did not return to its original shape after indentation. The thickness of the gel

before and after indentation, h_{fandh_i} , respectively, was measured to determine the indentation depth δ , which was used to calculate the modulus using Hertz Theory and the Corrected Hertz Theory 13.

For collagen gel with thickness of 350 μ m with indent strain within 20%, the moduli in the mean \pm SEM format were 34.2 \pm 2.8Pa and 20.0 \pm 2.1Pa, for 6 samples.

3. Microsphere indentation: no recovery

To evaluate whether collagen gel is truly elastic, relaxation experiment was carried out. Collagen with two concentrations (2.0 & 3.5 mg/mL), at room temperature and 37 $^{\circ}$ C, were indented by a sphere (D=350 μ m). Experimentally, no recovery activity was observed after 12 hours, indicating the indented gel was permanently deformed. This was evidenced using three techniques, z-stack images, defocused ring tracking, and confocal microscopy images (Figure 1).

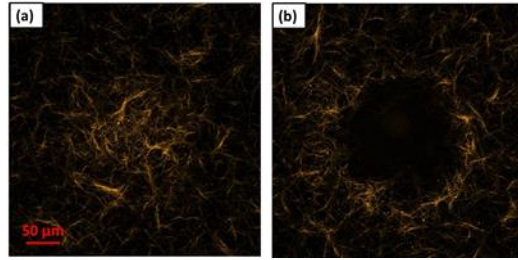


Figure 1: Confocal images of collagen after removal of microsphere. (a) dense collagen underneath sphere; (b) empty space in the center indicating no recovery of collagen.

4. Microindentation: Slow&fast warming gel modulus

Slow warming method resulted in inhomogeneous microstructure with unstructured long fibers while fast warming method resulted in homogeneous gel microstructure. Microindentation was applied to determine the modulus of these two types of collagen (2.0mg/mL) because under certain strain, collagen gel was recovered.

First, the indenter was calibrated on a balance, the obtained spring constant was $k=0.551\mu$ N/ μ m. Then the indenter was mounted on the microscopy and adjusted to be on top of the gel. When the indenter was subjected to be closed to the surface of the gel, the bead rings changed slightly. The contact point between the indenter and the gel surface was determined by slowing adjusting the micrometer until the ring size was stable. Then the micrometer was rotated to lower the indenter for $z=10, 20,$ and 30μ m to indent the gel (beyond 30μ m, the gel would not fully recover). The ring sizes for each indentation depth were measured to get the actual gel indentation depth δ , and the maximum δ corresponding to the bottom of the sphere was used.

The obtained $k, z,$ and δ , could be used to compute the force F acting on the gel using the Hook's law, $F=k(z-\delta)$. The modulus was calculated to be $E_h=530.3\pm17.5$ Pa, $E_c=358.9\pm10.4$ Pa and $E_h=779.5\pm12.7$ Pa, $E_c=538.5\pm11.7$ Pa, for slow and fast warming gel, respectively. When $z=20\mu$ m and 30μ m, the average modulus for three trials for both gels was shown in figure 2. After performing a T-test on the two samples, the result shown that there was a significant increase of

the modulus (~78% and 27%) from the slow warming gel to the fast warming gel, meaning the fast warming was stiffer.

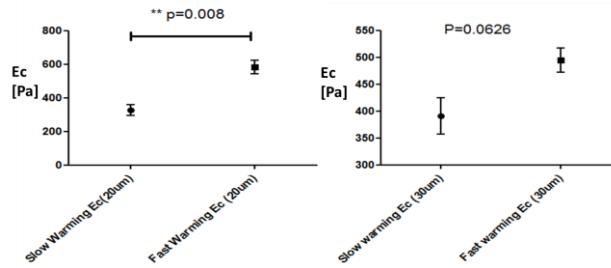


Figure 2: Comparison of the corrected modulus for slow & fast warming gels. Left plot: $z=20\mu\text{m}$; right plot: $z=30\mu\text{m}$.

5. Microsphere indentation: Poisson's ratio

Performing microsphere indentation on collagen gel, after a fixed strain is imposed, initially the media does not have sufficient time to respond, resulting an indentation δ_0 ; after a period of time, media will migrate out of the collagen network, resulting a further indentation δ_∞ ($\delta_\infty > \delta_0$). The increase of indentation depth along relaxation time can be used to compute the Poisson's ratio using derived equation from Chan et al.20

After indenting the sphere, the initial indentation δ_0 was measured at t_0 , during relaxation time, the indentation depth was measured at a 15min time interval for total 3 hours of relaxation time. A plot of the change of indentation depth verses the relaxation time was plotted. The Poisson's ratio was determined as 0.117, 0.377, 0.5, 0.336, and 0.5 for five samples.

DISCUSSION

For the slow warming collagen gel (2.0mg/mL), the corrected modulus obtained was $20.0 \pm 2.1\text{Pa}$ and $358.9 \pm 10.4\text{Pa}$ from the microsphere indentation and the microindentation, respectively, shown in figure 3. From the literature, for collagen with same concentration, the reported modulus was from 38.7Pa to 16.6kPa.

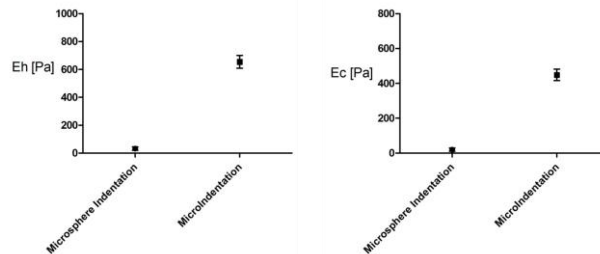


Figure 3: Comparison of the modulus using two indentation methods. Left plot: Hertz modulus; right plot: corrected modulus.

By comparing the obtained modulus using two indentation methods, the corrected modulus obtained from the microsphere indentation was 18 folds smaller compared to the microindentation.

In the microindentation, adhesion between the indenter and the gel surface was observed by examining that the ring sizes shrank compared to the original state while pulling up the indenter, indicating the gel was pulled above its original state. This adhesive force was not included in the Corrected Hertz Theory by Long et al.¹³, hence the resulted modulus may be overestimated. The resulting modulus could be corrected using the JKR model which adds adhesion into the Hertz Theory.

Lopez-Garcia et al.¹⁶ had demonstrated that the Young's modulus of collagen gel differed by varying the displacement rates (from 0.01 to 1 mm/min), indicating that the gel property is depending on the loading rate.

The gel was permanent indented using microsphere indentation method while recovered using the microindentation method with similar indented strain. This observation could be explained by two reasons: 1) The gel is depending on the loading rate, with the microsphere indentation has much faster loading rate (in milliseconds) compare to manual microindentation (in seconds). This result agrees with the result from Chandran et al.⁸, they shown that collagen deformed permanently under step compression (fast strain rate: 10% strain in 0.05s) and relaxed to its original state under ramp compression (slow strain rate: 0.1%/s strain rate for 100s). If the property of the gel was strain rate dependent, it indicated that the gel is not truly elastic. 2) Adhesion force dominates using the microindentation method that pulls back the gel while unloading.

To relate the above information to the physiological ECM experienced by migrating cells, one would think that slower strain rate can better mimic the cell motion effect (pulling & compression) on the ECM. Our lab shows that the average breast cancer cell migration speed is $\sim 0.3\mu\text{m}/\text{min}$. Also, when cells are embedded in ECM, there will be focal adhesion between the cell membrane and the ECM that cannot be neglected and even may dominate over the pulling forces, as the case for the microindentation.

The Poisson's ratio was obtained from the change of indentation depth along three hours relaxation time at 37°C . The further indentation depth of the microsphere may due to the solvent migration from underneath of the sphere, rearrangement of the fibers, and possibly the stage drift. If applied the stage drift, the resulted indentation depth would be smaller and gave larger Poisson's ratio. Another consideration is the relaxation time range. From Long's calculation, the relaxation time was in seconds while the relaxation time here was three hours long.

From literature, the Poisson's ratio was mostly assumed to be 0.2, 0.25, and 0.5^{8,9,10,11}. Roeder et al.⁹ illustrated time-lapse images of dog-bone shaped collagen (2.0mg/mL, pH=7.4) under tensile testing. Within 10% strain, the transverse and longitudinal width was measured to compute the Poisson's ratio, which was from 0.234 to 0.5. Recently, Lake et al.¹⁷ developed a model to predict the Poisson's ratio as 0.33 and validated with an experimental data of 0.35 for 1.0mg/mL collagen.

Compare the two indentation methods, microsphere indentation is simple to implement and optimal for in situ experiment in biological labs. One limitation of this method is that there is no control over the indent place on the gel. If the aim was to determine the change of indentation depth in a short time period (seconds) due to poroelasticity, the time required to adjust the

microscopic to focus on the sphere would exceed the short time period. In addition, this method induced permanent deformation of collagen gel. Microindentation, although has well control on the indent place and semi-control on the indent displacement, cannot measure the relaxation forces, limiting this method to be applied to study the poroelasticity of the gel. One solution could be using load cell indentation with displacement control and the relaxation force measurement to obtain a force relaxation curve in the time order of seconds for Poisson's ratio calculation. This method has been used by Lake et al.¹⁸ and Hu et al.¹⁹ to study the poroelasticity of collagen-agarose co-gel and pH-sensitive hydrogels, respectively.

REFERENCES

1. Chambers, A.F., A.C. Groom, and I.C. MacDonald, *Dissemination and growth of cancer cells in metastatic sites*. Nat Rev Cancer, 2002. **2**(8): p. 563-72.
2. Steeg, P.S., *Tumor metastasis: mechanistic insights and clinical challenges*. Nat Med, 2006. **12**(8): p. 895-904.
3. Wirtz, D., K. Konstantopoulos, and P.C. Searson, *The physics of cancer: the role of physical interactions and mechanical forces in metastasis*. Nat Rev Cancer, 2011. **11**(7): p. 512-522.
4. Paszek, M.J. and V.M. Weaver, *The tension mounts: mechanics meets morphogenesis and malignancy*. J Mammary Gland Biol Neoplasia, 2004. **9**(4): p. 325-42.
5. Paszek, M.J., et al., *Tensional homeostasis and the malignant phenotype*. Cancer Cell, 2005. **8**(3): p. 241-254.
6. Kumar, S. and V.M. Weaver, *Mechanics, malignancy, and metastasis: The force journey of a tumor cell*. Cancer and Metastasis Reviews, 2009. **28**(1): p. 113-127.
7. Joyce, J.A. and J.W. Pollard, *Microenvironmental regulation of metastasis*. Nat Rev Cancer, 2009. **9**(4): p. 239-52.
8. Bissell, M.J. and W.C. Hines, *Why don't we get more cancer? A proposed role of the microenvironment in restraining cancer progression*. Nat Med, 2011. **17**(3): p. 320-329.
9. Pickup, M.W., J.K. Mouw, and V.M. Weaver, *The extracellular matrix modulates the hallmarks of cancer*. EMBO reports, 2014. **15**(12): p. 1243-1253.
10. Marshall, J., *Transwell((R)) invasion assays*. Methods Mol Biol, 2011. **769**: p. 97-110.
11. Hulkower, K.I. and R.L. Herber, *Cell Migration and Invasion Assays as Tools for Drug Discovery*. Pharmaceuticals, 2011. **3**(1): p. 107-124.
12. Albini, A. and D.M. Noonan, *The 'chemoinvasion' assay, 25 years and still going strong: the use of reconstituted basement membranes to study cell invasion and angiogenesis*. Curr Opin Cell Biol, 2010. **22**(5): p. 677-89.
13. Roussos, E.T., J.S. Condeelis, and A. Patsialou, *Chemotaxis in cancer*. Nat Rev Cancer, 2011. **11**(8): p. 573-587.
14. Zhou, Z.N., P.J. Boimel, and J.E. Segall, *Tumor-stroma: In vivo assays and intravital imaging to study cell migration and metastasis*. Drug Discov Today Dis Models, 2011. **8**(2-3): p. 95-112.
15. Cekanova, M. and K. Rathore, *Animal models and therapeutic molecular targets of cancer: utility and limitations*. Drug Des Devel Ther, 2014. **8**: p. 1911-21.
16. Kim, B.J. and M. Wu, *Microfluidics for Mammalian Cell Chemotaxis*. Annals of biomedical engineering, 2012. **40**(6): p. 1316-1327.
17. Polacheck, W.J., et al., *Microfluidic platforms for mechanobiology*. Lab on a chip, 2013. **13**(12): p. 2252-2267.
18. Sung, K.E. and D.J. Beebe, *Microfluidic 3D models of cancer*. Advanced Drug Delivery Reviews, 2014. **79-80**: p. 68-78.
19. Sackmann, E.K., A.L. Fulton, and D.J. Beebe, *The present and future role of microfluidics in biomedical research*. Nature, 2014. **507**(7491): p. 181-189.
20. Tien, J., *Microfluidic approaches for engineering vasculature*. Current Opinion in Chemical Engineering, 2014. **3**: p. 36-41.
21. Boussommier-Calleja, A., et al., *Microfluidics: A new tool for modeling cancer-immune interactions*. Trends Cancer, 2016. **2**(1): p. 6-19.
22. Hanahan, D. and Robert A. Weinberg, *Hallmarks of Cancer: The Next Generation*. Cell, 2011. **144**(5): p. 646-674.
23. Friedl, P. and S. Alexander, *Cancer invasion and the microenvironment: plasticity and reciprocity*. Cell, 2011. **147**(5): p. 992-1009.

24. Meacham, C.E. and S.J. Morrison, *Tumour heterogeneity and cancer cell plasticity*. Nature, 2013. **501**(7467): p. 328-337.
25. Wu, J., X. Wu, and F. Lin, *Recent developments in microfluidics-based chemotaxis studies*. Lab on a Chip, 2013. **13**(13): p. 2484-2499.
26. Moraes, C., et al., *Organs-on-a-chip: a focus on compartmentalized microdevices*. Ann Biomed Eng, 2012. **40**(6): p. 1211-27.
27. Young, E.W., *Cells, tissues, and organs on chips: challenges and opportunities for the cancer tumor microenvironment*. Integr Biol (Camb), 2013. **5**(9): p. 1096-109.
28. GABE, I.T., et al., *Measurement of Instantaneous Blood Flow Velocity and Pressure in Conscious Man with a Catheter-Tip Velocity Probe*. Circulation, 1969. **40**(5): p. 603-614.
29. Popel, A.S. and P.C. Johnson, *Microcirculation and Hemorheology*. Annual review of fluid mechanics, 2005. **37**: p. 43-69.
30. Hahn, C. and M.A. Schwartz, *Mechanotransduction in vascular physiology and atherogenesis*. Nat Rev Mol Cell Biol, 2009. **10**(1): p. 53-62.
31. le Noble, F., et al., *Flow regulates arterial-venous differentiation in the chick embryo yolk sac*. Development, 2004. **131**(2): p. 361-75.
32. Culver, J.C. and M.E. Dickinson, *The effects of hemodynamic force on embryonic development*. Microcirculation, 2010. **17**(3): p. 164-78.
33. Lucitti, J.L., et al., *Vascular remodeling of the mouse yolk sac requires hemodynamic force*. Development, 2007. **134**(18): p. 3317-3326.
34. Davies, P.F., *Flow-mediated endothelial mechanotransduction*. Physiol Rev, 1995. **75**(3): p. 519-60.
35. Resnick, N., et al., *Fluid shear stress and the vascular endothelium: for better and for worse*. Progress in Biophysics and Molecular Biology, 2003. **81**(3): p. 177-199.
36. Li, Y.-S.J., J.H. Haga, and S. Chien, *Molecular basis of the effects of shear stress on vascular endothelial cells*. Journal of Biomechanics, 2005. **38**(10): p. 1949-1971.
37. Chien, S., *Mechanotransduction and endothelial cell homeostasis: the wisdom of the cell*. Am J Physiol Heart Circ Physiol, 2007. **292**(3): p. H1209-24.
38. Dixon, J.B., et al., *Measuring microlymphatic flow using fast video microscopy*. Journal of Biomedical Optics, 2005. **10**(6): p. 064016-064016-7.
39. Berk, D.A., et al., *Transport in lymphatic capillaries. II. Microscopic velocity measurement with fluorescence photobleaching*. Am J Physiol, 1996. **270**(1 Pt 2): p. H330-7.
40. Fischer, M., et al., *Flow velocity of single lymphatic capillaries in human skin*. American Journal of Physiology - Heart and Circulatory Physiology, 1996. **270**(1): p. H358-H363.
41. Yuan, F., et al., *Vascular permeability and microcirculation of gliomas and mammary carcinomas transplanted in rat and mouse cranial windows*. Cancer Res, 1994. **54**(17): p. 4564-8.
42. Kamoun, W.S., et al., *Simultaneous measurement of RBC velocity, flux, hematocrit and shear rate in tumor vascular networks*. Nature methods, 2010. **7**(8): p. 655-660.
43. Leunig, M., et al., *Angiogenesis, microvascular architecture, microhemodynamics, and interstitial fluid pressure during early growth of human adenocarcinoma LS174T in SCID mice*. Cancer Res, 1992. **52**(23): p. 6553-60.
44. Jain, R.K., *Determinants of tumor blood flow: a review*. Cancer Res, 1988. **48**(10): p. 2641-58.
45. Stylianopoulos, T., et al., *Coevolution of solid stress and interstitial fluid pressure in tumors during progression: implications for vascular collapse*. Cancer Res, 2013. **73**(13): p. 3833-41.
46. Jain, R.K., J.D. Martin, and T. Stylianopoulos, *The role of mechanical forces in tumor growth and therapy*. Annual review of biomedical engineering, 2014. **16**: p. 321-346.

47. Wiig, H. and M.A. Swartz, *Interstitial Fluid and Lymph Formation and Transport: Physiological Regulation and Roles in Inflammation and Cancer*. *Physiological Reviews*, 2012. **92**(3): p. 1005-1060.
48. Wong, S.Y. and R.O. Hynes, *Lymphatic or Hematogenous Dissemination: How Does a Metastatic Tumor Cell Decide?* *Cell cycle (Georgetown, Tex.)*, 2006. **5**(8): p. 812-817.
49. Paduch, R., *The role of lymphangiogenesis and angiogenesis in tumor metastasis*. *Cellular Oncology*, 2016. **39**(5): p. 397-410.
50. Chambers, A.F., et al., *Critical steps in hematogenous metastasis: an overview*. *Surg Oncol Clin N Am*, 2001. **10**(2): p. 243-55, vii.
51. Koumoutsakos, P., I. Pivkin, and F. Milde, *The Fluid Mechanics of Cancer and Its Therapy*. *Annual Review of Fluid Mechanics*, 2013. **45**(1): p. 325-355.
52. Swartz, M.A. and M. Skobe, *Lymphatic function, lymphangiogenesis, and cancer metastasis*. *Microsc Res Tech*, 2001. **55**(2): p. 92-9.
53. Jain, R.K., *Transport of molecules in the tumor interstitium: a review*. *Cancer Res*, 1987. **47**(12): p. 3039-51.
54. Chary, S.R. and R.K. Jain, *Direct measurement of interstitial convection and diffusion of albumin in normal and neoplastic tissues by fluorescence photobleaching*. *Proceedings of the National Academy of Sciences of the United States of America*, 1989. **86**(14): p. 5385-5389.
55. Ng, C.P., C.L. Helm, and M.A. Swartz, *Interstitial flow differentially stimulates blood and lymphatic endothelial cell morphogenesis in vitro*. *Microvasc Res*, 2004. **68**(3): p. 258-64.
56. Helm, C.-L.E., et al., *Synergy between interstitial flow and VEGF directs capillary morphogenesis in vitro through a gradient amplification mechanism*. *Proceedings of the National Academy of Sciences of the United States of America*, 2005. **102**(44): p. 15779-15784.
57. Helm, C.L., A. Zisch, and M.A. Swartz, *Engineered blood and lymphatic capillaries in 3-D VEGF-fibrin-collagen matrices with interstitial flow*. *Biotechnol Bioeng*, 2007. **96**(1): p. 167-76.
58. Ng, C.P., B. Hinz, and M.A. Swartz, *Interstitial fluid flow induces myofibroblast differentiation and collagen alignment in vitro*. *J Cell Sci*, 2005. **118**(Pt 20): p. 4731-9.
59. Ng, C.P. and M.A. Swartz, *Fibroblast alignment under interstitial fluid flow using a novel 3-D tissue culture model*. *Am J Physiol Heart Circ Physiol*, 2003. **284**(5): p. H1771-7.
60. Ng, C.P. and M.A. Swartz, *Mechanisms of interstitial flow-induced remodeling of fibroblast-collagen cultures*. *Ann Biomed Eng*, 2006. **34**(3): p. 446-54.
61. Dafni, H., et al., *Overexpression of vascular endothelial growth factor 165 drives peritumor interstitial convection and induces lymphatic drain: magnetic resonance imaging, confocal microscopy, and histological tracking of triple-labeled albumin*. *Cancer Res*, 2002. **62**(22): p. 6731-9.
62. Kingsmore, K.M., et al., *MRI analysis to map interstitial flow in the brain tumor microenvironment*. *APL Bioeng*, 2018. **2**(3).
63. Hompland, T., et al., *Interstitial Fluid Pressure and Associated Lymph Node Metastasis Revealed in Tumors by Dynamic Contrast-Enhanced MRI*. *Cancer Research*, 2012. **72**(19): p. 4899-4908.
64. Butler, T.P., F.H. Grantham, and P.M. Gullino, *Bulk transfer of fluid in the interstitial compartment of mammary tumors*. *Cancer Res*, 1975. **35**(11 Pt 1): p. 3084-8.
65. Jain, R.K. and L.T. Baxter, *Mechanisms of heterogeneous distribution of monoclonal antibodies and other macromolecules in tumors: significance of elevated interstitial pressure*. *Cancer Res*, 1988. **48**(24 Pt 1): p. 7022-32.
66. Boucher, Y., L.T. Baxter, and R.K. Jain, *Interstitial pressure gradients in tissue-isolated and subcutaneous tumors: implications for therapy*. *Cancer Res*, 1990. **50**(15): p. 4478-84.
67. Jain, R.K., *Delivery of Molecular Medicine to Solid Tumors*. *Science*, 1996. **271**(5252): p. 1079-1080.

68. Heldin, C.-H., et al., *High interstitial fluid pressure [mdash] an obstacle in cancer therapy*. Nat Rev Cancer, 2004. **4**(10): p. 806-813.
69. Lunt, S.J., et al., *Interstitial fluid pressure in tumors: therapeutic barrier and biomarker of angiogenesis*. Future Oncology, 2008. **4**(6): p. 793-802.
70. Shields, J.D., et al., *Autologous chemotaxis as a mechanism of tumor cell homing to lymphatics via interstitial flow and autocrine CCR7 signaling*. Cancer Cell, 2007. **11**(6): p. 526-38.
71. Adrian, C.S. and A.S. Melody, *Regulation of tumor invasion by interstitial fluid flow*. Physical Biology, 2011. **8**(1): p. 015012.
72. Munson, J.M., R.V. Bellamkonda, and M.A. Swartz, *Interstitial flow in a 3D microenvironment increases glioma invasion by a CXCR4-dependent mechanism*. Cancer Res, 2013. **73**(5): p. 1536-46.
73. Kingsmore, K.M., et al., *Interstitial flow differentially increases patient-derived glioblastoma stem cell invasion via CXCR4, CXCL12, and CD44-mediated mechanisms*. Integrative Biology, 2016. **8**(12): p. 1246-1260.
74. Qazi, H., et al., *Cancer cell glycocalyx mediates mechanotransduction and flow-regulated invasion*. Integr Biol (Camb), 2013. **5**(11): p. 1334-43.
75. Shieh, A.C., et al., *Tumor cell invasion is promoted by interstitial flow-induced matrix priming by stromal fibroblasts*. Cancer Res, 2011. **71**(3): p. 790-800.
76. Tchafa, A.M., et al., *EMT Transition Alters Interstitial Fluid Flow–Induced Signaling in ERBB2-Positive Breast Cancer Cells*. Molecular Cancer Research, 2015. **13**(4): p. 755-764.
77. Shah, A.D., M.J. Bouchard, and A.C. Shieh, *Interstitial Fluid Flow Increases Hepatocellular Carcinoma Cell Invasion through CXCR4/CXCL12 and MEK/ERK Signaling*. PLoS One, 2015. **10**(11): p. e0142337.
78. Lu, P., V.M. Weaver, and Z. Werb, *The extracellular matrix: A dynamic niche in cancer progression*. The Journal of Cell Biology, 2012. **196**(4): p. 395-406.
79. Pathak, A. and S. Kumar, *Biophysical regulation of tumor cell invasion: moving beyond matrix stiffness*. Integr Biol (Camb), 2011. **3**(4): p. 267-78.
80. Chang, J.M., et al., *Clinical application of shear wave elastography (SWE) in the diagnosis of benign and malignant breast diseases*. Breast Cancer Research and Treatment, 2011. **129**(1): p. 89-97.
81. Boyd, N.F., et al., *Mammographic densities and breast cancer risk*. Cancer Epidemiol Biomarkers Prev, 1998. **7**(12): p. 1133-44.
82. Acerbi, I., et al., *Human breast cancer invasion and aggression correlates with ECM stiffening and immune cell infiltration*. Integr Biol (Camb), 2015. **7**(10): p. 1120-34.
83. Kirschmann, D.A., et al., *A molecular role for lysyl oxidase in breast cancer invasion*. Cancer Res, 2002. **62**(15): p. 4478-83.
84. Levental, K.R., et al., *Matrix Crosslinking Forces Tumor Progression by Enhancing Integrin Signaling*. Cell, 2009. **139**(5): p. 891-906.
85. Condeelis, J. and J.E. Segall, *Intravital imaging of cell movement in tumours*. Nat Rev Cancer, 2003. **3**(12): p. 921-30.
86. Weigel, B., G.-J. Bakker, and P. Friedl, *Intravital third harmonic generation microscopy of collective melanoma cell invasion*. IntraVital, 2012. **1**(1): p. 32-43.
87. Alexander, S., et al., *Preclinical intravital microscopy of the tumour-stroma interface: invasion, metastasis, and therapy response*. Current Opinion in Cell Biology, 2013. **25**(5): p. 659-671.
88. Gehler, S., et al., *Filamin A– β 1 Integrin Complex Tunes Epithelial Cell Response to Matrix Tension*. Molecular Biology of the Cell, 2009. **20**(14): p. 3224-3238.

89. Hall, M.S., et al., *Fibrous nonlinear elasticity enables positive mechanical feedback between cells and ECMs*. Proceedings of the National Academy of Sciences, 2016. **113**(49): p. 14043-14048.
90. Provenzano, P.P., et al., *Collagen reorganization at the tumor-stromal interface facilitates local invasion*. BMC Medicine, 2006. **4**(1): p. 38.
91. Conklin, M.W., et al., *Aligned collagen is a prognostic signature for survival in human breast carcinoma*. Am J Pathol, 2011. **178**(3): p. 1221-32.
92. Gaggioli, C., et al., *Fibroblast-led collective invasion of carcinoma cells with differing roles for RhoGTPases in leading and following cells*. Nat Cell Biol, 2007. **9**(12): p. 1392-1400.
93. Gritsenko, P.G., O. Ilina, and P. Friedl, *Interstitial guidance of cancer invasion*. J Pathol, 2012. **226**(2): p. 185-99.
94. Wolf, K., et al., *Collagen-based cell migration models in vitro and in vivo*. Seminars in Cell & Developmental Biology, 2009. **20**(8): p. 931-941.
95. Doyle, A.D., et al., *One-dimensional topography underlies three-dimensional fibrillar cell migration*. J Cell Biol, 2009. **184**(4): p. 481-90.
96. Friedl, P., et al., *New dimensions in cell migration*. Nat Rev Mol Cell Biol, 2012. **13**(11): p. 743-747.
97. Chang, Stephanie S., et al., *Guidance of Cell Migration by Substrate Dimension*. Biophysical Journal, 2013. **104**(2): p. 313-321.
98. Chrobak, K.M., D.R. Potter, and J. Tien, *Formation of perfused, functional microvascular tubes in vitro*. Microvascular Research, 2006. **71**(3): p. 185-196.
99. Nguyen, D.-H.T., et al., *Biomimetic model to reconstitute angiogenic sprouting morphogenesis in vitro*. Proceedings of the National Academy of Sciences, 2013. **110**(17): p. 6712-6717.
100. Wong, A.D. and P.C. Searson, *Live-Cell Imaging of Invasion and Intravasation in an Artificial Microvessel Platform*. Cancer Research, 2014. **74**(17): p. 4937-4945.
101. Jimenez-Torres, J.A., D.J. Beebe, and K.E. Sung, *A Microfluidic Method to Mimic Luminal Structures in the Tumor Microenvironment*. Methods Mol Biol, 2016. **1458**: p. 59-69.
102. Zheng, Y., et al., *In vitro microvessels for the study of angiogenesis and thrombosis*. Proceedings of the National Academy of Sciences, 2012. **109**(24): p. 9342-9347.
103. Buchanan, C.F., et al., *Flow shear stress regulates endothelial barrier function and expression of angiogenic factors in a 3D microfluidic tumor vascular model*. Cell Adhesion & Migration, 2014. **8**(5): p. 517-524.
104. Bischel, L.L., S.H. Lee, and D.J. Beebe, *A practical method for patterning lumens through ECM hydrogels via viscous finger patterning*. J Lab Autom, 2012. **17**(2): p. 96-103.
105. Bischel, L.L., et al., *Tubeless microfluidic angiogenesis assay with three-dimensional endothelial-lined microvessels*. Biomaterials, 2013. **34**(5): p. 1471-1477.
106. Bischel, L.L., et al., *The importance of being a lumen*. The FASEB Journal, 2014. **28**(11): p. 4583-4590.
107. Golden, A.P. and J. Tien, *Fabrication of microfluidic hydrogels using molded gelatin as a sacrificial element*. Lab Chip, 2007. **7**(6): p. 720-5.
108. Bellan, L.M., et al., *Fabrication of an artificial 3-dimensional vascular network using sacrificial sugar structures*. Soft Matter, 2009. **5**(7): p. 1354-1357.
109. Miller, J.S., et al., *Rapid casting of patterned vascular networks for perfusable engineered three-dimensional tissues*. Nat Mater, 2012. **11**(9): p. 768-774.
110. Kolesky, D.B., et al., *3D Bioprinting of Vascularized, Heterogeneous Cell-Laden Tissue Constructs*. Advanced Materials, 2014. **26**(19): p. 3124-3130.
111. Bertassoni, L.E., et al., *Hydrogel bioprinted microchannel networks for vascularization of tissue engineering constructs*. Lab on a Chip, 2014. **14**(13): p. 2202-2211.

112. Sobrino, A., et al., *3D microtumors in vitro supported by perfused vascular networks*. Scientific Reports, 2016. **6**: p. 31589.
113. Moya, M.L., et al., *In Vitro Perfused Human Capillary Networks*. Tissue Engineering Part C: Methods, 2013. **19**(9): p. 730-737.
114. Phan, D.T.T., et al., *A vascularized and perfused organ-on-a-chip platform for large-scale drug screening applications*. Lab on a Chip, 2017. **17**(3): p. 511-520.
115. Kim, S., M. Chung, and N.L. Jeon, *Three-dimensional biomimetic model to reconstitute sprouting lymphangiogenesis in vitro*. Biomaterials, 2016. **78**: p. 115-28.
116. Gerlowski, L.E. and R.K. Jain, *Microvascular permeability of normal and neoplastic tissues*. Microvascular Research, 1986. **31**(3): p. 288-305.
117. Price, G.M., et al., *Effect of Mechanical Factors on the Function of Engineered Human Blood Microvessels in Microfluidic Collagen Gels*. Biomaterials, 2010. **31**(24): p. 6182-6189.
118. Jeon, J.S., et al., *Human 3D vascularized organotypic microfluidic assays to study breast cancer cell extravasation*. Proceedings of the National Academy of Sciences, 2015. **112**(1): p. 214-219.
119. Song, J.W. and L.L. Munn, *Fluid forces control endothelial sprouting*. Proceedings of the National Academy of Sciences, 2011. **108**(37): p. 15342-15347.
120. Zhang, Q., T. Liu, and J. Qin, *A microfluidic-based device for study of transendothelial invasion of tumor aggregates in realtime*. Lab on a Chip, 2012. **12**(16): p. 2837-2842.
121. Zervantonakis, I.K., et al., *Three-dimensional microfluidic model for tumor cell intravasation and endothelial barrier function*. Proceedings of the National Academy of Sciences, 2012. **109**(34): p. 13515-13520.
122. Ehsan, S.M., et al., *A three-dimensional in vitro model of tumor cell intravasation*. Integr Biol (Camb), 2014. **6**(6): p. 603-10.
123. Wong, A.D. and P.C. Searson, *Mitosis-Mediated Intravasation in a Tissue-Engineered Tumor-Microvessel Platform*. Cancer Res, 2017. **77**(22): p. 6453-6461.
124. Pisano, M., et al., *An in vitro model of the tumor-lymphatic microenvironment with simultaneous transendothelial and luminal flows reveals mechanisms of flow enhanced invasion*. Integrative Biology, 2015. **7**(5): p. 525-533.
125. Michel, C.C. and F.E. Curry, *Microvascular permeability*. Physiol Rev, 1999. **79**(3): p. 703-61.
126. Fu, B.M. and S. Shen, *Acute VEGF effect on solute permeability of mammalian microvessels in vivo*. Microvascular Research, 2004. **68**(1): p. 51-62.
127. Yuan, W., et al., *Non-invasive measurement of solute permeability in cerebral microvessels of the rat*. Microvascular Research, 2009. **77**(2): p. 166-173.
128. Scallan, J.P. and V.H. Huxley, *In vivo determination of collecting lymphatic vessel permeability to albumin: a role for lymphatics in exchange*. J Physiol, 2010. **588**(Pt 1): p. 243-54.
129. Yuan, F., et al., *Microvascular permeability of albumin, vascular surface area, and vascular volume measured in human adenocarcinoma LS174T using dorsal chamber in SCID mice*. Microvasc Res, 1993. **45**(3): p. 269-89.
130. Dreher, M.R., et al., *Tumor vascular permeability, accumulation, and penetration of macromolecular drug carriers*. J Natl Cancer Inst, 2006. **98**(5): p. 335-44.
131. Albelda, S.M., et al., *Permeability characteristics of cultured endothelial cell monolayers*. Journal of Applied Physiology, 1988. **64**(1): p. 308-322.
132. Roeder, B.A., et al., *Tensile mechanical properties of three-dimensional type I collagen extracellular matrices with varied microstructure*. J Biomech Eng, 2002. **124**(2): p. 214-22.
133. Storm, C., et al., *Nonlinear elasticity in biological gels*. Nature, 2005. **435**(7039): p. 191-194.
134. Polacheck, W.J., J.L. Charest, and R.D. Kamm, *Interstitial flow influences direction of tumor cell migration through competing mechanisms*. Proceedings of the National Academy of Sciences, 2011. **108**(27): p. 11115-11120.

135. Haessler, U., et al., *Migration dynamics of breast cancer cells in a tunable 3D interstitial flow chamber*. Integr Biol (Camb), 2012. **4**(4): p. 401-9.
136. Tung, C.K., et al., *A contact line pinning based microfluidic platform for modelling physiological flows*. Lab Chip, 2013. **13**(19): p. 3876-85.
137. Huang, Y.L., et al., *Interstitial flows promote amoeboid over mesenchymal motility of breast cancer cells revealed by a three dimensional microfluidic model*. Integrative Biology, 2015. **7**(11): p. 1402-1411.
138. Polacheck, W.J., et al., *Mechanotransduction of fluid stresses governs 3D cell migration*. Proceedings of the National Academy of Sciences, 2014. **111**(7): p. 2447-2452.
139. Swartz, M.A. and M.E. Fleury, *Interstitial flow and its effects in soft tissues*. Annu Rev Biomed Eng, 2007. **9**: p. 229-56.
140. Levick, J.R., *Flow through interstitium and other fibrous matrices*. Q J Exp Physiol, 1987. **72**(4): p. 409-37.
141. Cross, V.L., et al., *Dense type I collagen matrices that support cellular remodeling and microfabrication for studies of tumor angiogenesis and vasculogenesis in vitro*. Biomaterials, 2010. **31**(33): p. 8596-607.
142. Ramanujan, S., et al., *Diffusion and convection in collagen gels: implications for transport in the tumor interstitium*. Biophysical Journal, 2002. **83**(3): p. 1650-1660.
143. Raub, C.B., et al., *Image Correlation Spectroscopy of Multiphoton Images Correlates with Collagen Mechanical Properties*. Biophysical Journal, 2008. **94**(6): p. 2361-2373.
144. Yang, Y.L., S. Motte, and L.J. Kaufman, *Pore size variable type I collagen gels and their interaction with glioma cells*. Biomaterials, 2010. **31**(21): p. 5678-88.
145. Piotrowski-Daspit, A.S., J. Tien, and C.M. Nelson, *Interstitial fluid pressure regulates collective invasion in engineered human breast tumors via Snail, vimentin, and E-cadherin*. Integrative Biology, 2016. **8**(3): p. 319-331.
146. Friedl, P. and K. Wolf, *Tumour-cell invasion and migration: diversity and escape mechanisms*. Nat Rev Cancer, 2003. **3**(5): p. 362-74.
147. Friedl, P., et al., *Classifying collective cancer cell invasion*. Nat Cell Biol, 2012. **14**(8): p. 777-783.
148. Patsialou, A., et al., *Intravital multiphoton imaging reveals multicellular streaming as a crucial component of in vivo cell migration in human breast tumors*. Intravital, 2013. **2**(2): p. e25294.
149. Rizvi, I., et al., *Flow induces epithelial-mesenchymal transition, cellular heterogeneity and biomarker modulation in 3D ovarian cancer nodules*. Proceedings of the National Academy of Sciences of the United States of America, 2013. **110**(22): p. E1974-E1983.
150. Nelson, M.T., et al., *Preferential, enhanced breast cancer cell migration on biomimetic electrospun nanofiber 'cell highways'*. BMC Cancer, 2014. **14**: p. 825.
151. Milano, Daniel F., et al., *Regulators of Metastasis Modulate the Migratory Response to Cell Contact under Spatial Confinement*. Biophysical Journal, 2016. **110**(8): p. 1886-1895.
152. Lee, P., et al., *Microfluidic alignment of collagen fibers for in vitro cell culture*. Biomed Microdevices, 2006. **8**(1): p. 35-41.
153. Riching, K.M., et al., *3D collagen alignment limits protrusions to enhance breast cancer cell persistence*. Biophys J, 2014. **107**(11): p. 2546-58.
154. Sung, K.E., et al., *Control of 3-dimensional collagen matrix polymerization for reproducible human mammary fibroblast cell culture in microfluidic devices*. Biomaterials, 2009. **30**(27): p. 4833-4841.
155. Lanfer, B., et al., *Aligned fibrillar collagen matrices obtained by shear flow deposition*. Biomaterials, 2008. **29**(28): p. 3888-95.
156. Han, W., et al., *Oriented collagen fibers direct tumor cell intravasation*. Proceedings of the National Academy of Sciences, 2016. **113**(40): p. 11208-11213.

157. Vader, D., et al., *Strain-Induced Alignment in Collagen Gels*. PLoS ONE, 2009. **4**(6): p. e5902.
158. Kim, J., J.R. Staunton, and K. Tanner, *Independent Control of Topography for 3D Patterning of the ECM Microenvironment*. Adv Mater, 2016. **28**(1): p. 132-7.
159. Iliina, O., et al., *Two-photon laser-generated microtracks in 3D collagen lattices: principles of MMP-dependent and -independent collective cancer cell invasion*. Phys Biol, 2011. **8**(1): p. 015010.
160. Kraning-Rush, C.M., et al., *Microfabricated collagen tracks facilitate single cell metastatic invasion in 3D*. Integr Biol (Camb), 2013. **5**(3): p. 606-16.
161. Wolf, K., et al., *Physical limits of cell migration: Control by ECM space and nuclear deformation and tuning by proteolysis and traction force*. The Journal of Cell Biology, 2013. **201**(7): p. 1069-1084.
162. Isermann, P., et al., *Assays to measure nuclear mechanics in interphase cells*. Curr Protoc Cell Biol, 2012. **Chapter 22**: p. Unit22.16.
163. Davidson, P.M., et al., *Design of a microfluidic device to quantify dynamic intra-nuclear deformation during cell migration through confining environments*. Integrative Biology, 2015. **7**(12): p. 1534-1546.
164. Denais, C.M., et al., *Nuclear envelope rupture and repair during cancer cell migration*. Science, 2016. **352**(6283): p. 353-8.
165. Skau, C.T., et al., *FMN2 Makes Perinuclear Actin to Protect Nuclei during Confined Migration and Promote Metastasis*. Cell, 2016. **167**(6): p. 1571-1585.e18.
166. Miron-Mendoza, M., J. Seemann, and F. Grinnell, *The differential regulation of cell motile activity through matrix stiffness and porosity in three dimensional collagen matrices*. Biomaterials, 2010. **31**(25): p. 6425-35.
167. Raub, C.B., et al., *Noninvasive assessment of collagen gel microstructure and mechanics using multiphoton microscopy*. Biophys J, 2007. **92**(6): p. 2212-22.
168. Roy, R., A. Boskey, and L.J. Bonassar, *Processing of type I collagen gels using nonenzymatic glycation*. J Biomed Mater Res A, 2010. **93**(3): p. 843-51.
169. Mason, B.N., et al., *Tuning three-dimensional collagen matrix stiffness independently of collagen concentration modulates endothelial cell behavior*. Acta Biomater, 2013. **9**(1): p. 4635-44.
170. Cassereau, L., et al., *A 3D tension bioreactor platform to study the interplay between ECM stiffness and tumor phenotype*. Journal of Biotechnology, 2015. **193**: p. 66-69.
171. Hanahan, D. and Robert A. Weinberg, *Hallmarks of Cancer: The Next Generation*. Cell. **144**(5): p. 646-674.
172. Tung, C.-k., et al., *A contact line pinning based microfluidic platform for modelling physiological flows*. Lab on a chip, 2013. **13**(19): p. 3876-3885.
173. Wu, M. and M.A. Swartz, *Modeling Tumor Microenvironments In Vitro*. Journal of Biomechanical Engineering, 2014. **136**(2): p. 021011-021011.
174. Deegan, R.D., et al., *Capillary flow as the cause of ring stains from dried liquid drops*. Nature, 1997. **389**: p. 827.
175. Vulto, P., et al., *Phaseguides: a paradigm shift in microfluidic priming and emptying*. Lab Chip, 2011. **11**(9): p. 1596-602.
176. Chauhan, V.P., et al., *Multiscale measurements distinguish cellular and interstitial hindrances to diffusion in vivo*. Biophys J, 2009. **97**(1): p. 330-6.
177. Jain, R.K., *Transport of Molecules in the Tumor Interstitium: A Review*. Cancer Research, 1987. **47**(12): p. 3039-3051.
178. Chary, S.R. and R.K. Jain, *Direct measurement of interstitial convection and diffusion of albumin in normal and neoplastic tissues by fluorescence photobleaching*. Proc Natl Acad Sci U S A, 1989. **86**(14): p. 5385-9.

179. Hompland, T., et al., *Interstitial fluid pressure and associated lymph node metastasis revealed in tumors by dynamic contrast-enhanced MRI*. *Cancer Res*, 2012. **72**(19): p. 4899-908.
180. Munson, J.M. and A.C. Shieh, *Interstitial fluid flow in cancer: implications for disease progression and treatment*. *Cancer Manag Res*, 2014. **6**: p. 317-28.
181. Heldin, C.H., et al., *High interstitial fluid pressure - an obstacle in cancer therapy*. *Nat Rev Cancer*, 2004. **4**(10): p. 806-13.
182. Less, J.R., et al., *Interstitial hypertension in human breast and colorectal tumors*. *Cancer Res*, 1992. **52**(22): p. 6371-4.
183. Boucher, Y., M. Leunig, and R.K. Jain, *Tumor angiogenesis and interstitial hypertension*. *Cancer Res*, 1996. **56**(18): p. 4264-6.
184. Weidner, N., et al., *Tumor angiogenesis and metastasis--correlation in invasive breast carcinoma*. *N Engl J Med*, 1991. **324**(1): p. 1-8.
185. Skobe, M., et al., *Induction of tumor lymphangiogenesis by VEGF-C promotes breast cancer metastasis*. *Nat Med*, 2001. **7**(2): p. 192-8.
186. Harrell, M.I., B.M. Iritani, and A. Ruddell, *Tumor-Induced Sentinel Lymph Node Lymphangiogenesis and Increased Lymph Flow Precede Melanoma Metastasis*. *The American Journal of Pathology*, 2007. **170**(2): p. 774-786.
187. Butcher, D.T., T. Alliston, and V.M. Weaver, *A tense situation: forcing tumour progression*. *Nat Rev Cancer*, 2009. **9**(2): p. 108-22.
188. Reed, R.K. and K. Rubin, *Transcapillary exchange: role and importance of the interstitial fluid pressure and the extracellular matrix*. *Cardiovasc Res*, 2010. **87**(2): p. 211-7.
189. Carter, C.L., C. Allen, and D.E. Henson, *Relation of tumor size, lymph node status, and survival in 24,740 breast cancer cases*. *Cancer*, 1989. **63**(1): p. 181-187.
190. Cai, T., et al., *Clinical importance of lymph node density in predicting outcome of prostate cancer patients*. *J Surg Res*, 2011. **167**(2): p. 267-72.
191. Friedl, P. and K. Wolf, *Plasticity of cell migration: a multiscale tuning model*. *The Journal of Cell Biology*, 2010. **188**(1): p. 11-19.
192. Pinner, S. and E. Sahai, *Imaging amoeboid cancer cell motility in vivo*. *J Microsc*, 2008. **231**(3): p. 441-5.
193. Lammermann, T., et al., *Rapid leukocyte migration by integrin-independent flowing and squeezing*. *Nature*, 2008. **453**(7191): p. 51-5.
194. Guck, J., et al., *Critical review: cellular mechanobiology and amoeboid migration*. *Integrative Biology*, 2010. **2**(11-12): p. 575-583.
195. Ricart, B.G., et al., *Measuring traction forces of motile dendritic cells on micropost arrays*. *Biophys J*, 2011. **101**(11): p. 2620-8.
196. Renkawitz, J. and M. Sixt, *Mechanisms of force generation and force transmission during interstitial leukocyte migration*. *EMBO Rep*, 2010. **11**(10): p. 744-50.
197. Nabeshima, K., et al., *Matrix metalloproteinases in tumor invasion: role for cell migration*. *Pathol Int*, 2002. **52**(4): p. 255-64.
198. Zaman, M.H., et al., *Migration of tumor cells in 3D matrices is governed by matrix stiffness along with cell-matrix adhesion and proteolysis*. *Proceedings of the National Academy of Sciences*, 2006. **103**(29): p. 10889-10894.
199. Friedl, P., K.S. Zanker, and E.B. Brocker, *Cell migration strategies in 3-D extracellular matrix: differences in morphology, cell matrix interactions, and integrin function*. *Microsc Res Tech*, 1998. **43**(5): p. 369-78.
200. Cukierman, E., et al., *Taking Cell-Matrix Adhesions to the Third Dimension*. *Science*, 2001. **294**(5547): p. 1708-1712.

201. Wolf, K., et al., *Compensation mechanism in tumor cell migration: mesenchymal-amoeboid transition after blocking of pericellular proteolysis*. J Cell Biol, 2003. **160**(2): p. 267-77.
202. Wells, A., et al., *Targeting tumor cell motility as a strategy against invasion and metastasis*. Trends Pharmacol Sci, 2013. **34**(5): p. 283-9.
203. Polacheck, W.J., et al., *Mechanotransduction of fluid stresses governs 3D cell migration*. Proceedings of the National Academy of Sciences of the United States of America, 2014. **111**(7): p. 2447-2452.
204. Petrie, R.J., et al., *Nonpolarized signaling reveals two distinct modes of 3D cell migration*. J Cell Biol, 2012. **197**(3): p. 439-55.
205. Sanz-Moreno, V., et al., *Rac activation and inactivation control plasticity of tumor cell movement*. Cell, 2008. **135**(3): p. 510-23.
206. Ulrich, T.A., et al., *Probing cellular mechanobiology in three-dimensional culture with collagen-agarose matrices*. Biomaterials, 2010. **31**(7): p. 1875-84.
207. Yamazaki, D., S. Kurisu, and T. Takenawa, *Involvement of Rac and Rho signaling in cancer cell motility in 3D substrates*. Oncogene, 2009. **28**(13): p. 1570-83.
208. Sahai, E. and C.J. Marshall, *Differing modes of tumour cell invasion have distinct requirements for Rho/ROCK signalling and extracellular proteolysis*. Nat Cell Biol, 2003. **5**(8): p. 711-9.
209. Parsons, J.T., A.R. Horwitz, and M.A. Schwartz, *Cell adhesion: integrating cytoskeletal dynamics and cellular tension*. Nature reviews Molecular cell biology, 2010. **11**(9): p. 633-643.
210. Pankov, R. and K.M. Yamada, *Fibronectin at a glance*. Journal of Cell Science, 2002. **115**(20): p. 3861-3863.
211. Orr, A.W., et al., *Matrix-specific Suppression of Integrin Activation in Shear Stress Signaling*. Molecular Biology of the Cell, 2006. **17**(11): p. 4686-4697.
212. Engler, A.J., et al., *A novel mode of cell detachment from fibrillar fibronectin matrix under shear*. J Cell Sci, 2009. **122**(Pt 10): p. 1647-53.
213. Wu, P.-H., et al., *Three-dimensional cell migration does not follow a random walk*. Proceedings of the National Academy of Sciences, 2014. **111**(11): p. 3949-3954.
214. Berg, H.C., *Random walks in biology*. 1983, Princeton, N.J.: Princeton University Press.
215. Roeder, B.A., et al., *Tensile Mechanical Properties of Three-Dimensional Type I Collagen Extracellular Matrices With Varied Microstructure*. Journal of Biomechanical Engineering, 2002. **124**(2): p. 214-222.
216. Hall, M.S., et al., *Toward single cell traction microscopy within 3D collagen matrices*. Experimental cell research, 2013. **319**(16): p. 2396-2408.
217. Provenzano, P.P., et al., *Collagen reorganization at the tumor-stromal interface facilitates local invasion*. BMC Med, 2006. **4**(1): p. 38.
218. Li, T., et al., *The association of measured breast tissue characteristics with mammographic density and other risk factors for breast cancer*. Cancer Epidemiol Biomarkers Prev, 2005. **14**(2): p. 343-9.
219. Ulrich, T.A., E.M. de Juan Pardo, and S. Kumar, *The mechanical rigidity of the extracellular matrix regulates the structure, motility, and proliferation of glioma cells*. Cancer Res, 2009. **69**(10): p. 4167-74.
220. Spiering, D. and L. Hodgson, *Multiplex imaging of Rho family GTPase activities in living cells*. Methods Mol Biol, 2012. **827**: p. 215-34.
221. Machacek, M., et al., *Coordination of Rho GTPase activities during cell protrusion*. Nature, 2009. **461**: p. 99.
222. Hall, J.E., *Guyton and Hall textbook of medical physiology*. 2016.
223. Shieh, A.C. and M.A. Swartz, *Regulation of tumor invasion by interstitial fluid flow*. Phys Biol, 2011. **8**(1): p. 015012.

224. Kim, B.J. and M. Wu, *Microfluidics for mammalian cell chemotaxis*. Ann Biomed Eng, 2012. **40**(6): p. 1316-27.
225. Wu, M. and M.A. Swartz, *Modeling tumor microenvironments in vitro*. J Biomech Eng, 2014. **136**(2): p. 021011.
226. Huang, Y.L., J.E. Segall, and M. Wu, *Microfluidic modeling of the biophysical microenvironment in tumor cell invasion*. Lab Chip, 2017. **17**(19): p. 3221-3233.
227. Polacheck, W.J., J.L. Charest, and R.D. Kamm, *Interstitial flow influences direction of tumor cell migration through competing mechanisms*. Proc Natl Acad Sci U S A, 2011. **108**(27): p. 11115-20.
228. Bissell, M.J. and D. Radisky, *Putting tumours in context*. Nature Reviews Cancer, 2001. **1**: p. 46.
229. Egeblad, M., E.S. Nakasone, and Z. Werb, *Tumors as Organs: Complex Tissues that Interface with the Entire Organism*. Developmental Cell, 2010. **18**(6): p. 884-901.
230. Liotta, L.A. and E.C. Kohn, *The microenvironment of the tumour-host interface*. Nature, 2001. **411**(6835): p. 375-9.
231. Li, R., et al., *Interstitial flow promotes macrophage polarization toward an M2 phenotype*. Mol Biol Cell, 2018. **29**(16): p. 1927-1940.
232. Marturano-Kruik, A., et al., *Human bone perivascular niche-on-a-chip for studying metastatic colonization*. Proceedings of the National Academy of Sciences, 2018. **115**(6): p. 1256-1261.
233. Bissell, M.J., A. Rizki, and I.S. Mian, *Tissue architecture: the ultimate regulator of breast epithelial function*. Current opinion in cell biology, 2003. **15**(6): p. 753-762.
234. Tlsty, T.D. and L.M. Coussens, *Tumor stroma and regulation of cancer development*. Annu Rev Pathol, 2006. **1**: p. 119-50.
235. Carey, S.P., et al., *Leading malignant cells initiate collective epithelial cell invasion in a three-dimensional heterotypic tumor spheroid model*. Clin Exp Metastasis, 2013. **30**(5): p. 615-30.
236. Allinen, M., et al., *Molecular characterization of the tumor microenvironment in breast cancer*. Cancer Cell, 2004. **6**(1): p. 17-32.
237. Muschler, J. and M.J. Bissell, *Order and Disorder: The Role of Extracellular Matrix in Epithelial Cancer* AU - Radisky, Derek. Cancer Investigation, 2002. **20**(1): p. 139-153.
238. Huang, Y.L., et al., *Interstitial flows promote amoeboid over mesenchymal motility of breast cancer cells revealed by a three dimensional microfluidic model*. Integr Biol (Camb), 2015. **7**(11): p. 1402-11.
239. Weiswald, L.-B., D. Bellet, and V. Dangles-Marie, *Spherical Cancer Models in Tumor Biology*. Neoplasia, 2015. **17**(1): p. 1-15.
240. Song, W., et al., *Dynamic self-organization of microwell-aggregated cellular mixtures*. Soft Matter, 2016. **12**(26): p. 5739-46.
241. Hall, M.S., et al., *Toward single cell traction microscopy within 3D collagen matrices*. Exp Cell Res, 2013. **319**(16): p. 2396-408.
242. Petrie, R.J., et al., *Nonpolarized signaling reveals two distinct modes of 3D cell migration*. The Journal of Cell Biology, 2012. **197**(3): p. 439-455.
243. Ivascu, A. and M. Kubbies, *Diversity of cell-mediated adhesions in breast cancer spheroids*. Int J Oncol, 2007. **31**(6): p. 1403-13.
244. Kim, B.J., et al., *Cooperative roles of SDF-1alpha and EGF gradients on tumor cell migration revealed by a robust 3D microfluidic model*. PLoS One, 2013. **8**(7): p. e68422.
245. Bhattacharjee, N., et al., *The upcoming 3D-printing revolution in microfluidics*. Lab on a Chip, 2016. **16**(10): p. 1720-1742.
246. Gjorevski, N. and C.M. Nelson, *Mapping of mechanical strains and stresses around quiescent engineered three-dimensional epithelial tissues*. Biophys J, 2012. **103**(1): p. 152-62.
247. Legant, W.R., et al., *Measurement of mechanical tractions exerted by cells within three-dimensional matrices*. Nature methods, 2010. **7**(12): p. 969-971.

248. Irianto, J., et al., *DNA Damage Follows Repair Factor Depletion and Portends Genome Variation in Cancer Cells after Pore Migration*. *Current Biology*, 2017. **27**(2): p. 210-223.
249. Shembekar, N., et al., *Droplet-based microfluidics in drug discovery, transcriptomics and high-throughput molecular genetics*. *Lab on a Chip*, 2016. **16**(8): p. 1314-1331.
250. Ahrberg, C.D., A. Manz, and B.G. Chung, *Polymerase chain reaction in microfluidic devices*. *Lab on a Chip*, 2016. **16**(20): p. 3866-3884.